High-Fidelity Structural Sizing Method for Weight Estimation of a Flying-V

Marloes Nanninga

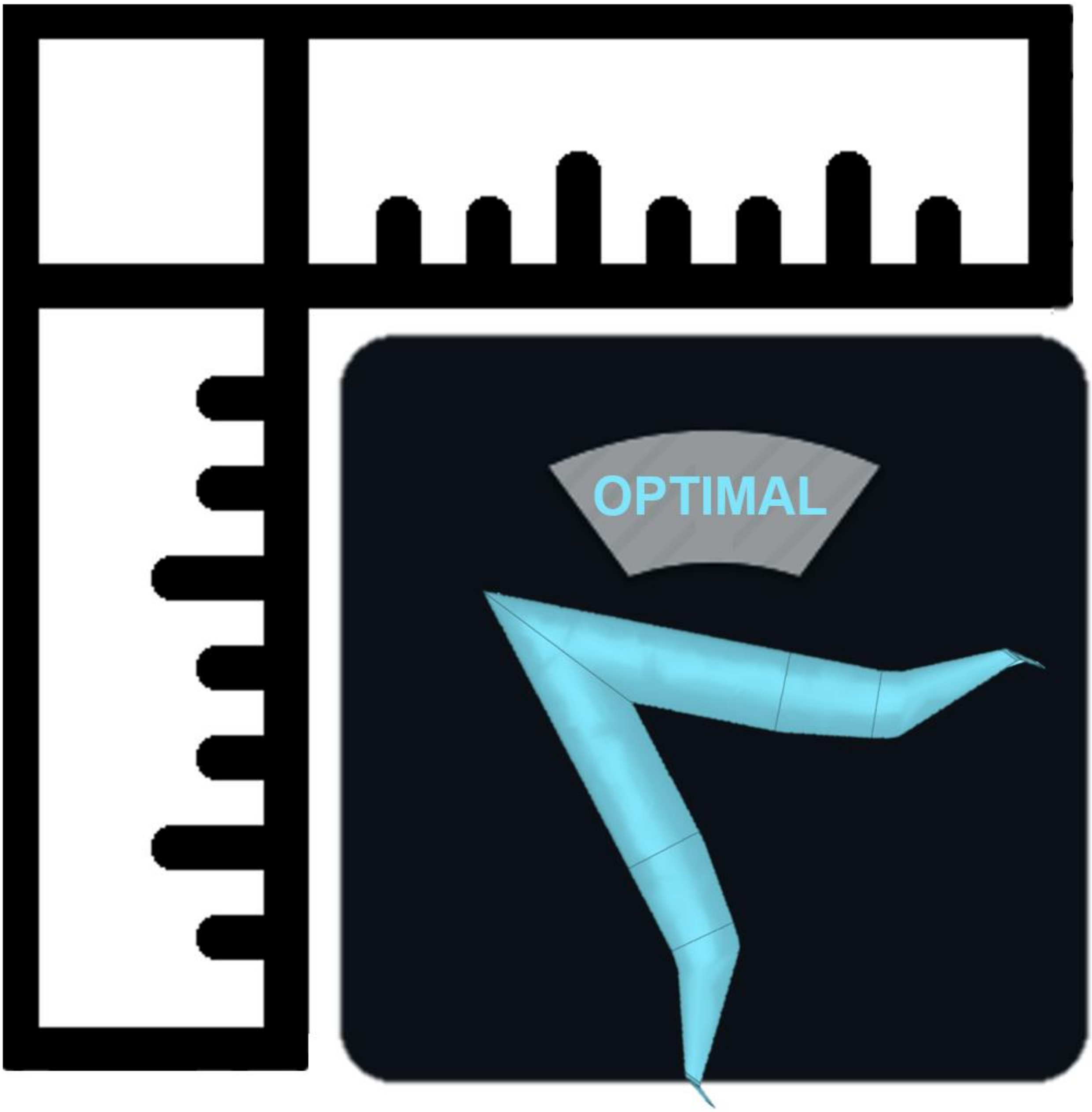

High-fidelity Structural Sizing Method for Weight Estimation of a Flying-V

by

Marloes Nanninga

To obtain the degree of Master of Science in Aerospace Engineering
at the Delft University of Technology.

to be defended publicly on Wednesday the 11th of January 2023 at 13:00.

Student number:	4547179	
Project duration:	December 2021 – January 2023	
Supervisors:	Dr. Ir. R. Vos,	TU Delft
	Dr. Ing. S.G.P. Castro,	TU Delft
Thesis Committee:	Dr. Ir. R. Vos,	TU Delft
	Dr. Ing. S.G.P. Castro,	TU Delft
	Dr. F. Oliviero ,	TU Delft
	Dr. Ing. J. Benad,	TU Delft
Total Equivalent Word Count:	$22,545+35\cdot 200=29,545$	

TU Delft

Contents

Nomenclature x

Summary xi

Ackowledgments xiii

1 Introduction 1
- 1.1 Oval-Fuselage Concept . . . 2
- 1.2 Structural Weight Estimation Methods . . . 3
- 1.3 Finite Element Analysis . . . 4
- 1.4 Structural Optimization . . . 5
- 1.5 The Flying-V Structure . . . 6
- 1.6 Flying-V Input Model . . . 9
  - 1.6.1 Numerical Model . . . 9
  - 1.6.2 Graphical Model . . . 9
- 1.7 Research Objective & Questions . . . 10
- 1.8 Thesis Outline . . . 11

2 Methodology 13
- 2.1 Structure Generation . . . 14
  - 2.1.1 Rib Generation . . . 15
  - 2.1.2 Spar Generation . . . 16
  - 2.1.3 Stringer Generation . . . 17
  - 2.1.4 Graphical User Interface . . . 18
- 2.2 Finite Element Model . . . 19
  - 2.2.1 Shape Generation . . . 19
  - 2.2.2 Mesh Generation . . . 20
  - 2.2.3 Finite Element Types . . . 21
  - 2.2.4 Material . . . 22
  - 2.2.5 Loads . . . 23
  - 2.2.6 Boundary Conditions . . . 24
  - 2.2.7 BDF File Generation . . . 25

3 Design Problem Definition 27
- 3.1 Sizing Variables & Initial Values . . . 28
- 3.2 Failure Criteria . . . 29
  - 3.2.1 Static yield strength . . . 29
  - 3.2.2 Structural Instabilities & Buckling . . . 29
  - 3.2.3 Fatigue . . . 30
- 3.3 Optimization Settings . . . 32
- 3.4 Design of Experiment Results . . . 33

4 Verification 35
- 4.1 Modal Analysis . . . 35
- 4.2 Mesh Convergence Study . . . 36
- 4.3 NASTRAN example - Cantilevered Plate . . . 36
- 4.4 Analytical Verification . . . 38

5 Results **43**
5.1 Initial Results 43
5.2 Baseline Results 44
5.3 Sensitivity Study 50
5.4 Design of Experiment Results 52
5.5 Weight Estimate 56

6 Conclusions & Recommendations **57**
6.1 Conclusions 57
6.2 Recommendations 58

A Code Documentation **59**
A.1 UML Diagram 60
A.2 Activity Diagrams 62

B Additional Verification Results **65**
B.1 Modal Analysis Results 65
B.2 NASTRAN Example - Numerical Results 70
B.3 Analytical Validation - Numerical Results 71

C BDF Files **73**
C.1 BDF Template Input Files 73
C.2 Example BDF File 74

D NASTRAN Cards **79**

E Additional Results Design of Experiments **87**

List of Figures

1.1 The multi-bubble fuselage concept [29]. 2
1.2 The integrated skin shell concept[29]. 2
1.3 The oval fuselage concept [29]. 2
1.4 Original, Leading-Edge Spar (LES), Oval fuselage cross-section concept [12]. 2
1.5 The No Leading edge spar (NLES) concept layout as proposed by Dotman [12]. 2
1.6 Process Flow of general Finite Element Analysis 4
1.7 Thickness [mm] plot showing the material thickness distribution after sizing of the structure [7]. 7
1.8 The process flow of the structural sizing method developed by Van der Schaft and Claeys [32], [7]. 8
1.9 Diagram showing the Flying-V planform according to the parametrization by Faggiano and the proposed parametrization by Hillen [17]. This proposed parametrization has been utilized in all research following Hillen. 10
1.10 Linear representation of the Flying-V as developed by Hillen [17]. 10
1.11 Non-linear representation of the Flying-V generated from the linear representation of Hillen, as developed by Van Luijk. 10

2.1 A concise process flow of the structural sizing method developed. 13
2.2 A detailed few of the process inside the ParaPy module of the methodology developed. 13
2.3 On the left the linear representation of the Flying-V as developed by Hillen [17]. On the right the non-linear representation of the Flying-V, constructed from the linear representation of Hillen, developed by Van Luijk. 14

2.4 Image showing the structure generation of the outer wing and winglet from left to right. Starting with the empty outer shell, adding the ribs, and next adding the spars and lastly adding the stringers as well. . . . 16
2.5 Spars as generated with the Spar Class. Zoom in on the spars connecting the wing and the winglet. 17
2.6 Spars as generated with the Spar Correction Class. Based on the spars, generated with the Spar Class. Zoom in on the spars connecting the wing and the winglet . . . 17
2.7 Diagram showing the basics of the stringer algorithm used for the stringer generation. . . . 18
2.8 Figure showing the Graphical User Interface with the outer wing structure and winglet structure loaded. The property view panel is opened to show the inputs for the outer wing structure. . . . 19
2.9 Image showing the shape modifications to the shape when removing the flap structure from the analysis. On the right, the full shape with flap is shown with the rib and spar planes used to split the elements such as to exclude the flap structure from the FEM shape. On the left the resulting flap shape is highlighted. . . . 20
2.10 Loading Diagram of a Conventional Aircraft. Created by Nieuwenhuizen [24]. . . . 23
2.11 Loading Diagram of a Flying-V. Created by Nieuwenhuizen [24] . . . 23
2.12 Spanwise lift distribution at the design lift coefficient. The black dashed line indicating the spanwise location that marks the transition from inner-wing to outer-wing. Created by Oosterom [25]. . . . 24

4.1 Mesh Convergence Plot . . . 36
4.2 Cantilevered plate model of NASTRAN [5]. . . . 36
4.3 Cantilevered plate thickness distribution results visualized in ParaPy. . . . 37
4.4 Cantilevered plate model of NASTRAN. . . . 38
4.5 Cross-section of the simplified outer wing model. . . . 38
4.6 Plot comparing the thickness distribution as approximated analytically versus the thickness distribution as a result from a SOL200 analyses generated by the framework developed in this research. . . . 40
4.7 The internal moment, in the simplified Flying-V outer-wing model, as calculated with the analytical method. . . . 41
4.8 The second moment of area around the x-axis of the simplified Flying-V outer wing model after sizing for thickness. . . . 41
4.9 Cantilevered plate thickness distribution results visualized in ParaPy. . . . 41

5.1 Von Mises stress plot in [Pa], showing the stresses in the skin. This shows the results from cycle 1, the stress in the initial design. . . . 44
5.2 Von Mises stress plot in [Pa], showing the stresses in the skin. This shows the results from cycle 4, after some improvements to the design have been made by the optimizer. . . . 44
5.3 Von Mises stress plot in [Pa], showing the stresses in the skin. This shows the results from cycle 14, the final design cycle, showing the optimized baseline design. . . . 45
5.4 The combined stresses inside the stringers, or beam elements, in [Pa]. For the final optimized design. . . . 45
5.5 Deformation plot in [m], showing the deformation of the outer wing. This shows the results from cycle 1, the deformation of the initial design. . . . 46
5.6 Deformation plot in [m], showing the deformation of the outer wing. This shows the results from cycle 14, the final design cycle, showing the optimized baseline design. . . . 46
5.7 Plot showing the thickness in [mm] of the optimized baseline design. Both the skin and the stringers are plotted. . . . 47
5.8 Plot showing the thickness in [mm] of the stringers of the optimized baseline design. . . . 48
5.9 Plot showing the thickness in [mm] of the spars of the optimized baseline design. . . . 48
5.10 Von Mises stress plot in [Pa], showing the stresses in the skin. This shows the results from cycle 14, the final design cycle, showing the optimized baseline design. . . . 49
5.11 Von Mises stress plot in [Pa], showing the stresses in the skin. This shows the results of the optimized NLES design. . . . 49
5.12 Von Mises stress plot in [Pa], showing the stresses in the skin. This shows the results of the optimized Baseline with Flap design. . . . 50

5.13 Von Mises stress plot in [Pa], showing the stresses in the skin. This shows the results of the optimized NLES with Flap design. 50
5.14 Plot showing the structural weight and layout parameters of the 5 layouts that resulted in the lowest structural weight and the 5 layouts that resulted in the highest structural weight, as a result of the design of experiments. The weight is indicated as a percentage of the baseline design weight. The stringer pitches, rib pitch, and orthogrid pitch are given in percentage w.r.t the baseline value. The stringer shape is indicated in binary. A value of zero indicates an L-shaped stringer, a value of one indicates a C-shaped stringer is used. The location of the spar is given as a percentage w.r.t the baseline value, zero indicates no spar is present. 53
5.15 Plot showing the structural weight and layout parameters of the average of the 5 layouts that resulted in the lowest structural weight and the average of the 5 layouts that resulted in the highest structural weight, as a result of the design of experiments. The weight is indicated as a percentage of the baseline design weight. The stringer pitches, rib pitch, and orthogrid pitch are given in percentage w.r.t the baseline value. The stringer shape is indicated in binary. A value of zero indicates an L-shaped stringer, a value of one indicates a C-shaped stringer is used. The location of the spar is given as a percentage w.r.t the baseline value, zero indicates no spar is present. 54
5.16 Top view of structure of the outer wing of Flying-V, as generated with the previous framework developed by Van der Schaft [32] and Claeys [7]. 56
5.17 Top view of the structure of the outer wing of the Flying-V, as generated with the framework developed in this thesis. 56

A.1 Part one of the UML Class Diagram of the Framework developed in this study. 60
A.2 Part two of the UML Class Diagram of the Framework developed in this study. 61
A.3 Activity Diagram showing the rib generation. 62
A.4 Activity Diagram showing the spar generation. 63
A.5 Activity Diagram showing the stringer generation. 64

B.1 First eigenmode of the baseline structure of the Flying V outer-wing. Deformation at frequency = 4.928E-05. 65
B.2 Section eigenmode of the baseline structure of the Flying V outer-wing. Deformation at frequency = 8.339E-07. 66
B.3 Third eigenmdoe of the baseline structure of the Flying V.Deformation at frequency = 2.064-05. 66
B.4 Fourth eigenmode of the baseline structure of the Flying V outer-wing. Deformation at frequency = 2.773-05. 67
B.5 Fifth eigenmdoe of the baseline structure of the Flying V. Deformation at frequency = 4.110E-05. 67
B.6 Sixth eigenmode of the baseline structure of the Flying V outer-wing. Deformation at frequency = 9.505E-05. 68
B.7 Seventh eigenmode of the baseline structure of the Flying V. Deformation at frequency = 3.713 . 68
B.8 Eighth eigenmode of the baseline structure of the Flying V outer-wing. Deformation at frequency = 8.338. 69
B.9 Ninth eigenmdoe of the baseline structure of the Flying V. Deformation at frequency = 16.391. . 69
B.10 Tenth eigenmode of the baseline structure of the Flying V outer-wing. Deformation at frequency = 19.6064. 70
B.11 Numerical Results of the NASTRAN Cantilivered Plate problem as analysed with the ParaPy based Framework developed in this research. 70
B.12 Numerical Results of the simplified Flying V outer-wing as analysed with the ParaPy based Framework developed in this research. Bending loads only. 71

C.1 BDF Template input file required for the framework to automatically write the full BDF file for NASTRAN. Here, an example of a template for the baseline sol200 analysis is shown. 74
C.2 First part of the BDF file generated by the framework developed in this study. This first part makes extensive use of the Template for the structure and includes the Executive control section and the Case Control section. 75
C.3 Second part of a BDF file generated by the framework developed in this study. The triple dots indicate that the NASTRAN statement on the previous line was repeated multiple times. This part shows the majority of the Bulk Section. 76

C.4 Final part of a BDF file generated by the framework developed in this study. The triple dots indicate that the NASTRAN statement on the previous line was repeated multiple times. This part show the final part of the Bulk Section. 77

D.1 The CBEAM Card [23]. Used for the stringers and stiffeners of the outer wing model. 79
D.2 The CQUAD4 Card [23]. Used for the majority of the skin elements. Requires rectangular mesh elements. 79
D.3 The CTRIA3 Card [23]. Used for the triangular skin elements. 80
D.4 The DCONADD Card [23]. Used to specify the constraints applicable to each subcase. The Design Constraint ID needs to be match with the Template DESSUB. 80
D.5 The DCONSTR Card [23]. Used to specify the individual design constraints. 80
D.6 The DESVAR Card [23]. Used to define a design variable. 80
D.7 The DOPTPRM Card [23]. Used to define the optimization settings. 81
D.8 The DRESP1 [23]. Used to link structural responses to constraints. 81
D.9 The DVPREL1 Card [23]. Used to link the design variable to a model property. 81
D.10 The EIGRL Card [23]. Used to activate buckling analysis using the Lanczos method. 81
D.11 The FORCE Card [23]. Used to define a point load. 82
D.12 The GRID Card [23]. Used to define the grid points of the finite element model. 82
D.13 The LOAD Card [23]. Used to specify the loads applicable to each subcase. The ID needs to be match with the Template LOAD ID. 82
D.14 The MAT1 Card [23]. Used to define the material properties. 82
D.15 The MDLPRM Card [23]. Used to request a H5 output file. 83
D.16 The MOMENT Card [23]. Used to define a moment. 83
D.17 The PARAM Card [23]. Used to specify the format of the output data. 83
D.18 The PBEAML Card [23]. Used to describe the shape of the stringers and stiffening elements. Linked to the CBEAM Card. 83
D.19 The PSHELL Card [23]. Used to model the skin and define the skin properties. 84
D.20 The RBE2 Card [23]. Used to define the Rigid Body Elements, used to resemble the ribs and to introduce loads and boundary conditions. 84
D.21 The SPC1 Card [23]. Used to define a single point constraint, as part of the boundary conditions. 84
D.22 The SPCADD Card [23]. Used to define a constraint set, to specify for each subcase the boundary conditions. Needs to match with the Template. 84
D.23 The SUPORT1 Card [23]. Used to define a additional constraint. Needs to be referenced in the Template. 85

E.1 Plot showing the structural weight of several different layouts as a result of a design of experiments. The weight is indicated as a percentage w.r.t. the baseline design weight. The stringer pitches, rib pitch, and orthogrid pitch are given in [m]. The stringer shape is indicated in binary. A value of zero indicates an L-shaped stringer, a value of one indicates an C-shaped stringer is used. The location of the spar is given in percentage of chord. If a value of zero is given, this means that the spar is not present. 88

List of Tables

1.1 Design requirements for the FV-1000. 9
1.2 Main input values for the FV-1000. 9

2.1 Main input parameters for Layout Generation 15
2.2 Element Geometry Test Tolerances used by NASTRAN at the start of an analysis during a Geometry Test. 21

2.3 Material properties of AL 2024-T351 23

3.1 Sizing Variables 28
3.2 Fatigue-life prediction model parameters. Used for the model developed by Al-Rubaie [1] 31
3.3 Standardized load spectrum developed by NLR indicating the expected exceedance frequency per 40,000 flights [10]. 31
3.4 Overview of the layout parameters that are varied in the design of experiments. The location of the spars is given as a percentage of chord. The stringer shape value relates to the stringer shape, zero is an L-shaped stringer, one is a C-shaped stringer. 33

4.1 Verification FEA results. Here, the simplified model refers to the rectangular model, skin only, and the full model refers to the baseline design, including skin, stringers, spars, winglet, and the true loads etc. 42

5.1 Baseline Results, comparing the NLES design with the baseline design. The Flap model does not include the weight of the Flap. 49
5.2 Sensitivity Study Results. The fraction indicates the FEA weight fraction of the specific design compared to the baseline without minimum gage values for the design variables. 50
5.3 Sensitivity Study on the Stress Concentration Factor used for Fatigue analysis. 52

Nomenclature

General Abbreviations

AVL	Athena Vortex Lattice
BC	Boundary Condition
BDF	Bitmap Distribution Format
BWB	Blended Wing Body
CAD	Computer Aided Design
CFD	Computational Fluid Dynamics
CFRP	Carbon Fibre Reinforced Polymer
CG	Center of Gravity
CSM	Computational Structural Model
DESVARS	Design Variables
DOF	Degree of Freedom
DSG	Design Service Goal
EID	Element Identifier
EMWET	Elham Modified Weight Estimation Technique
FEA	Finite Element Analysis
FEM	Finite Element Method
FSD	Fully Stressed Design
FV	Flying-V
GUI	Graphical User Interface
HLP	High Level Primitive
ID	Identifier
KBE	Knowledge Based Engineering
L/D	Lift-over-drag ratio
LES	Leading Edges Spar
LE	Leading Edge
LHS	Latin Hypercube Sampling
MDO	Multi-Disciplinary Design Optimization
MPC	Multi Point Connector
MPC	Multipoint constraint equations

MTOM	Maximum Take-Off Mass
MTOW	Maximum Take-Off Weight
NLES	No Leading Edges Spar
NLR	Netherlands Aerospace Centre
OEM	Operational Empty Mass
OEW	Operational Empty Weight
OOP	Object-Oriented Programming
PLC	Programmable Logic Controller
RBE	Rigid Body Element
RBF	Radial Basis Function
TAW	Tube-and-Wing
TE	Trailing Edge

Summary

The Flying-V is an unconventional aircraft concept showing promising initial results in overall efficiency, outperforming the conventional tube-and-wing aircraft. To prove this gain in efficiency, optimized concepts are desired early in the development process. This requires flexible design tools that explore and optimize the design space. For this, a multidisciplinary design optimization tool is developed, in a Python-based parametric software that uses object-oriented programming and knowledge-based engineering, ParaPy. A representative high-fidelity structural weight estimation method is still missing from this tool, as recently, the parametrization of the outer mold line of the Flying-V has been altered to ensure cabin design flexibility, improve manufacturability, and enable a family concept.

This research contributes to the design of the Flying-V by presenting a framework that combines a fully parametric structure design tool with high-fidelity structural analysis, enabling automatic weight estimation of multiple optimized structural concepts. A structural model is automatically generated in ParaPy, requiring only the outer mold line as input. Optionally, default parameters on the structural layout, like the location of spars or the rib pitch, can be altered, allowing for thorough design space exploration. Next, all elements in the structural model are assigned element properties, the structure is meshed, and boundary conditions are applied. The design problem is defined, and a NASTRAN input file is written. NASTRAN SOL200 is used to perform a structural sizing optimization. The objective of the optimization problem is to minimize the structural weight based on a gust load, with constraints on both yield strength and fatigue. The results are post-processed by the ParaPy application, enabling a feedback system. The entire process is automated and a weight estimate, with thickness distribution, is generated as output.

A design of experiments is performed that shows a success rate of 90% and proves the flexibility and robustness of the framework developed. Moreover, the framework is fully automatic, has seamless integration with the existing multidisciplinary design optimization tool, and enables a full feedback design loop. This shows that the framework is suitable for the analysis of the full Flying-V structure. Furthermore, as the framework requires only the outer shape as input and uses the knowledge base to generate the structure and the finite element model, the framework can be expanded for structural weight estimation and design space exploration of other (un)conventional aircraft concepts. Currently, the main limitation of the framework is the lack of buckling analysis.

The framework is used to estimate the structural weight of the outer wing of the Flying-V. First, multiple concepts that are currently considered in the design of the Flying-V are compared. A Non-Leading Edge Spar design is estimated to be 15% heavier compared to the more conventional wing box structure design. The trailing edge of the outer wing is lightly loaded, and the implementation of a flap is shown to increase the structural efficiency, leading to a weight reduction of up to 20%. Fatigue is the critical failure mode, and the design of experiments shows a weight-saving potential of up to 30% by relocating the spar. The FEM weight of the baseline design is $2400[kg]$, such that the final, engineering weight of one outer wing is estimated at $3.0 * 10^3[kg]$, when including weight penalties for buckling and manufacturing as well. This is 20% lower than the weight as estimated by previous work, indicating a potential reduction in the total structural weight of over 15% compared to conventional reference aircraft. These results are promising and bring the Flying-V one step closer to reality and help bridge the gap to more efficient aircraft.

Acknowledgements

A little over six years ago, after long deliberation, I made the choice to study aerospace engineering. I immediately felt right at home in Delft, and the like-minded people and the inspiring projects all around me, motivated me to study hard. My time as a student went by quickly, all thanks to this incredible environment. The completion of this thesis marks the end of my time as a student, and I cannot possibly thank everyone who helped me make the most out of it. However, I would like to take the time to thank the people who helped me during my thesis.

Many thanks to my main supervisor, Roelof Vos. Although Roelof was on sabbatical most of the time, I have always enjoyed the meetings we had together. Furthermore, Roelof was the one to offer me a thesis subject right up my ally, and I am thankful for this opportunity. A special thanks to Saullo Castro who jumped in to supervise me. I truly learned a lot, and I could always feel his enthusiasm for the subject. I am grateful for all the help I got from Srikanth Vasudevan. Although our meetings were irregular, the replies to my questions were always quick and elaborate, more than I could hope for. Without the help of ParaPy, I would not have been able to truly showcase the state-of-the art of parametric engineering. Reinier van Dijk and Max Baan made time in their busy schedules to both supervise and assist wherever needed. Moreover, the time spent at the office were one of my most productive hours due to the hard-working office culture at ParaPy. Many thanks, for offering this support.

The most useful and motivating conversations were often with other students involved in the Flying V project. Thanks for all the help and comforting words during the difficult times of the project. Time to relax and unwind was also crucial during my thesis, and outside my thesis I got to enjoy unforgettable experiences. Hereby, I would like to thank all my friends, teammates, and family for putting up with all my difficult explanations and complaints.

Now, I am curious what the future holds. All I can hope is to find an environment that will inspire me just as much as the Delft campus area. On to the next challenge!

Marloes Nanninga
Delft, December 2022

1

Introduction

To limit global warming, a reduction in transport emissions of 90% by 2050, compared to 1990-levels, is required by the European Commission [31]. This Green Deal is a real challenge for the aviation industry, as aviation is one of the fastest-growing sources of green-house gas emissions. Even though, the amount of fuel burned per passenger has dropped by 34% between 2005 and 2017, the total emissions for the aviation industry have increased due to an increase in demand. To reach the goal set by the Green Deal, commercial aviation must become even more efficient in the upcoming years. However, improving the efficiency of the conventional tube-and-wing concept is becoming increasingly difficult [21]. Meanwhile, unconventional aircraft concepts show potential to further improve efficient. The Flying-V is one of the unconventional concepts for commercial aircraft design that shows promising initial results on overall efficiency [2]. Indicating that the Flying-V could potentially help reduce emissions of the aviation industry to reach the Green Deal requirements.

There are many more unconventional aircraft concept designs that could potentially be more efficient than the tube-and-wing concept. However, most of these designs have never become more than a sketch. The tube-and-wing aircraft concept did become the conventional aircraft during the first and second world war, when there was a need for fast production of reliable aircraft. The tube-and-wing aircraft proved the most reliable at that time, as many alternative concepts failed due to stall or other stability and control issues. In 1988, NASA saw the limitations to one conventional aircraft, as already only marginal improvements were made to the tube-and-wing aircraft. In response, NASA asked aircraft designers to see if there existed unconventional aircraft concepts that showed potential for improved efficiencies [19]. This spiked the interest in unconventional aircraft design and led to the first fundamental developments of blended wing body concepts. However, developing the alternative concepts was more complicated than anticipated and the current state-of-the-art in commercial flight, the Airbus A350 and the Boeing 787, still follow the conventional tube-and-wing concept. Now, with an increasing need to improve aviation efficiency, popularity around unconventional aircraft concepts has risen again.

In 2015 Benad founded the Flying-V concept in collaboration with the TU Berlin and the Future Projects Office of Airbus [2]. Contrary to conventional aircraft design, in the Flying-V, the payload is located in the aerodynamic lifting surface. Instead of splitting the aircraft into a fuselage designed purely for the transport of payload and a wing for aerodynamic performance only, one body fulfils both tasks. This potentially reduces the wetted area of the aircraft and increases the structural efficiency due to a greater similarity between payload distribution and lift distribution. This could be beneficial as this leads to lower bending moments due to shorter moment arms, resulting in increased efficiency and decreased fuel burned per passenger [3]. Currently, the Flying-V is headed for a design that is expected to be 20% more efficient than the current most efficient passenger aircraft, the airbus A350.

The dual functionality of the aircraft body is not unique to the Flying-V. However, the Flying-V has some great advantages that make it a promising concept. The original Flying-V concept consists of two highly swept pressurized cylinders arranged in a V-shape, with an airfoil-shaped shell constructed around it. The high sweep angle creates an elliptical cross-section when making a streamwise cut. This allows for a relatively low thickness-to-chord ratio for the airfoil whilst still allowing a spacious passenger cabin [2]. Compared to other alternatives, the Flying-V aircraft allows for easier evacuation and increased passenger acceptance, as passengers are likely closer to windows. Moreover, there is no need for high lift devices due to a sufficiently large wing area, and with the newest developments on a relatively simple family concept for the Flying-V, another advantage has presented itself. All advantages combined; a more attractive alternative is hard to find.

1.1. Oval-Fuselage Concept

Another advantage of the Flying-V is the application of the oval fuselage cross-section. The oval fuselage cross-section is an alternative non-circular pressurized fuselage concept that allows for higher space efficiency and structural efficiency. As aircraft designs moved away from circular shaped fuselages, a need for non-circular pressurized fuselages arose. The structural design of a non-circular pressurized fuselage is difficult to realize without the addition of considerable weight or reduction in passenger comfort. The first non-circular pressurized fuselage design are the multi-bubble fuselage concept and the integrated skin shell concept. The novel oval fuselage concept combines the advantages of both the multi-bubble and the integrated skin shell concept[29], as the outer skin and the inner trapezoidal structure take up the pressurization loads, and a large cabin space remains. The design allows for more flexibility than a conventional circular fuselage without introducing any bending loads in the skin, as the trapezoidal structure takes up all bending loads. The oval fuselage cross-section is used in the Flying-V.

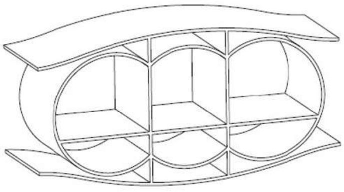

Figure 1.1: The multi-bubble fuselage concept [29].

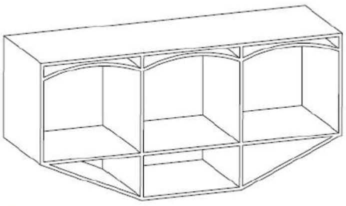

Figure 1.2: The integrated skin shell concept[29].

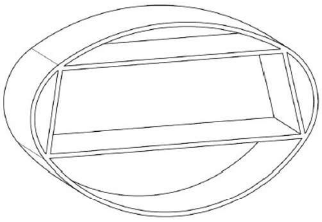

Figure 1.3: The oval fuselage concept [29].

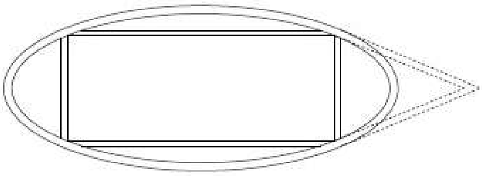

Figure 1.4: Original, Leading-Edge Spar (LES), Oval fuselage cross-section concept [12].

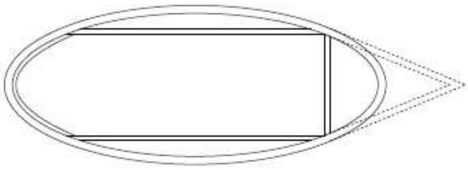

Figure 1.5: The No Leading edge spar (NLES) concept layout as proposed by Dotman [12].

In the latest research on the structure of the Flying-V, Dotman used a new parametrization and compared an oval fuselage concept with four walls with a concept that lacks a leading-edge spar, the Non-Leading-Edge Spar (NLES) concept [12]. The Non-leading Edge Spar concepts is considered as a leading-edge spar might not be required due to the lack of leading-edge devices and because the removal of the leading-edge spar in the cabin area could increase the space available for passengers. Removing the leading-edge spar would allow for passengers to get a more spacious feeling inside the Flying-V and would open up the possibility for windows in the leading edge. Both the original, Leading-Edge Spar (LES) concept, in Figure 1.4, and the NLES concept, in Figure 1.5, are still considered for the Flying-V, as no conclusive results on the relative structural efficiency of the NLES concept exist.

1.2. Structural Weight Estimation Methods

The Flying-V concept is developed using a Multidisciplinary Design Optimization (MDO) tool. A design engine for the entire aircraft concept is developed within the Python-based Knowledge-Based Engineering (KBE) environment: ParaPy[1]. With recent updates to the concept regarding cabin design flexibility and manufacturability, the structural representation in ParaPy is outdated. Without the structural representation and due to the lack of relevant statistical data on aircraft weight, an accurate weight estimation still needs to be included. Different methods for weight estimation exists.

A popular weight estimation method is the classification system for aircraft weight estimation developed by Elham [13]. Four categories are identified:

- Class I method: The mass of each aircraft component is defined as a fraction of the maximum take-off mass of the aircraft based on a statistical analysis of existing aircraft.
- Class II method: Empirical equations are utilized to calculate the mass of every fundamental component. More input on the design of the aircraft is required. However, a more detailed weight estimate is generated.
- Class II & 1/2 method: Basic analytical structural analysis is performed to estimate the material required to withstand the loads. Mostly limited to strength and stiffness analysis, statistical data may still support the analytical calculations.
- Class III method: Finite Element Method is used to calculate the mass of the aircraft. Again, Additional analytical and empirical methods are used to support the mass estimation of non-primary structures. This method requires a high number of design parameters as input and returns a detailed model weight distribution.

Class I and Class II methods often prove to be sufficient for conceptual design and the first preliminary design steps. These methods are ideal due to the low number of design inputs required. However, these weight estimation methods are inaccurate for unconventional aircraft design due to the limited amount of relevant statistical data available. More sophisticated weight estimation methods like the Class II & 1/2 and Class III methods are needed to give relatively accurate weight estimates for highly unconventional concepts. The Flying-V structure is complex, and the application of Class II & 1/2 methods is difficult. The Class III method is more flexible and allows for sensitivity analysis, which can be used for comparison and optimization of the concept as well[9]. Therefore, the Class III method, using Finite Element Analysis (FEA), is a good fit for weight estimation of unconventional aircraft concepts. Multiple aircraft manufacturers and research centres have used FEA to develop tools for mass estimation of unconventional wings or aircraft. However, most, if not all, of these tools have been developed using in-house software and are unavailable for public use [8].

---

[1] https://www.parapy.nl/ [cited on 29-10-2022]

1.3. Finite Element Analysis

Finite Element Analysis is not only used as a Class III weight estimation method. Rather, FEA is often used as structural analysis tool, for design and sizing of complex structures. Due to the high redundancy within complex structures, large sets of linear algebraic equations should be solved simultaneously, which requires approximations when no use is made of FEA. FEA is so powerful, that its introduction is considered the second industrial revolution due to its great consequences for design [6]. FEA tools use a finite element method (FEM) to approximate a distribution of field variables [20]. In FEA, first, the problem, often the geometry model, is divided into small pieces, called elements. Then, the governing, continuous, equations are approximated by applying linear functions to each element. A residual function is used to solve the discretized problem. Generally, the procedure of performing a FEA consists of nine steps:

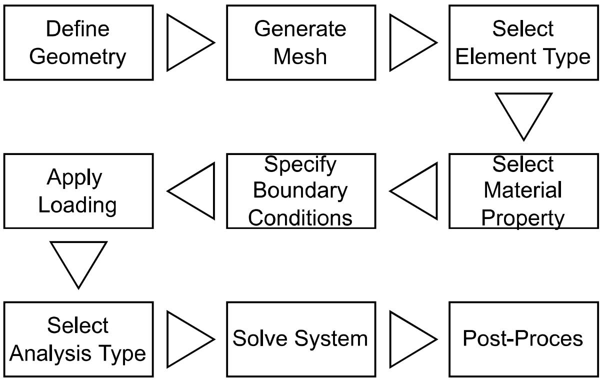

Figure 1.6: Process Flow of general Finite Element Analysis

Often, multiple different software packages are used for each step in FEA. A graphic user interface (GUI) is desired, especially, in the first steps of the analysis. An external Computer Aided Design (CAD) software is commonly used for the creation of the geometrical model. The geometrical model is often exported to a different discretization tool, which can be part of the FEA software. Discretization, or mesh generation, is considered a time-consuming and complex task, as fully automated mesh generators for general geometry are not yet available. There are different element types one can use for the discretization of the problem. The most versatile element is the 3D element, which can be used to model all types of structures. The downside of a 3D element is the high computational costs due to many Degrees of Freedom (DOFs). By simplifying the problem and making use of 2D or 1D elements, the amount of DOFs can be limited, whilst modelling quality can be maintained. The choices on the CAD geometry, the discretization, and the element type, all influence the modelling quality and should be tuned for the analysis type that is applied. If a CAD model represents a beam as a 3D solid, 3D solid elements could be chosen to analyse the beam, which allows for an analysis with more DOFs. This will result in more accurate results compared to a CAD model that represents a beam as a line, and 1D elements are chosen to analyse the beam. Some types of analysis require a higher number of DOFs than others, and 1D elements might not be sufficient to capture all structural failure modes. A detailed CAD model with all solid elements might be required for some analysis, whilst for other analysis a simple stick model will suffice. Thus, there is a strong connection between CAD model, discretization, element type, the accuracy of the analysis and the analysis type. The choice should be well considered before setting up the analysis.

Element connectivity is another important part of mesh generation as this is later used for the FEM equations, and the analysis will fail if not all elements are connected properly. Moreover, the quality of the mesh is influenced by the distortion of the elements, and thus, distortion of elements should be checked and limited. Once the discretization is performed, element properties can be defined for (a group of) elements by specifying which properties apply to what regions of the geometry. Again, this step is often done with the use of a GUI. The boundary and loading conditions are different from problem to problem and need to be assigned to the corresponding elements. Once all element properties are specified, the problem and analysis type are defined, the solver can start. After the solver has completed the calculations, the data generated by the solver must be post-processed. The solver has produced data on all requested entities like stresses, strains, deformations, and eigenvalues. All information can be projected back on the original geometry. One still must interpret these results and evaluate the quality of the model and make the translation to the real problem at hand, to check if the designed product fulfils all requirements. Stress plots, displaying the stress on the mesh, are often useful results. However, one might also be interested in partial results or internal stresses to generate freed-body diagrams for further analysis outside the FEA. Connecting the results to the original geometry is not straight forward and requires good bookkeeping and consistency in the entire process.

All these steps combined make FEA a complex and time-consuming task, often involving a lot of human interaction. There are CAD packages which combine all steps of the FEA, reducing complexity, however these are mostly limited in the analysis types and general functionalities. There are different types of FEA solvers. Linear FEA solvers, for example, are only able to perform linear analysis. General-use structural FEA solvers are not limited to one type of solution and can perform both linear and non-linear analysis, and static or dynamic analysis. In this study, a validated general-use FEM solver will be used to enable future application into aeroelastic analysis. NASTRAN is a state-of-the-art general-use FEA solver and is one of the first FEM programs ever. It was developed by NASA in the 1960s and the name comes from NASA STRuctural ANalysis, and today NASTRAN is the benchmark used in the aerospace industry. NASTRAN needs a BDF file as input to start the simulation. The BDF file can be generation through a GUI in PATRAN, the pre- and post-processing software developed for NASTRAN. The use of PATRAN is not required, and different means can be used to generate the BDF file. The BDF file is written in FORTRAN, a general-purpose coding language suited for numerical computation. Writing a BDF file can be automated making use of Python and the PyNastran module, especially developed for combining Python and NASTRAN.

1.4. Structural Optimization

In order to use NASTRAN, or other FEA tools, to make an accurate weight estimation of a concept, structural sizing, and ideally, optimization has to be performed. In structural optimization the best material distribution within a physical space is determined, sized by the loads that the structure must withstand. In general, there are three different types of structural optimization: size, shape, and topology optimization.

Topology optimization is the most general form. In topology optimization, there is still a lot unknown about the structure to be designed, and the main input for the optimization are the boundary conditions and applied loads. For a large and complex structure, results in a lot of design variables. Defining proper boundary conditions that prevent the optimization from resulting in unrealistic structural designs that are hard to manufacture, is a complex task and requires plenty of time and resources. A full topology optimization is computationally expensive and therefore often avoided in the design of larger structures like that of an entire aircraft. Topology optimization can be used in the detailed design of parts of the structure. An important study that uses a ground structure approach to include structural topology optimization for creation of the initial structural layout, is performed by Yang et al. [34].

Shape optimization is uncommon in full aircraft structure design and is used when the shape or boundary of a structural domain is unknown. Through optimization, the shape of the structure will be determined. Mainly applicable to individual elements where the design is driven by the space available. In size optimization, the size of the components of the structure is yet to be determined. However, the structural layout is already determined, and all other aspects of the structure except size are known. This form of structural optimization is most frequently used in aircraft structural design as it is less computationally expensive than a full topology optimization, however it is still an efficient way to reduce structural weight. Klimmek et al. [33] used size optimization after proposing an initial design.

There are multiple ways to perform a size or topology optimization. An intuitive method that is often used is the Fully Stressed Design method. In a fully stressed design, each member of a structure that is not bound by minimum thickness, must be fully stressed under at least one of the design load conditions [28]. From this, it follows that the absolute maximum stress and the minimum thickness constraints drive the design of the structure. Material is removed until all elements are fully stressed or are limited by a minimum gage constraint. This assumes that by changing the thickness of an element, there is only a limited effect on the rest of the structure. Iterations are required to get to a converged solution and take the effect of the response of the rest of the structure into account.

Using the FSD methods allows solving structural design optimization problems without the need for sensitivity analysis or complex optimization algorithms. Another advantage of using FSD is that it can handle many independent design variables, thousands of them [18]. The FSD method can be implemented within the MSC NASTRAN SOL200 environment. When setting a positive value to the maximum number of FSD cycles, the FSD function will be used in the SOL200 function.

The SOL200 module of NASTRAN is the industry standard for structural optimization by sizing of element thickness. NASTRAN SOL200 uses polynomials as the shape functions. The design variables are the coefficients of the polynomials. This unfortunately means that a positive thickness of all sized elements cannot be guaranteed, thus lower bound constraints must be imposed on the element thickness. Moreover, NASTRAN uses the finite difference method for sensitivity analysis. The accuracy of the sensitivity depends on the step size. This should be kept in mind during the design. NASTRAN SOL200 uses the eigenvalues of the whole structural stiffness matrix to analysis buckling, a global buckling approach. This means that the entire structural model must be designed as accurately as possible to prevent excessive buckling because of the large number of degrees of freedom. More importantly, this implies a high computational cost for the buckling analysis.

1.5. The Flying-V Structure

NASTRAN has been used for weight estimation of the Flying-V before, by Van der Schaft, and Claeys [32], [7]. First, preliminary research on the development and analysis of the Flying-V structure was performed by Van der Schaft. Claeys used the tools developed by Van der Schaft to estimate the structural mass of the Flying-V and compare it with the current state-of-the-art of conventional commercial aircraft, the Airbus A350. A primary structure concept was developed based on expected load paths. The LES oval fuselage concept was used in this initial structural design, and a CAD model of this primary structure was generated in ParaPy. A FEA was used to analyse the structure after the Flying-V structure was deemed too complex for efficient analytical analyses.

The behaviour of the structural model is analysed by looking at the stresses within the structure using a uniform thickness everywhere. From this analysis, the following conclusions can arise:

- The stress increases towards the root due to an increase in the internal bending moment.
- Bending relief occurs as higher local stress values are found for an OEM analysis than for a MTOW analysis.
- High stresses occur at the wing kink due to discontinuities.

The most important takeaway from the research from Van der Schaft is that the primary load path in the Flying-V runs from the outboard wing front spar to the root trailing edge. The results also show some challenges to the structural design of the Flying-V. The so-called wing-kink section and the nose-fuselage section need additional structural elements to achieve convergence. Claeys adjusted the critical sections by adding reinforcements and proved the feasibility of the Flying-V structure. The Flying-V structure was favourable over the Airbus A350 structure, with an estimated reduction in weight of 17%. It is important to note that Claeys did not consider fatigue, and failure criteria were only based on yield or ultimate strength and buckling requirements. Claeys found buckling to be the critical failure mode.

Taking a closer look at the structure of the outer-wing, including the wing-kink section, the sudden jump in wing box height becomes clearly visible, as can be seen in Figure 1.7. This sudden decrease in height greatly reduces the bending moment, resulting in the height stresses and need to increase the skin thickness. On top of that, the rib spacing might cause the high stresses in the inside of the kink, where all ribs come together. As here, the local structure mass, and likely local stiffness, is higher than the surroundings. A smoother transition from inner-wing to outer-wing is likely to decrease the stresses at the kink, so by re-evaluating the height changes in the wing box and the placement of the ribs, this section can possibly become more efficient.

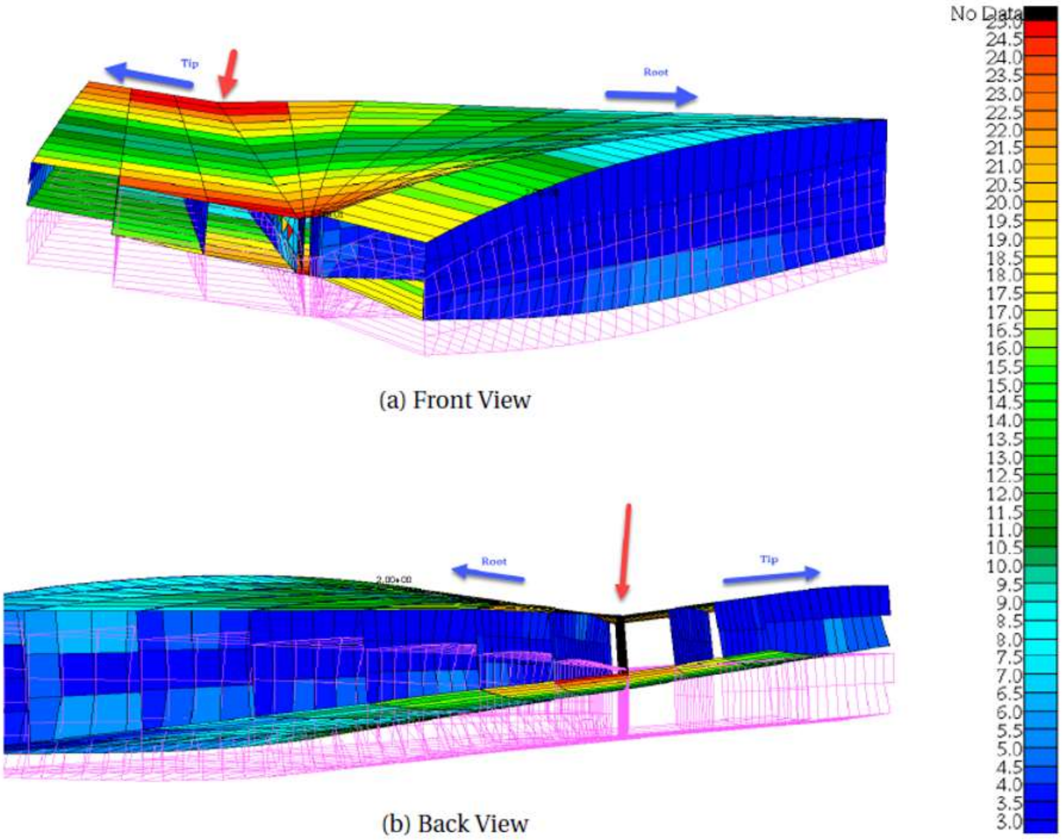

(a) Front View

(b) Back View

Figure 1.7: Thickness [mm] plot showing the material thickness distribution after sizing of the structure [7].

In Figure 1.8, a simplified process flow of the structural sizing method developed by Van der Schaft and Claeys can be seen. A total of six different software packages are used. A combination of the commercially available software PATRAN and NASTRAN is used for the FEA. Additionally, use is made of Airbus in-house software for multiple steps in the sizing method. ODILILA is Airbus's in-house software that is used to find the aerodynamic loads. ZORRO is an essential pre-processing module, which is again an Airbus in-house tool. ZORRO-X provides inertia mapping, including the balancing of the aircraft structural model. Moreover, ZORRO-X performs aero mapping using Multiple-Point Connectors (MPCs). As the aerodynamic mesh nodes do not coincide with the structural mesh nodes, the aerodynamic loading must be interpolated from aero mesh to structural mesh. Other functionalities of ZORRO-X include mesh refinement and solving for model imperfection. ZORRO-M is used to generate the design criteria for the composite materials used in the analysis of Claeys. ZORRO-M also updates the material thickness and is crucial for the sizing process and buckling analysis.

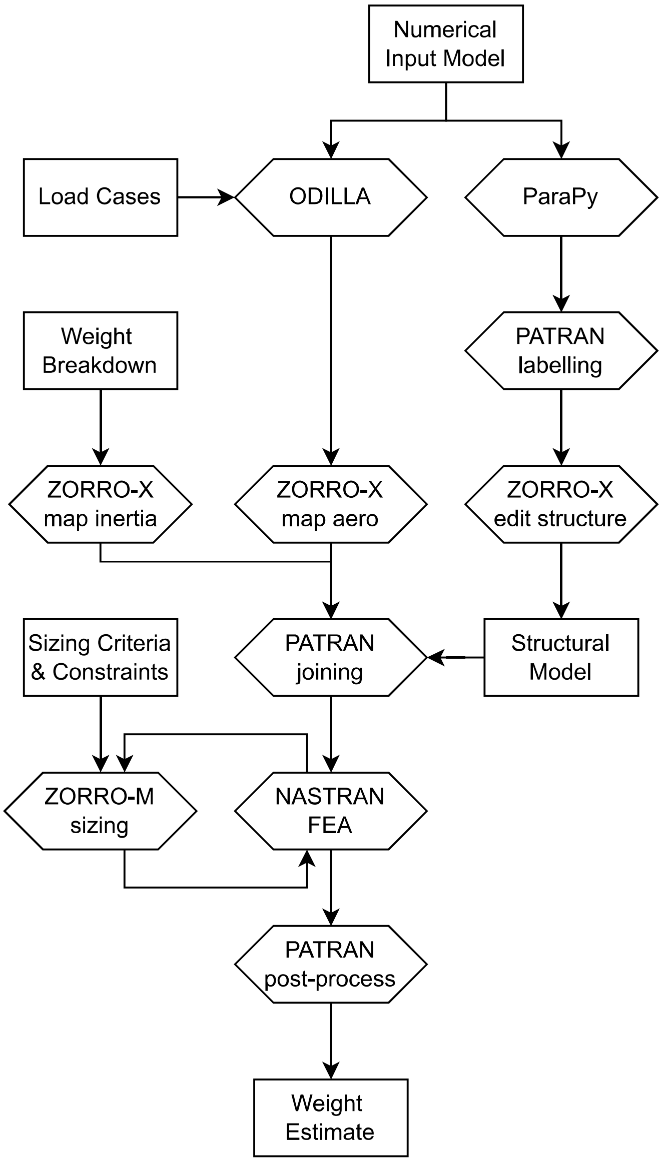

Figure 1.8: The process flow of the structural sizing method developed by Van der Schaft and Claeys [32], [7].

Not only is the use of the Airbus software a limitation to the development and accessibility of the sizing tool, but there are also more disadvantages to the tool developed by Van der Schaft and Claeys. The use of software packages of Airbus, limits design freedom, as the pre-processing software can only handle wing or fuselage sections. Manual adjustments were required at multiple points in the process flow to guarantee an outcome. Additionally, due to the use of multiple different software packages, multiple formatting issues did occur, and manual input was required. Moreover, the computational efficiency was reduced due to file sharing between the different software packages. Another downside to the tool is that using PATRAN as a pre-processor prevents a closed design loop. PATRAN uses PCL as a programming language instead of Python, as used by ParaPy, which results in integration difficulties. One of the main difficulties is the different mesh element identification numbers between ParaPy and PATRAN, which makes feedback of the results almost impossible. Other than the software choices, modelling choices can also be criticized. The structural model analysed by Van der Schaft and Claeys is generated based on the design guides of Airbus, and no sensitivity studies on the structural layout are performed. The developed structural model generator is limited in design freedom and is, for example, limited to conventional wing box structures, where the leading edge is crucial. This does not allow for evaluation of, for example, the NLES concept.

The results from Van der Schaft and Claeys gave new insights into the structure of the Flying-V concept. However, further research was required to understand the Flying-V's structural behaviour better. Dotman developed a new structural sizing methodology for the constant cross-section of the wing-fuselage section of the Flying-V [12]. Due to focus on increasing understanding instead of optimization or automated design, no use has been made of KBE or ParaPy by Dotman. Instead, Megson's [15] boom method was applied to determine the stresses in the longitudinal direction, whilst an enriched 2-dimensional finite element method was used to determine the stresses in the cross-sectional plane. The sizing and analysis loop required a substantial runtime and allowed for little design flexibility. Nevertheless, an extensive load case study was performed, and fatigue and structural instabilities were analysed in detail. Both buckling and fatigue are critical, and the fuselage floor proved the most critical structural element. A new parametrization of the oval fuselage section was used, and the conventional oval fuselage design was compared to an NLES oval fuselage cross-section. The NLES, so far, has shown to be a viable alternative; however, no conclusive results were shown.

1.6. Flying-V Input Model

This section specifies the Flying-V model and parametrization used as input for the structural model used in this thesis.

The FV-1000, the largest aircraft of the family, will be used for the development of the structure. The family designed by Oosterom consists of all common parts, with the only difference between the FV-800, FV-900 and FV-1000 being the addition of constant fuselage sections. It is assumed that because the FV-1000 is the largest aircraft, the common structure will be sized by the loads acting on the FV-1000. However, this should be verified in later developments. It is assumed that the structure of the outer wing is sized by the FV-1000.

The design requirement used for the Flying-V model will be equal to the design requirements used by Oosterom [25] and Nieuwenhuizen [24]. The design requirements are summarized in Table 1.1.

Requirement	Value	Unit
Passengers	378	[−]
Cruise Mach	0.85	[−]
Design Range	15350	[km]
MTOW	280	[10^3 kg]

Table 1.1: Design requirements for the FV-1000.

Requirement	Value	Unit
Angle of Attack	2.45	[°]
Total Span	65	[m]
Outer Wing Span	14.75	[m]
Winglet Height	7.0	[m]

Table 1.2: Main input values for the FV-1000.

1.6.1. Numerical Model

The input parameters are in line with the optimized baseline as used by Van Luijk, the latest research on aerodynamic shape optimization of the Flying-V. The main input values can be found in Table 1.2.

1.6.2. Graphical Model

The Flying-V planform was first parameterized by Faggiano. This parametrization was purely focused on aerodynamic design and was defined by streamline cutting planes. Hillen developed a new parametrization to improve cabin design flexibility and manufacturability. A linear representation of the Flying-V is the result, using linear lofted wing trunks for the 3D model.

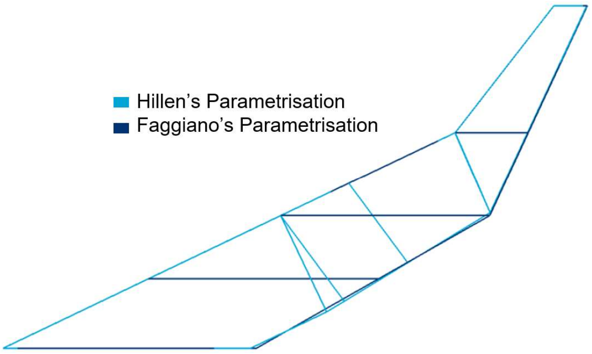

Figure 1.9: Diagram showing the Flying-V planform according to the parametrization by Faggiano and the proposed parametrization by Hillen [17]. This proposed parametrization has been utilized in all research following Hillen.

This Linear representation is used as the starting point for the structure and outer shell definition. However, the linear lofted wing trunks are replaced by gordon surfaces, and a non-linear model is generated. This is in line with the adjustments Van Luijk made to the model. The adjustments are needed to prevent both an undesirable aerodynamic and structural analysis, due to the steep drop in wing thickness at every section. The Flying-V can be divided into 5 sections: The nose-fuselage section, including the constant cross-section fuselage, the inner-wing section, the outer-wing section, and the winglet.

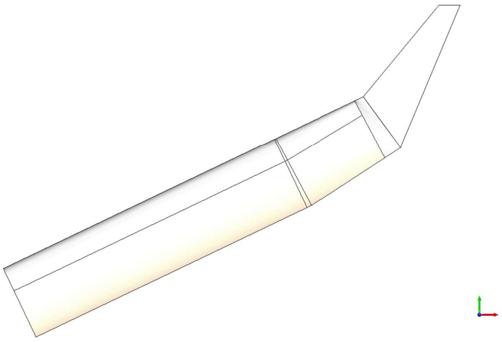

Figure 1.10: Linear representation of the Flying-V as developed by Hillen [17].

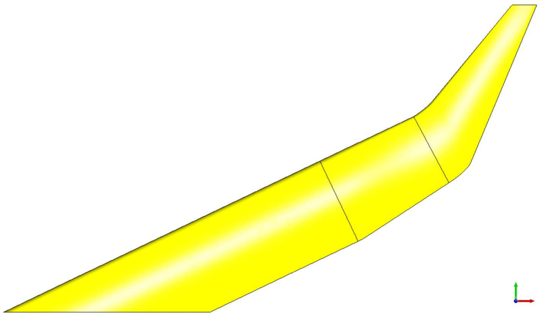

Figure 1.11: Non-linear representation of the Flying-V generated from the linear representation of Hillen, as developed by Van Luijk.

1.7. Research Objective & Questions

From the previous sections, it shows there is a need for a flexible yet accurate structural weight estimation tool that allows for concept comparison and optimization of unconventional aircraft. As, an accurate and design sensitive weight estimation is often missing in the early development stages of an unconventional aircraft. The same holds for the Flying-V. Whilst weight is one of the driving factors for aircraft design, an accurate weight estimate is this is still missing from the Flying-V design tool. To scope the current study, a methodology will be created that could be applied to the entire Flying-V, however, is only fully developed for weight estimation of the outer-wing. Therefore, the main research objective of this thesis is:

> **"To estimate the structural weight distribution of the outer wing of a Flying-V aircraft by developing a fully parametric framework, which is compatible with the latest concept developments and allows for expansion into a full Flying-V aircraft."**

This framework could be applied to other unconventional aircraft as well, and evaluation of the performance and efficiency of the framework is essential. However, this study will focus on updating the structural representation of the Flying-V, according to the newest concept and parametrization, as to complete the overall Flying-V design tool. The requirements and basic set-up of the framework results from the objective and this Introduction. The fully parametric framework:

- should allow for accurate and sensitive weight distribution estimates.
- should allow for comparison of the different, non-conventional, concepts, including the No Leading Edge Spar concept.
- should include all design criteria required for accurate sizing of the structure.
- should allow for design of experiments of different structural layouts for the outer wing of the Flying-V.
- should have the potential to be part of a full design loop, by feeding back the converged design variables and the weight estimate.
- should make use of commercially available or open-source software only.

The framework consists of two major parts; the structure generation and the sizing methodology needed to give the weight estimate. Together the structure generation and the sizing methodology aim to provide a stiffness and weight model to enable feasibility and optimization studies in the areas of structural design, aeroelastic behaviour, and stability and control. The framework can be used in ParaPy for a full multidisciplinary design optimization. The novelty of the framework developed in this thesis, is the fully parametric definition that allows for design changes such that non-conventional concepts can be evaluated, in combination with a fully automatic FEA thickness optimization that allows for accurate results.

The structure generation and sizing tool developed in this research contributes to more sustainable commercial aviation by reducing the overall aircraft weight and providing an accurate weight estimate, early in the design phase. This allows for an accurate multidisciplinary trade-off, resulting in a more efficient design. The framework is developed to be used during the developments of the Flying-V, aiming to provide insights in the structural behaviour of the new aircraft concept, and giving structural weight estimates on different concepts variations to allow for a multidisciplinary trade-off. The framework aims to contribute to the development of the Flying-V aircraft, hopefully increasing the efficiency of the aviation industry towards a greener future.

1.8. Thesis Outline

In the following chapter, the methodology used to get the weight estimate, is explained. First, the structure generation will be explained. Then the finite element model generation will be elaborated upon. Starting with the shape generation, the mesh generation and the choice of finite element types used to resemble the geometry. Next, the material will be applied to the model, as well as the loads and the boundary conditions. To finish the chapter, the input file generation will be explained. After the methodology is explained, the design problem will be defined. First, the sizing variables and initial values of the problem are determined, followed by the failure criteria and the optimization settings used to define the design space. Once the design problem is defined, both the framework and problem definition will be verified. First, a modal analysis will show that the model is properly defined, and the model acts as one structure. This will be followed by a mesh convergence study, giving the quality of the mesh. An example problem is used to show that the framework yields the same results as verified, manual, methods. Lastly, an analytical verification is performed to verify the results of the use case in this study, the weight distribution of the outer wing. The results are presented next, followed by the final chapter that gives an overview of the conclusions and recommendations.

2

Methodology

In this chapter, the methodology, developed in this study, is explained. A concise process flow of the developed methodology is presented in Figure 2.1. To limit the number of software packages used, extensive use is made of the functionalities of Object-Oriented Programming (OOP) and Knowledge-Based Engineering (KBE), using the software ParaPy. Moreover, the choice for ParaPy allows for integration with the already existing Flying-V analysis tool in ParaPy. First, the parametric structure model is developed and generated in ParaPy, based upon the inputs and rules developed in the knowledge base. One of the inputs for the analysis is the numerical input model that describes the input geometry. The load cases that are to be considered in the analysis need to be provided, including the load factor and load distribution. Moreover, the weight breakdown of all the weight that is related to the model except from the structural weight, is also required as input. Lastly, the sizing criteria and constraints of the design space are needed as input. The structural model that is automatically developed from these inputs can be adjusted based upon user input through a GUI in ParaPy, if desired.

Now the structural model is generated, the structure should be sized in order to make a weight estimation. To size the structure model, use is made of a finite element analysis. Using finite element analysis allows for an accurate and sensitive weight estimate. All pre- and post-processing of the finite element analysis is done in ParaPy. Performing the pre- and post-processing all in the same software allows for a closed design loop, also automating the post-processing part and saves computational effort. ParaPy is combined with a finite element solver that includes optimization functionalities. In this study, NASTRAN is chosen to perform the finite element analysis. NASTRAN is chosen as it is the convention for FEA in the aerospace industry and houses a powerful optimization solution module called SOL200. A thickness optimization will be performed using SOL200. A thickness optimization is chosen as a full shape optimization is too computationally expensive and with the combination of the parametric layout and the thickness optimization, a computationally efficient framework is developed with design sensitivity results comparable to the results of a full shape optimization.

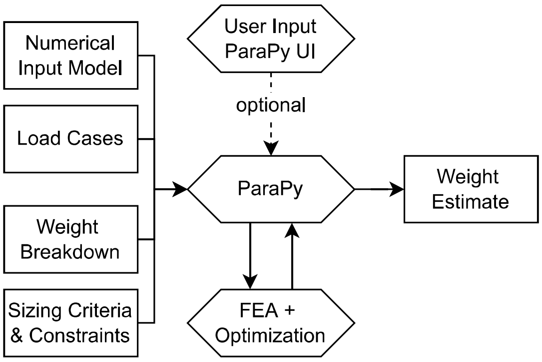

Figure 2.1: A concise process flow of the structural sizing method developed.

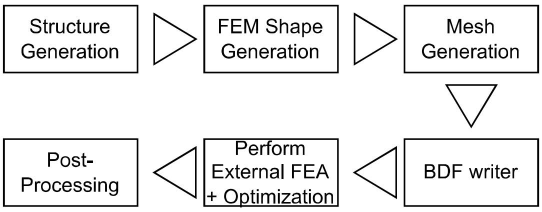

Figure 2.2: A detailed few of the process inside the ParaPy module of the methodology developed.

With the thickness optimization completed, the results from the finite element analysis and optimization are post-processed by a ParaPy module, giving information on the internal strains and stresses and optimized local thicknesses. Resulting in a weight estimate. In the following sections, all steps of the process flow will be elaborated upon. An overview of the steps is given in Figure 2.2. This chapter will show the methodology applied to the outer-wing of the Flying-V; however, it should be noted that the methodology is designed to be wider applicable to the entire Flying-V or other unconventional aircraft concepts.

2.1. Structure Generation

The first step in the method is to develop a structure model. The structure generation is fully automated in ParaPy using only the linear representation and the non-linear outer shell as input. Both these inputs are already available in the Flying-V ParaPy environment; thus, the structure can be automatically generated based upon default input values. The structure is generated as a 3D geometry, using only surfaces and lines. This provides a geometry model that can be automatically translated to a finite element model consisting of shell and beam elements only. The shell and beam elements are expected to be sufficiently detailed to represent the lightweight reinforced panel structure correctly and result in an accurate weight estimation based upon the critical failure modes.

ParaPy uses OpenCascade[1] for 3D modelling. Only the main structural elements are defined, and no detailed connections to the structural elements are modelled. The code, that generates the structure, is built from scratch as the tool developed by Van der Schaft [32] was difficult to translate to the current parametrization. Moreover, the shape generation, developed by Van der Schaft, was dependent on the leading-edge spar, which made it impossible to analyse the NLES concept. The new developed structure generation code aims to be more flexible whilst still being robust and allows for multiple layout concepts to be compared. This section explains the structure generation step by step. First, the general process is elaborated upon in the following paragraphs. This is followed by subsections explaining the structure generation classes in more detail.

As can be seen in Figure 2.3, the non-linear Flying-V can be divided in 5 sections: The symmetry or nose section, the constant cross-section fuselage section, the inner-wing section, the outer-wing section, and the winglet. These form different classes in the structure generation code. These classes differ slightly to specify the elements required and give the possibility to change input on parameters for each section. The following structure generation classes are developed: Rib Generation class, Spar Generation class, Stringer Generation class, Floor Generation class and Orthogrid Generation class. The Orthogrid class generates an orthogrid on a planar surface, useful for the spar webs and floor surfaces. The floor generation class contains a separate floor strut generation class. This study limits itself to the structure generation of the constant cross-section fuselage section, the inner-wing section, the outer-wing section, and the winglet. No structural layout for the symmetry or nose section is created. Likely, no new structural element classes are needed for the generation of the symmetry section, therefore, expansion of the model is expected to be straightforward.

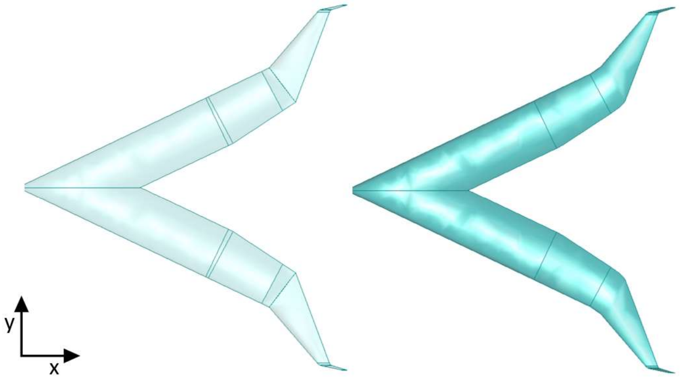

Figure 2.3: On the left the linear representation of the Flying-V as developed by Hillen [17]. On the right the non-linear representation of the Flying-V, constructed from the linear representation of Hillen, developed by Van Luijk.

---

[1] https://www.opencascade.com/open-cascade-technology/ [cited on 29-10-2022]

The main user input that is required for the structure generation and the corresponding default values are listed in Table 2.1. If no input parameters are given, the default parameters are used to generate a structure automatically. These input parameters can be easily changed in a GUI, and the structure will automatically update accordingly. Additional structure elements for local reinforcements can also be added easily. More advanced settings, to change the structure, can be changed in the code itself, however, the compiler must restart to implement these changes. The rib, spar and stringer generation classes are applied to all sections. The orthogrid generation class is used for all sections but the winglet, and the floor generation class is only used for the pressurized sections, so excluding the outer-wing and the winglet. The skin is generated directly from the shape of the outer shell, so no separate class is needed. The main principles of the structure generation will be explained by elaborating on the classes required for the generation of the structure of the outer-wing and the winglet. The activity diagrams of the structure generation can be found in Appendix section A.2. The section ends with a subsection on the ParaPy User Interface, showing the outer wing structure.

Parameter	Default Value $[m]$	Type
Rib/Frame pitch	1.0	float
Stringer pitch	0.2	float
Spar positions	$[0.15, 0.8]$	List of floats
Floor height	-0.5	float
Floor Strut Location	$[0.2, 0.5]$	List of floats
Orthogrid pitch	0.4	float

Table 2.1: Main input parameters for Layout Generation

2.1.1. Rib Generation

The ribs are generated first. An activity diagram showing the rib generation is shown in Appendix section A.2, Figure A.3. The rib generation is based on the leading edge and trailing edge. These edges are taken from the linear input model in order to prevent difficulties at the kinks in the model. In the linear model, both the inner- and outer-wing are split into two separate sections at the kink. The structure of both wing sections is developed in two steps, one section in front of the kink and one aft of the kink. The linear leading and trailing edge rail are a required input, as well as the rib pitch and the outer shell (either linear or non-linear). The rib pitch defines the distance between two rib faces. First, the number of ribs that are to be generated is computed. This is based on the maximum length of the leading or trailing edge. The length is divided by the desired rib pitch and the resulting number is converted to an integer and one rib is added. This is done to ensure the rib pitch is always smaller or equal to the desired rib pitch.

$$number\ of\ ribs = int\left(\frac{max(\,edge\ length\,)}{desired\ rib\ pitch}\right) + 1 \tag{2.1}$$

Once the number of ribs is defined, equidistant points are defined on both the leading and trailing edge. The leading-edge point is translated in the local Z-direction and a plane is generated from the three points. The planes define the location of the ribs. By defining the ribs based on planes, one allows easy implementation of user-input. Additional ribs can be defined based on planes, that are relatively straightforward to create in the GUI. The rib planes are intersected with the outer shell. After this, so-called, fuse operation, curves and faces can be extracted that define the ribs. The orientation of the ribs with respect to the leading edge is with this method not necessarily perpendicular, rather, by using the equidistant points, a gradual change in orientation is present if the leading and trailing edge are non-parallel. This prevents intersecting ribs or complex structures at the tip or root of the wing section, making it a fail-safe method for automatic structure generation. A minimum required number of ribs per section is 2, one at the root and one at the tip. This ensures a closed section, which is needed for the future fuse operations for the generation of spars. When defining the finite element model, duplicate ribs are removed.

Must a user wish to evaluate the ribs perpendicular to the leading- or trailing-edge, this can be easily changed by redefining the points that define the rib planes. However, this likely requires more manual checks and adjustments at the kink sections and transition from the outer wing to the winglet, to ensure the minimum desired rib pitch is maintained, and no intersecting ribs are generated. This will lead to a less robust structure generation, which is why it is avoided in this study.

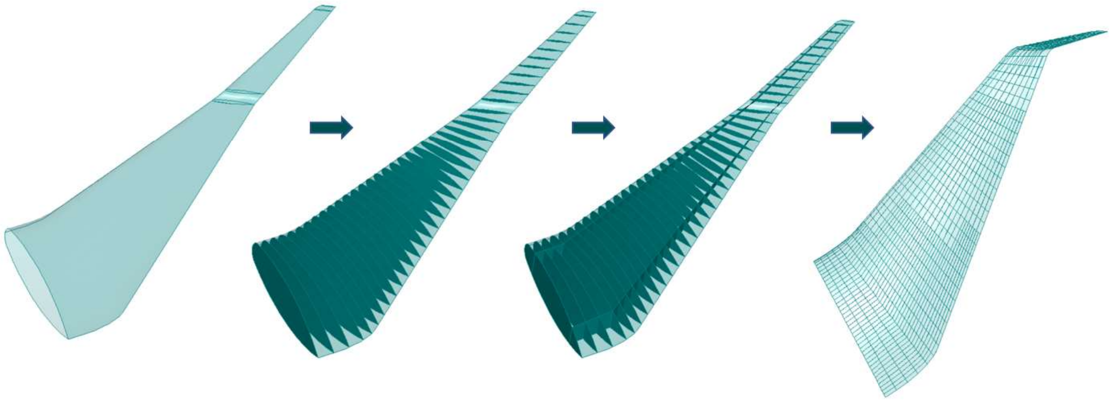

Figure 2.4: Image showing the structure generation of the outer wing and winglet from left to right. Starting with the empty outer shell, adding the ribs, and next adding the spars and lastly adding the stingers as well.

2.1.2. Spar Generation

After the ribs are generated, the spars will follow. An activity diagram showing the spar generation is shown in Appendix section A.2, Figure A.4. Spar generation is based on the spar location user input and the closed outer shell section. The closed outer shell section consists of the outer shell and the ribs defined at the root and tip of the outer shell. Notice that this requires the Ribs to be generated before the spars can be generated. If a user wishes to test a design without (conventional) ribs, it is possible to only use the ribs as construction elements and remove the ribs from the model later. The input of the spar locations is a list, and any number of spars can be defined. The location of the spar is defined as a percentage of chord line, where zero is defined at the leading edge, and 1 indicates the trailing edge.

The spar generation is similar to the rib generation. First, points are defined on the chord line of the root and tip of the section. The leading-edge point and trailing edge point of the chord line of the root and tip of the section are used as input for the interpolation, and two points are generated at the spar location. Again, an additional point is generated by translating the tip point in the local Z-direction. From these 3 points, planes are generated. The planes are intersected, or fused, with the shell and spar faces can be extracted. This allows for a spar definition per section, as a result the spars are ensured to be parallel to the leading and trailing edge, which prevents intersecting spars and difficult identification of kink locations, resulting in a fail-safe method for automatic structure generation.

The advantage of this method, is its simplicity and computational efficiency. Only one intersect operation is required and no complex sorting methods are needed. However, the downside of this method is that it only allows for the creating of planar structural elements. For the ribs and most of the spars, this does not pose a problem, as planar structural elements are preferred for these sections. For the spars connecting the outer-wing and the winglet, however, curved surfaces are required. For the real structure, and in the detailed design, this section will need more attention as a special connection spar is expected to be required. For the current analyses, curved spars surfaces that connect the planar spars in the outer wing with the planar spars in the winglet, are sufficient as these can provide a smooth transition and stress peaks can be avoided. The generation of these curved spars faces is more complex and will be explained next. The difference between the original spars and the corrected spars can be seen in Figure 2.5 and Figure 2.6.

A special Spar Correction class is created for the curved spar faces. The class requires the planar spar faces to be generated first, as the vertices of the connecting spar faces are used as an input to generate the curved connection spar. First, a shell is generated, defined by lines connecting the vertices of the neighbouring spar faces. This creates planar surfaces that have a definite size. The outer shell is intersected with the planar surfaces, similar to the normal spar generation method. Now, instead of directly extracting the surface that is generated by the intersection, the lines that are generated on the upper and lower surface are collected. Combining these lines with the tip and root edges of the neighbouring spars, a closed curve is formed. This closed curve is used to generate a filled surface, and the curved spar faces are created. The curved spar faces are guaranteed to be connected to the neighbouring spars faces.

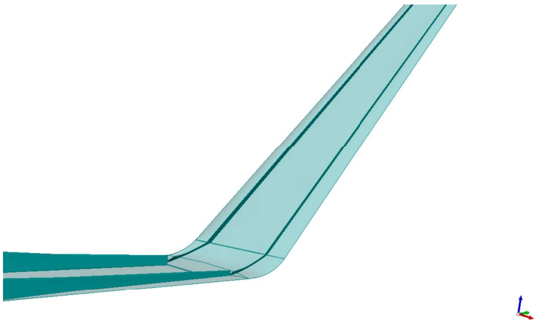

Figure 2.5: Spars as generated with the Spar Class. Zoom in on the spars connecting the wing and the winglet.

Figure 2.6: Spars as generated with the Spar Correction Class. Based on the spars, generated with the Spar Class. Zoom in on the spars connecting the wing and the winglet

2.1.3. Stringer Generation

Stringers are the most complex structural elements to define due to the double curved outer-shell surfaces, the taper, the non-symmetry for top and bottom surface, and the continuity of the stringers at the transition to different wing sections. Due to the tapered nature of the outer wing and the desire to continue the stringers all the way from the nose of the Flying-V to the tip of the winglet, a constant stringer pitch at every rib is not possible. The input value for stringer pitch is used as a minimum stringer pitch and the actual local stringer pitch will vary between the input value and 2 times this value, at maximum. The stringers are defined as lines, that later on get geometric properties assigned. The activity diagram of the Stringer Generation Class can be found in Appendix section A.2, Figure A.5.

The Stringer Generation class takes the end point of stringers from the previous section as an input. Assuming one is generating the structure for the entire aircraft, the stringer generation starts at the winglet and ends at the nose. The stringer generation for the winglet takes the stringer pitch input value and generates stringers start points on the edge of the tip rib. The stringers are generated for lower and upper surface separately to allow for additional design flexibility by enabling the user to define a different pitch on both surfaces. The rib edge is split by the spar faces to avoid stringers at the location of the spars. Next, all separate rib edge sections are evaluated one by one, and equispaced points are created on the edges. The number of stringer points is determined by dividing the edge length by the stringer pitch. An iterative loop now creates new equispaced points on all rib edges in the section, starting at the rib neighbouring the tip rib.

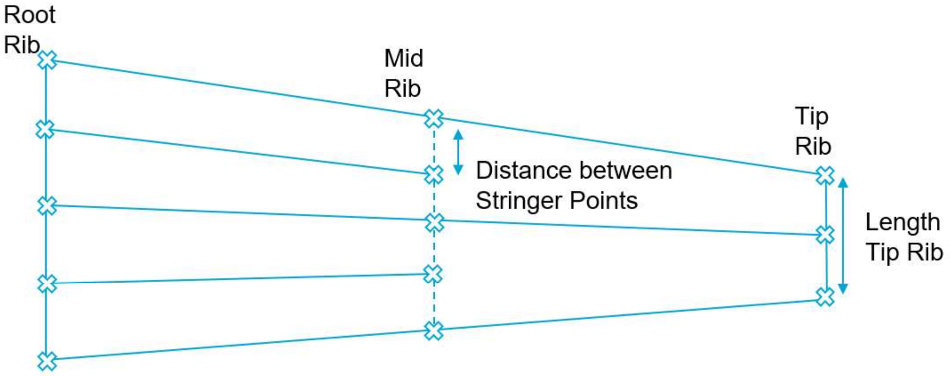

Figure 2.7: Diagram showing the basics of the stringer algorithm used for the stringer generation.

Initially, the number of equispaced points is kept equal to the number of points defined on the tip rib. This ensures continuity of the stringer. The distance between two neighbouring points is evaluated and as soon as the distance exceeds two times the desired stringer pitch, an additional point is added in-between the already existing point. The basics of the stringer generation are shown in Figure 2.7. Then the code moves on to a more inboard rib and determines this newly increased number of stringer points. Once all ribs of a section are evaluated, the points are grouped together. Using all resulting stringer points as control points, BSplineCurves are generated. The curves generated do not necessarily lie on the outer-shell, due to the double curved nature of the outer-shell, additional operations are required to ensure the lines are on the surface. The stringer curves are used to generate a shell with ExtrudedShells. These ExtrudedShells are intersected with the outer-shell and the edges resembling the stringer paths are selected. This splitting operation ensure the stringers lie on the outer shell, even for double curved sections, and prevent any future problems with mesh generation.

2.1.4. Graphical User Interface

The structure is automatically generated based upon default values unless a user did specify any properties and the desired values. However, once the structure is generated, one can view and edit this structure in a GUI if desired. No interaction is needed if all default values, or input values specified at the start do result in the desired results. The GUI provides an optional means to edit the structure before the FEM shape is generated. The basic input values can be changed, and the structure is automatically updated and refreshed taken the new input values into account. This allows for quick turnaround times and visual inspection of multiple structural layout concepts. A snapshot of the GUI can be found in Figure 2.8.

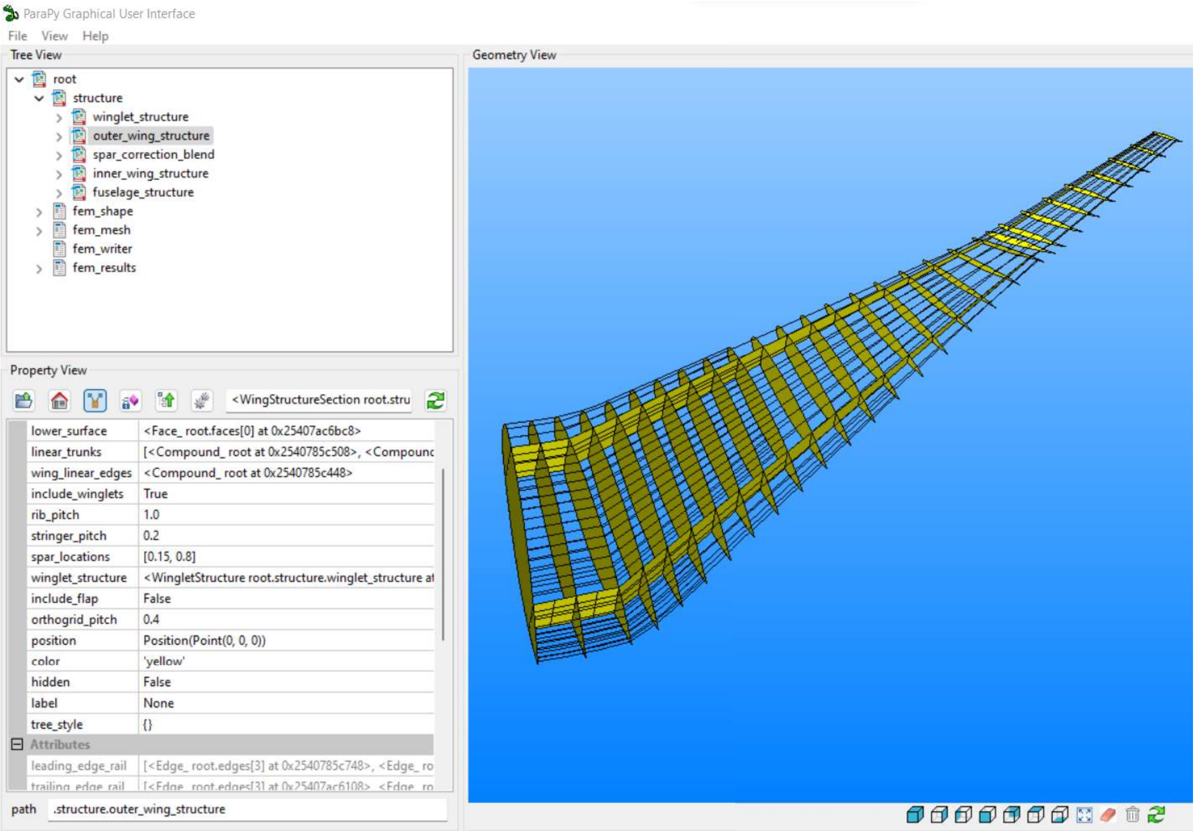

<WingStructureSection root.stru

lower_surface	<Face_ root.faces[0] at 0x25407ac6bc8>
linear_trunks	[<Compound_ root at 0x2540785c508>, <Compounc
wing_linear_edges	<Compound_ root at 0x2540785c448>
include_winglets	True
rib_pitch	1.0
stringer_pitch	0.2
spar_locations	[0.15, 0.8]
winglet_structure	<WingletStructure root.structure.winglet_structure at
include_flap	False
orthogrid_pitch	0.4
position	Position(Point(0, 0, 0))
color	'yellow'
hidden	False
label	None
tree_style	{}
Attributes	
leading_edge_rail	[<Edge_ root.edges[3] at 0x2540785c748>, <Edge_ ro
trailing_edge_rail	[<Edge_ root.edges[3] at 0x25407ac6108>, <Edge_ ro

path .structure.outer_wing_structure

Figure 2.8: Figure showing the Graphical User Interface with the outer wing structure and winglet structure loaded. The property view panel is opened to show the inputs for the outer wing structure.

2.2. Finite Element Model

This section explains how the structure model is converted into a finite element model. The entire development of the finite element model is automated in ParaPy. In this research, the finite element model developed for analysis with NASTRAN. However, all steps, up-to the writing of the NASTRAN input file, are equal for analysis with different FEA software packages.

2.2.1. Shape Generation

The first step in converting the geometry model to a Finite Element Model is the shape generation. Here, the edges and faces that are required to be in the FEA are selected and are assigned a Higher-Level Primitives (HPLs). The HPLs carry the information required for the FEA: initial dimensions, material, and element type. Once elements are collected, a General Fuse operation is performed to merge all element in to one shape. The element groups included are skin faces, rib curves, spar faces, spar curves, stringer curves, and orthogrid curves. The shape generation is an important step in the definition of the design problem. Only the individual elements added in the Fuse operation can be identified and meshed separately, allowing for a difference in model properties. If, for example, the ribs are added as one group, then all ribs have the same model properties. If a user wishes to give all ribs different model properties, one has to add the individual ribs to the Fuse operator instead of as a group. All individuals in the Fuse operation can later be identified by using the history function of ParaPy [4].

In this shape generation, final adjustments to the shape of the analysis can be made. One of the modifications that is demonstrated in this study is the addition or rather removal of the flap structure. When collecting all elements that will define the shape, some elements are split and some resulting surface from the split operation are excluded from the shape. In this way, the shape generated does not include the structure of the flap. In this study, the flap is defined as the structure aft of the trailing edge spar between the second and one but last rib of the most outboard wing section. The plane that defines the trailing edge spar is used to split the skin surfaces and only the skin surface in front of the trailing edge is collected for the shape Fuse operation, this is similar for the ribs. For the stringers, the rib planes are used to split the stringers and only consider the parts that are excluded from the flap area. It is important to note that because the history function of the shape is needed in the future, one cannot simply subtract the flap shape after the shape fuse operation. Therefore, this method is applied where the elements are split before the fuse operation is performed.

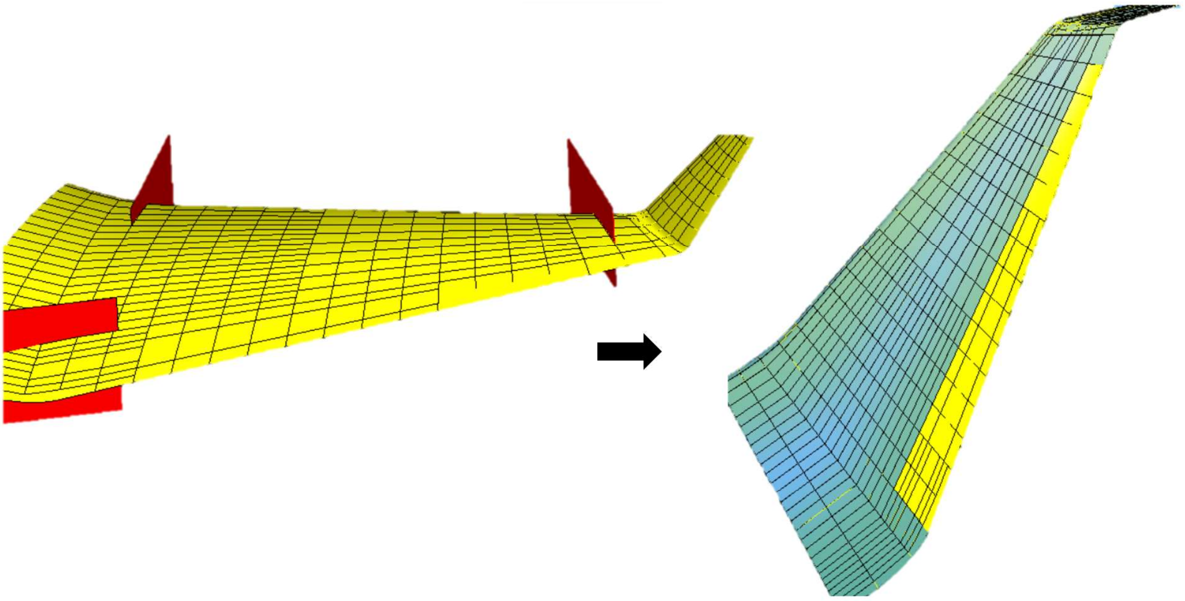

Figure 2.9: Image showing the shape modifications to the shape when removing the flap structure from the analysis. On the right, the full shape with flap is shown with the rib and spar planes used to split the elements such as to exclude the flap structure from the FEM shape. On the left the resulting flap shape is highlighted.

2.2.2. Mesh Generation

Once the shape is generated, the shape can be discretized, creating a mesh. In finite element analysis, the quality of the mesh is of great importance for the overall quality of the results. There are multiple high-level decisions that can influence the quality of the mesh. One of these important design decisions is to design a structured or an unstructured mesh. This decision goes hand in hand with the choice of element types that one uses for the structural mesh. The main advantage of unstructured meshes is that any type of element, and a mix of element types, can be used, which often enables more robust mesh generation. In unstructured meshes, there are no connectivity rules between elements. The main advantage of a structured mesh is that it is easier to perform uniform mesh refinement, to increase analysis accuracy. However, structured meshes can only be generated with quadrilateral or hexahedron elements, which makes it difficult to mesh complex or organically shaped parts.

So-called "mesh seeds" are often the first step in mesh generation, and the placement of the mesh seeds often control the mesh density. These mesh seeds indicate the positions of the nodes of the actual finite element mesh that will be generated and when the mesh is generated the nodes will be created at the location of the seeds. The correct identification of expected zones of stress concentrations and the according denser mesh seed placement is essential for a high-quality mesh.

One can decide to mesh one product with multiple meshes. Meshing two parts separately can enable parallel computing and makes it easier to debug and refine meshes of certain parts only. However, it is often difficult to combine the meshes again to be able to analyse the whole product at once. Mesh seeds can aid in combining two parts that are meshed separately. The mesh seeds can ensure that the two shared edges have the same number of nodes and nodes at the same location. Node equivalence can occur when combining the meshes. One should check and correct for node equivalence and eliminate the duplicate notes. Node equivalence should be checked for to generate an entirely enclosed and continuous mesh. Another common problem that could lead to unexpected and incorrect analysis results is element distortion. The aspect ratio and the internal angles of an element should be checked and within reasonable limit to still give reliable results.

ParaPy supports the use of SALOME [2], which is suited for grid generation for structural analysis and works well with the Open Cascade geometry. In this research, the mesh is generated by a Mesh Builder Class which inherits functionalities of SALOME. The desired mesh is close to a structured quadratic mesh. As mentioned before, a fully quadratic mesh is undesirable to prevent high skew angles and aspect ratios of the mesh elements due to tapered or organic faces. The Quadrangle parameter Standard is used as a 2D Mesh Hypothesis [30]. This hypothesis tries to mesh everything using all quadrangular elements. Standard allows for the use of both triangles and quadrangles in the transition area, on edges with a different number of elements. This prevents straddling elements. For the mesh control, a MaxLength function is used, where a maximum edge length can be specified which sets a 1D hypothesis on the edges of the shape. This 1D hypothesis places mesh seeds on all edges of the model. The grid spacing can be specified in the GUI, and a default spacing of $0.1\,[m]$ is used. Later, a Mesh Convergence Class is used to automatically give the lowest mesh spacing that still gives converged results based upon quick static analysis that gives an estimate on maximum deflection.

Robust mesh generation is needed to achieve automation. Extensive tests are performed on the robustness giving confidence in the resulting mesh. Node equivalence is checked in ParaPy, and duplicate mesh nodes are removed. The quality of the mesh elements is checked by NASTRAN to prevent analysis using highly distorted elements. The tolerances used by NASTRAN are shown in Table 2.2.

In order to set up the design problem correctly and assign different finite element types, the generation of mesh subgroups is required before mesh generation can be performed. All subgroups are meshed separately and receive a submesh. A Python Dictionary is used to assign finite element objects to subshapes. The history functionality of ParaPy is used to access the structural elements that were used as an input for shape generation [4]. This ensures that, for example, the mesh nodes on a spar face can later be accessed as a separate spar face mesh group. All separate design variables, require a separate submesh group. All receive a label, which enables referencing and automated property assignment. Moreover, the labels are used for post-processing.

Property	Tolerance CQUAD4	Tolerance CTRIA3
Min. Skew Angle [°]	30	10
Aspect ratio [−]	0.5	N/A
Interior Angle [°]	150	160
Warp Factor[−]	0.5	N/A

Table 2.2: Element Geometry Test Tolerances used by NASTRAN at the start of an analysis during a Geometry Test.

2.2.3. Finite Element Types

The HPLs assigned to all faces and edges in the shape, contain an element type. There are many types of elements that can be used in finite element analysis, and a trade-off between modelling accuracy and computational costs is required. 3D elements are the most versatile elements and can be used to model all types of structure, however, the elements have a high number of Degrees Of Freedom (DOFs) which results in high computational costs. As a rule of thumb, commonly, 2D elements are used for parts that resemble a plate- or shell-like geometry, and 1D elements are used for parts that resemble a bar- or arch-like geometry [20]. 3D elements are normally only used for bulky parts where 1D or 2D elements are insufficient.

The finite element types used in the current analyse are 2D shell elements, 1D beam elements and Rigid Body elements. The precise finite element types are closely related to the mesh shaped. Most of the elements used are CQUAD4, for modelling of the quadratic mesh faces. Some CTRIA3 elements are required to prevent to model the triangular mesh faces. The CQUAD4 and CTRIA3 elements are used for the skin and spar webs.

---

[2] https://www.salome-platform.org/ [cited on 29-10-2022]

CBEAM elements are used for spar flanges, stringers, and the stiffeners of the orthogrid structure. RBE2 elements are used for the modelling of the ribs, as it was chosen to not include the sizing of the ribs in the current analysis.

The Rigid Body element, RBE2, is used to impose stiffness to the structure. The RBE2 has one independent node that connects to multiple dependent nodes. The RBE2 elements can divide a load applied to the independent nod, equally over all dependent nodes, making it a suited element for load introduction into the structure. One must specify the DOFs that the RBE2 should provide stiffness for, commonly either only the translational stiffness in x,y and z direction is chosen or both translational and rotational stiffness is desired and all 6 DOFs are constraint.

2.2.4. Material

The HPLs not only contain the element type, the HPLs also contain the material properties of the elements. The material choice influences the structural efficiency, and a higher efficiency can be achieved with the use of the right material. Advanced composite structures have been developed within the aircraft industry over the past decades [6]. Advanced composites promise significant weight savings relative to metal structures, especially for parts that clearly experience a main load direction. Weight saved on aircraft structure immediately allows for an increase in payload weight for a given MTOW. Material density and high specific strength properties are required in aircraft materials. Strength is an important material property for aircraft structures; however, a high elastic modulus and fatigue resistance are also required. The high elastic modulus prevents buckling and with increased fatigue strength the lifetime of the aircraft can possibly also be increased.

In the first aircraft, the structure was made from wood. Soon, aluminium started to replace wood. Now, titanium and high strength steels are also used more often. Aluminium lithium is promised to outperform conventional aluminium in the future. Composite materials and carbon fibre reinforced plastics have also led to great improvements in structural efficiency over the past years. Not only strength efficiency and fatigue resistance are required for a material to be suited for aircraft structures. Fracture toughness, crack growth, corrosion resistance and environmental stability are required [6]. Moreover, a material that has a too high density will not be ideal for aircraft structures as the lower bound on the material thickness, due to manufacturing issues and stability problems, will often be higher than the thickness required for pure strength. The most feared failure mode is fatigue. This is because damage caused by fatigue is difficult to detect however, it can weaken the strength of critical components. Fatigue resistance has become more and more the driven factor for material choice since more high strength materials have become available.

This research will only consider one material in the entire analysis. A 2024-T351 aluminium alloy is chosen. The material properties of this alloy are found in Table 2.3. This is a relatively easy material to model due to its isotropic and elastic behaviour, compared to composites, and still a material often chosen in aircraft design. During the research, one should keep in mind that higher structural efficiencies are possible by orientating composite materials perfectly according to the expected loads. Unidirectional CFRP can achieve much higher specific properties in this way, compared to metallic allows. With this increase in structural efficiency, substantial weight savings can be achieved compared to metallic structures. In previous research on the oval fuselage, it was found that a weight saving of around 19% can be reached when using composites instead of aluminium [29]. What must be noted, is that with CFRP composites, impact strength and toughness become more important due to the specific material properties of CFRP. And although, CFRP composites promise an increase of around 30% in specific buckling strength, inspection of failure due to fatigue or impact becomes increasingly difficult [27].

Property	Value
Young's Modulus E(MPa)	73.1E + 3
Material density $\rho\left(\mathrm{Kg/m^3}\right)$	2.78E + 3
Yield stress σ_{Yield} (MPa)	324
Ultimate stress $\sigma_{\mathrm{Ultimcte}}$ (MPa)	469

Table 2.3: Material properties of AL 2024-T351

2.2.5. Loads

Once the elements are defined, loads can be applied to the model. Previously, use was made of Airbus in-house software to define the loads and trim the aircraft [7]. Claeys used gust loading as the manoeuvring load used for the load distribution. The design of aircraft structures is often sized by the ultimate load factor. Loading diagrams will indicate the load factor which an aircraft is expected to experience. For the outer-wing of the Flying-V, it is expected that the critical ultimate load case is caused by a gust while flying at cruise speed. In gust loading, a normal lift distribution is applied, which means a close to elliptical lift distribution for the entire aircraft. However, Claeys did apply the manoeuvring load factors to the lift, resulting in a 2.5g and -1g scaling of the gust load. This is expected to be over designed, as it is unlikely that gust loads with these load factor does occur. Also, these trimmed loads are unavailable for the current research, and thus, a new load distribution needs to be defined.

Conventionally, gust loadings are well within the limits of the manoeuvre load factors. And the manoeuvre load will size the aircraft wing structure. For the Flying-V this is expected to be different due to load alleviation. The manoeuvre loads, the 2.5g and -1g loads, are not expected to be critical due to this manoeuvre load alleviation. As the outer wing will act like a horizontal tail plane, to trim the aircraft. The Flying-V does not utilize High-Lift Devices, and Lift is increased by increasing the lift generated by the main body. During the manoeuvre, the angle of attack will increase, the resultant lift will move forward, and the outer wing will have to generate a down force to balance the aircraft. The exact load distribution during manoeuvres is not quantified at this stage in the design, and the gust loads are expected to result in a higher aerodynamic load on the outer wing.

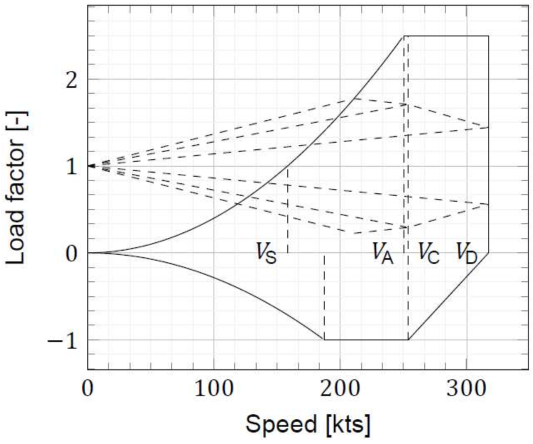

Figure 2.10: Loading Diagram of a Conventional Aircraft. Created by Nieuwenhuizen [24].

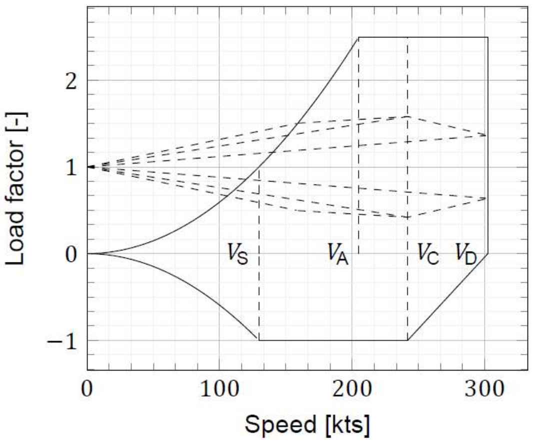

Figure 2.11: Loading Diagram of a Flying-V. Created by Nieuwenhuizen [24]

Although the wings of the Flying-V are much larger, the gust loads are smaller compared to conventional aircraft. This can be seen in the loading diagrams in Figure 2.10 and Figure 2.11. And can be explained by the lower lift slope. A lower lift slope indicates that there is a weaker link between change in angle of attack and lift. As a gust can be compared to an unexpected change in angle of attack, a lower lift slope would indicate a less severe change in lift, lower the gust load factor. However, it must be noted, that the assumption is made that there is no delay between the time when a gust hits the nose of the aircraft and when it reaches the outer wings. This assumption holds for a conventional aircraft, as a conventional aircraft will experience little delay since the wings are nearly perpendicular to the flow. For the Flying-V however, this is not the case, and a significant delay could be experienced. For now, it is assumed that these load factors for the gust loads are valid and a load factor of 1.8 for a gust load distribution is chosen. For the analysis, two load cases are chosen: load case 1 with a load factor of 1 and load case 2 with a load factor of 1.8.

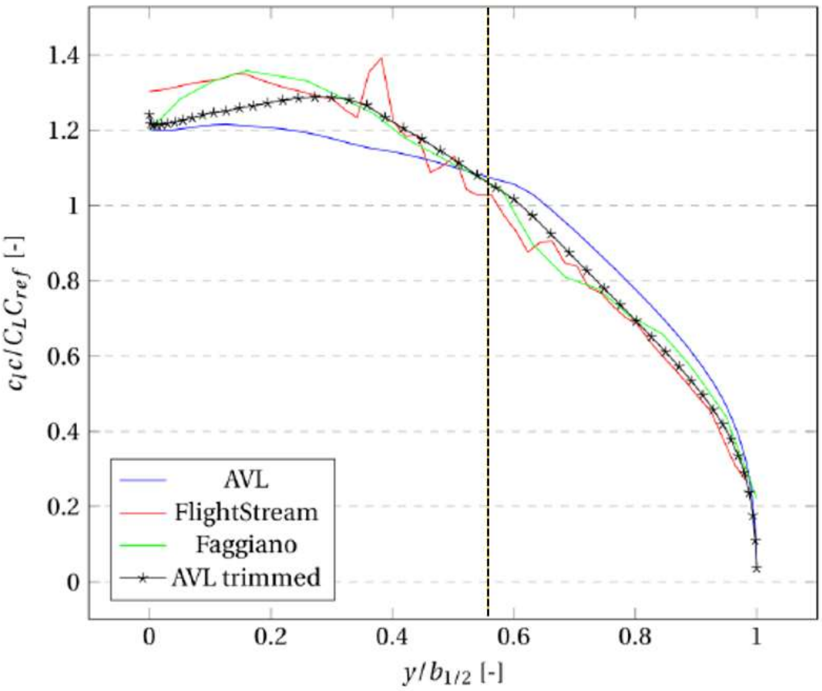

Figure 2.12: Spanwise lift distribution at the design lift coefficient. The black dashed line indicating the spanwise location that marks the transition from inner-wing to outer-wing. Created by Oosterom [25].

It is assumed that the outer wing does not hold any fuel and the only forces considered in this thesis are aerodynamic forces. The drag loads are neglected, as the drag loads are estimated to be less than 5% of the lift load. With the L/D ratio assumed to be 24.3 in line with the ratios calculated by previous Flying-V research [12] [25]. The load acting on the outer wing is thus assumed to only consist of the lift forces. For a load factor of 1, the lift is set equal to the MTOW. This is an overestimation, as the MTOW is greater than the weight during cruise, making for a conservative estimation. The lift distribution of the Flying-V is approximated by Oosterom [25], comparing multiple lift distributions resulting from previous research by Faggiano [14] and several different analysis methods. The lift distribution shows the spanwise lift at the design lift coefficient when the aircraft is trimmed. Integrating the lift for the outer-wing, shows that approximately one third of the total lift is generated by the outer-wing. For one single outer-wing the lift is calculated with Equation 2.2 and Equation 2.3.

$$L_{total} \approx MTOW \cdot g = 280 \cdot 10^3 \cdot 9.81 \approx 2,750 \cdot 10^3 [N] \tag{2.2}$$

$$L_{one\,outer wing} \approx L_{total} \cdot \frac{1}{3} \cdot \frac{1}{2} \approx 460 \cdot 10^3 [N] \tag{2.3}$$

2.2.6. Boundary Conditions

One of the final steps in pre-processing is the application of boundary conditions. As only a part of the structure of the Flying-V is analysed, boundary conditions are required to constrain the model. The boundary conditions are applied to the rigid body element at the root, resembling the most inboard rib. A single-point constraint is applied to the independent centre node of the RBE2, and movement is constraint in all but one degree of freedom. This is needed to prevent an overdetermined system. However, to prevent movement in all direction, a fictitious support is applied in the remaining degree of freedom. Here, it is chosen to apply the fictitious support in the global z-direction. NASTRAN SPC1 and SUPORT1 cards are used to specify these boundary conditions.

2.2.7. BDF File Generation

As a last step, the NASTRAN input file must be generated. A NASTRAN input file is of file type, .bdf, and makes use of the FORTRAN coding language [22]. An input file consists, globally, of 3 separate sections: An Executive Control Section, a Case Control Section, and a Bulk Section. The generation of the NASTRAN input file requires in-depth knowledge of the NASTRAN statements used. All NASTRAN statements make use of a NASTRAN card. A special ParaPy NASTRAN Library is utilized such that all NASTRAN cards can be written to the input file automatically. A template is required, as a start of the input file, that contains the Executive Control Section and the Case Control Section. The template mainly specifies the solution type to be used and the subcase parameters and are rather compact files. The templates are independent of the geometry, however, are dependent on the analysis type. The templates for this research are stored in a folder, and the correct template is picked based upon the desired analysis type as specified by the user. If no analysis type is specified, the default, the SOL200 analysis, is picked. Three types of analysis are considered in this research:

- SOL101: Linear Static Analysis
- SOL105: Linear Global Buckling Analysis
- SOL200: Optimization Analysis

Starting with the template, only the Bulk Section must be defined. The Bulk Section contains all the information on the geometry and the mesh: the grid node coordinates and IDs, the element types used to model mesh faces and the corresponding grid nodes, the boundary conditions, and the loads. For a SOL200 analysis also, the design problem needs to be defined in the Bulk section. This means the Bulk section also contains the information on the link between the geometry and the design variables, the bounds of the design variables, the constraints, the objective, and the optimization settings.

Using the BDF Generation class developed in this research together with the corresponding template files, NASTRAN input files can automatically be written that carry all information required to perform a NASTRAN analysis. A class loops over the submeshes and the corresponding HLP. From the HLP the element type can be extracted as well as the remaining information required to generate the NASTRAN cards that are linked to this submesh.

To keep track of the grid IDs of NASTRAN and the mesh IDs of ParaPy, use is made of a Python Dictionary storing the grid IDs and the corresponding mesh IDs. This is needed to assign the right grid points to the elements and element groups. Later, with post-processing, this dictionary is needed. A BDF Generation class loops through the different mesh subgroups and checks the HLP type of the mesh group. The corresponding NASTRAN statements are selected and generated per mesh group. The statements are collected in a list. This list of NASTRAN statements is used by the Writer function of the ParaPy NASTRAN library, that writes the actual .bdf file. ParaPy enabled dynamic allocation of the IDs and EIDs, prevents duplicate IDs could be created, and ensures correct referencing of the IDs is performed.

3

Design Problem Definition

In this chapter, the objective of the structural design problem is formalized and the optimization problem that NASTRAN utilizes for thickness sizing is determined. The objective of the structural sizing is to minimize weight whilst providing a structure that can endure the design load for the entire design lifetime of the aircraft. Ideally, the structure is designed in such a way that if a critical load is increased beyond the design load, this leads to multiple failure modes becoming critical. This would mean that for all failure modes the parts are designed to be just sufficient, indicating an efficient design.

NASTRAN SOL200 analysis performs a gradient-based sizing optimization base on a single-objective optimization problem [22]. This single-objective optimization problem is defined by the design variables, the bounds on the design variables and the design criteria. The objective in Equation 3.1 that represent the goal of the optimization, the inequality constraints in Equation 3.2 that represent the bounds to the design space, the equality constraints in Equation 3.3 that need to be satisfied in order to achieve a feasible design, the side constraints in Equation 3.4 on the design variables to limit the search area, and the design variables in Equation 3.5 that can be changed to explore the design space.

NASTRAN SOL200 uses a gradient-based algorithm to find the optimum. In gradient-based algorithms, the gradients of the objective function and constraints are calculated, which is used as input to determine the search direction. A modified feasible direction algorithm is used, to determine the direction of search. The direction of search is continued as long as the objective is further minimized. Once there are no improvements in the objective, the problem is said to be converged and the solution is terminated. Kuhn-Tucker conditions are used to determine if an optimum is found. The first-forward finite difference approximation is used to get the gradients of the design variables. For a gradient-based optimizer, it is desired to start from a feasible design. Starting from an infeasible design makes it difficult to find a search direction that takes the optimizer to a feasible design. Understanding this is key when using the framework developed. The gradient-based single objective optimization allows for efficient evaluation of over thousands of design variables, making the method suited for the current application. However, the efficiency and the total computation costs of the optimization usually rise with an increase in design variables.

$$F(\mathbf{x}) \tag{3.1}$$

$$g_j(\mathbf{x}) \leq 0 \qquad j = 1, ..., n_g \tag{3.2}$$

$$h_k(\mathbf{x}) = 0 \qquad k = 1, ..., n_h \tag{3.3}$$

$$x_i^l \leq x_i \leq x_i^u \qquad i = 1, ..., n \tag{3.4}$$

$$\mathbf{x} = x_1, x_2, ..., x_n \tag{3.5}$$

In this chapter, first, the sizing variables and the corresponding initial values and bounds are discussed. Followed by a section on the failure criteria used to drive the optimization problem. At the end of the chapter, the optimization settings used in this research are indicated.

3.1. Sizing Variables & Initial Values

The sizing variables combined with the sizing constraints determine the design space of the optimization problem. The motivation for choosing the sizing variables is based upon a trade-off between computation effort, manufacturability and expected weight saving potential. NASTRAN utilizes the finite difference method for sensitivity analyses and polynomials as the shape function, with the design variables as the coefficients of the polynomials [22]. In this research, the choice is made to use all independent design variables and no use of reduced basis functions is made. However, implementation of reduced basis functions is straight forward, within this framework, and could be beneficial to implement if the number of design variables is increased. All structural elements and the corresponding, independent, sizing variables, used in this research, will be explained next.

As mentioned before, the ribs will not be sized in this optimization problem. This is a common choice in wing finite element analysis, as the rib thickness is normally determined based upon criteria that are not (fully) captured in the analysis. The rib thickness is assumed constant and equal to the average of the skin thickness, in order to give a total weight estimate.

The skin is split in an upper and lower surface and in different sections by the ribs. Thus, for all skin panels between ribs two design variables are assigned, one for the upper skin panel and one for the lower skin panel. The design variable refers to the thickness of the skin. The spar web is also split in different section by the ribs, and all spar sections get one independent sizing variables, indicating the thickness. Important to note, is that with this method, the rib spacing automatically defines the number of design variables as well. Initially, the rib spacing is set to 1.0 [m], in line with industry standard for preliminary structural analysis.

All stringers are assigned one sizing variable. All stringers have the same static shape. For the baseline design, all stringers are L-shaped. Initially, the stringers are sized with guidelines used commonly in the industry [6]. The initial thickness of the L-shaped stringer is equal to the initial skin thickness and the size of the flange is approximately one third of the stringer pitch, in line with the suggestions of Howe. The ratio between the thickness and size of the flange is constant and equal to 10, and both flanges are equal. This holds for the spar flanges as well.

Sizing Variable [m]	Initial Value	Lower Bound	Upper Bound
Skin Thickness	0.008	0.0012	0.025
Spar-web Thickness	0.008	0.0012	0.025
Stringer Flange			
Thickness	0.008	0.0012	0.016
Size	0.08	0.012	0.16

Table 3.1: Sizing Variables

The initial thickness of the skin, spar-web and stringers is chosen to be equal. This allows for a smooth initial stress distribution. The initial thickness is chosen such that the resulting design is feasible. Next to an initial value, all design variables are also assigned a lower and upper bound. Both bounds are based upon expected manufacturing limits and reasonable ranges based upon actual thicknesses used within reference aircraft. An overview of the design variables and their corresponding bounds is given in Table 3.1. Rivet spacing is beyond the scope of this project and will not be designed for.

3.2. Failure Criteria

The failure criteria are translated to design constraint that will drive the optimization. Previous research on the key design drivers of conventional aircraft wings has shown the importance of inclusion of failure criteria on strength, buckling and fatigue [35]. This research by You et al. tries to identify the key design inputs for a FEM-based structural sizing of a conventional aircraft wing [35]. The critical loads and failure criteria that drive the structural design of the wing are identified through a sensitivity analysis. The results of the study clearly show that in addition to a yield strength constraint, buckling and fatigue analyses drive the design. Buckling and fatigue constraints account for a stiffness increase of 32-57% and 10-15%, respectively. Moreover, the aircraft rolling loads did also increase the stiffness by 10-17%. Accounting for the buckling criteria, fatigue criteria and rolling loads increased the mass of the sized wing with 7-24%. The engine loads and landing and ground handling loads are considered to be not critical as their influence on mass estimation is within 5%. This study thus clearly shows the importance of the implementation of buckling and fatigue analysis during the mass and stiffness model sizing, of aircraft wing design. Therefore, static yield strength, buckling and fatigue will be considered in this research. No maximum deflection limit is set, as it is expected that the deflection is not going to be critical for operations or performance.

3.2.1. Static yield strength

Strength is the ability of a material to sustain a load without excessive deformation or failure [16]. Strength is a material property which is experimentally determined. A stress-strain diagram is generated from a tension or compression test, and from this diagram the material behaviour under various loading scenarios can be estimated. For most metals, the stress-strain diagram looks somewhat comparable. Upon relatively light loading, the material shows linear elastic behaviour where the stress is proportional to the strain. Yielding starts after the elastic limit is reached. At the elastic limit, the specimen will still be able to go back to its original shape after unloading. However, a slight increase above the elastic limit and the material will yield. Yielding damages the material and permanent, plastic, deformation occurs. This means yielding can be seen as a form of material failure occurring in metals. After yielding, the ultimate stress can be reached due to a phenomenon called strain hardening. Finally, necking eventually will cause the material to fracture.

Materials can be divided into two main categories based upon the stress-strain diagram: ductile or brittle. A ductile material can handle large strains before it fractures. A ductile material is often preferred by engineers, as ductile materials first experience large deformations whilst absorbing energy before the material fails. Whereas brittle materials tend to fail almost immediately after the yield stress is reached, which causes a more unexpected failure. In structural design, for simplification, a metal is often considered to have failed after the yield stress is reached. The Von Mises stress is often used as a criterion for the material failure, as the Von Mises stress averages the stress in all three-dimensions to achieve a one-dimensional stress value. The Von Mises stress is mathematically defined in Equation 3.6. In this research, once the material reaches the Von Mises stress, the material is considered to have failed. Therefore, for a feasible design, all Von Mises stresses in the structure must be below the yield strength. To account for any modelling inaccuracies and imperfections, a safety factor of 1.5 is applied to the yield stress allowed.

$$\sigma_{VonMises} = \frac{1}{\sqrt{2}}\sqrt{(\sigma_{11}-\sigma_{22})^2+(\sigma_{22}-\sigma_{33})^2+(\sigma_{33}-\sigma_{11})^2+6(\sigma_{12}^2+\sigma_{23}^2+\sigma_{31}^2)} \tag{3.6}$$

3.2.2. Structural Instabilities & Buckling

Strength failure is often caused by tension forces. Compressive forces, often lead to instabilities before maximum material strength is achieved. For long and slender parts, compressive loading may cause the part to deflect laterally or sideways, these material instabilities or also known as buckling. Buckling can lead to sudden failure of a structure and is important to consider. One can specify two general forms of buckling: local buckling and global buckling. Global buckling is the instability in a long, slender column. Local instabilities are also referred to as crippling and is related to shorter elements.

When loaded in compression, a part is unlikely to be able to support a stress close to the yield stress before failure, and a critical load value is needed. The critical load P_{cr} is the maximum load that a column can support, before buckling occurs. The column will buckle about the principal axis of the cross-section having the least moment of inertia if the member is supported the same way in every axis [16].

For pin-supported long slender columns, a buckling equation can be written, as seen in Equation 3.7.

$$P_{cr} = \frac{\pi^2 EI}{L^2} \tag{3.7}$$

Here E is the modulus of elasticity for the material, I is the smallest moment of inertia for the column's cross-sectional area, L is the unsupported length of the column, whose ends are pinned, and P_{cr} is the critical load for column buckling.

For more complex structures, Equation 3.8 can be used, for linear buckling analysis [11]. In this equation, the structure's elastic stiffness matrix and global geometric matrix are used to determine if buckling does occur under maximum loading. Here, λ is vector of eigenvalues, u is an eigenvector which satisfied the equation and $\mathbf{K}_0$ is the elastic stiffness matrix and $\mathbf{K}_G$ is the global geometric matrix.

$$(\mathbf{K}_0 - \lambda \mathbf{K}_G)\,\mathrm{u} = \mathbf{0} \tag{3.8}$$

Buckling will drive the design and will determine the amount of support that is needed, often in the form of stringers, to prevent failure due to instabilities. Generally, buckling is a critical failure mode in design, and much weight is added to the structure in order to prevent buckling. In the design, one should aim for a stringer size and spacing which allows a column stress equal to the crippling stress, as this gives the least number of supports at the highest stress [6].

The linear buckling analysis of NASTRAN is applied to evaluate global structural instabilities within the model. During this analysis, the eigenvalues of the entire structural stiffness matrix is evaluated. As a result, global buckling is assessed. The first 20 buckling modes are analysed and again a safety factor of 1.5 is applied. Twenty buckling modes are evaluated during buckling analysis to achieve convergence of the analysis. Due to excessive computation costs of non-linear buckling analysis, only linear buckling analysis is performed. A limitation of linear buckling analysis is the overestimation of the performance of the structure against buckling, due to instabilities to take geometric nonlinearity into account. The additional internal stresses that occur due to deformation of the structure are not considered in the linear buckling analysis. Excessive buckling due to additional compressive forces in the top skin, caused by the upward bending of the wing, are, for example, not considered.

3.2.3. Fatigue

The strength and buckling failure modes discussed before are related to a one time only static loading. However, loading may also be applied repeatedly or cyclic. For such cyclic loading, the material strength may be lower than the expected strength based upon the yield strength, and failure occurs at a stress below the yield stress. The premature failure is caused by microscopic imperfections, within the material or part, which result in extremely high localized stresses which exceed the average stress acting on the structure. Miniature cracks appear at these highly stressed locations, and upon cyclic loading, these cracks grow continuously. The crack growth reduces the effective cross-section area and at some point, the material can no longer sustain the load and failure occurs.

In order to prevent fatigue failure, a new failure criterion must be determined. The fatigue limit of a material is found experimentally and is a limit below which no failure can be detected after applying load for a certain number of cycles [16]. The fatigue limit can be determined from an S-N diagram, or stress-cycle diagram. It is assumed that for any stress below the fatigue limit, the fatigue life is infinite, and failure due to fatigue is not considered any more. Moreover, in an S-N diagram it is assumed that the loading is of constant amplitude, and the mean stress is zero. If the mean stress is non-zero, a special S-N curve should be used as this influences the fatigue life as well. For the outer wing of the Flying-V, the cyclic loading can refer to the loading and unloading of the outer wing, comparing the loading when the aircraft is stationary to the loading when the aircraft is in cruise flight.

Important in structural design, to be able to design for fatigue, one must estimate the number of load cycles a design must endure before failure is allowed. For an aircraft, this can be the number of flights an aircraft is designed for. During design of an aircraft, a Design Service Goal, DSG, is set. In this DSG the number of flights is determined. The number of flights required for the Flying-V is 40,000 flights.

$$S_{allow} = \frac{f_{exceeds} * 10^{-\frac{A}{B}} + D}{\left(K_t^E * \frac{2-2S_m}{1+Scale}\right)}^{C} \qquad Scale = \frac{S_{a_{flight}}}{S_{m_{flight}}} \tag{3.9}$$

High-fidelity fatigue analysis is complex and computationally expensive. However, fatigue is proven too often be a critical failure mode in structural sizing [35]. Therefore, a rather simplistic first order estimate for fatigue will be used in this framework. A general model for stress-life fatigue prediction [1] is used in combination with a standardized load spectrum developed by NLR [10]. The model for fatigue life prediction incorporates the effects of both stress ratio and stress concentration factor. Crack initiation and crack propagation are the two most important measures in fatigue analysis, and both are included in the fatigue life prediction model with the extensive use of notched specimens. This allows for fatigue prediction without the need for a detailed design of the structure. By rewriting the equation for the general fatigue life model to the maximum allowed stress for a number of cycles to failure, the fatigue analysis can be easily included in the framework. With Equation 3.9, the maximum allowed Von Mises stress in the structure can be determined. The maximum Von Mises stress allowed is equal to the S_{allow} with a safety factor of 1.5 applied. For fatigue analysis, a load factor of 1 is used. In this study N, the minimum number of cycles before fatigue failure may occur, is assumed to be 40,000.

	Definition	Value
A	Microstructure	12.81011
B	Processing	3.35997
C	Load Spectrum	0.67782
D	Geometry	158.9626
E	Environment	0.75416

Table 3.2: Fatigue-life prediction model parameters. Used for the model developed by Al-Rubaie [1]

Exceedance Frequency	Scale
10^1	1.6
10^2	1.215
10^3	0.916
10^4	0.628
10^5	0.419
10^6	0.247

Table 3.3: Standardized load spectrum developed by NLR indicating the expected exceedance frequency per 40,000 flights [10].

Equation 3.9 can be applied with relatively little knowledge of the design. The parameters used, and the definitions, can be found in Table 3.2. The stress concentration factor K_t is estimated to be 4.5, in line with the practical design factor indicated by Niu [6]. This stress concentration factor is quite conservative, and in later stages of the design, when the geometric details and manufacturing techniques are known, it is expected that the stress concentration factor can be lowered. The stress concentration factor can be more accurately determined analytically using the theory of elasticity, or computationally using FEA, or experimentally using photoelasticity or strain gauges with material and shape samples [26].

The exceedance frequency, $f_{exceeds}$ for 40,000 flights, can be found in Table 3.3. When defining the optimization problem, the critical S_{allow} is determined from all the exceedance frequencies, and a constraint on the fatigue load case is generated. The Scale is defined as, the $S_{a_{flight}}$, the stress value of the anomaly that occurs a certain number of times according to the exceedance frequency and the number of flights. Divided by the mean stress value of stress in flight $S_{m_{flight}}$. This $S_{m_{flight}}$ value is the Von Mises stress resulting from the FEA.

However, in this application, the scale value is based upon the statistical data from NLR to determine the scale factor based on an estimated $S_{a_{flight}}$.

3.3. Optimization Settings

With the DOPTPRM parameter of NASTRAN the settings for the optimization can be specified. With FSDMax the number of Fully stressed Design Cycles that are to be performed at the start of the optimization, can be specified. With DESMAX the maximum number of design cycles can be determined, excluding the number of FSD cycles. In this research, the default value used, will be a maximum 3 FSD cycles to start and a maximum of 50 successive design cycles.

In order to achieve convergence, additional settings, specific to this research, are required. An absolute criterion for convergence is implemented. The problem is considered converged if the absolute change in objective between two optimization cycles is less than 25 [kg], and the optimization is terminated once this is reached. The maximum fractional change allowed in each property during an optimization cycle is also set in order to prevent skipping over an optimum. The maximum fractional change allowed in each property, CONV2, is set to 0.05. DELX is the fractional change allowed in each design variable during any optimization cycle. This is closely related to the CONV2 value and is set at 0.125. The minimum move limit for the objective, DPMIN, is set to 0.0025. This is closely related to the minimum design variable move limit, DXMIN, which is set to 0.0125.

After termination, a statement on the optimization is formulated indicating the state of convergence. Three options are possible: hard convergence, soft convergence, or the maximum number of design cycles. The maximum number of design cycles indicates that no convergence could be achieved, and the result is the best compromise design. Often this refers to an infeasible design. The optimization was terminated as the maximum number of design cycles was reached. If convergence is achieved, the run terminates prior to the maximum number of design cycles. NASTRAN performs a convergence check every design cycle, directly after the structural analysis. Two methods to check for convergence are used, soft convergence versus hard convergence. Soft convergence is based on the objective value resulting from an approximate optimization. Hard convergence is based on the objective value resulting from the finite element analysis. Hard convergence is often preferred, however, if the computational costs of a full finite element analysis are high and only relatively small design adjustments are made comparatively to the prior analysis cycle, soft convergence may be a cost-effective termination point. In this research, hard convergence is required for optimization to be completed.

Hard convergence indicates that an optimum feasible design is found. However, hard convergence does not necessarily yield to a unique design. Only if the relative changes in properties or the relative changes in design variables are satisfied, a unique design is found. If hard convergence is reached, but the relative change in the design variables is not satisfied, this indicates multiple, non-unique, designs are optimum, which indicates that there is low sensitivity with respect to the design variables and the objective value, for at least some design variables. This would allow for a trade-off in designs based upon manufacturing or cost considerations.

3.4. Design of Experiment Results

In addition to some baseline analysis and a sensitivity analysis, a design of experiments is performed. This goal of this design of experiments is to test the robustness of the framework and to see common features of efficient structural layouts. For sampling of the design of experiments, a Latin Hypercube Sampling method is used. Latin hypercube sampling is used, as LHS ensures that the set of random numbers generated is representative of the sampling space. Contrary to random sampling, that does not guarantee a selection that is representative of the sampling space. For this reason, Latin hypercube sampling is the go-to sampling method for design of experiments. The layout variables that are included in the design of experiments and the respective bounds are shown in Table 3.4.

Layout Parameter	Baseline Value	Lower Bound	Upper Bound
Stringer Pitch Upper Surface [m]	0.2	0.01	0.5
Stringer Pitch Lower Surface [m]	0.2	0.01	0.5
Rib Pitch [m]	1	0.8	2
Orthogrid Pitch [m]	0.4	0.1	0.5
Stringer Shape	0	0	1
Number of Spar	2	1	3
Location Spar 1	0.15	0.1	0.9
Location Spar 2	0.8	0.1	0.9
Location Spar 3	-	0.1	0.9

Table 3.4: Overview of the layout parameters that are varied in the design of experiments. The location of the spars is given as a percentage of chord. The stringer shape value relates to the stringer shape, zero is an L-shaped stringer, one is a C-shaped stringer.

4

Verification

The framework developed in this study is used to estimate the weight of the outer wing of the Flying-V. A baseline design is defined to start the weight estimation study. Furthermore, multiple concepts of the outer wing are compared, a sensitivity analysis is performed, and a Design of Experiments is done. The baseline model is verified with a modal analysis and a mesh convergence study. For verification of the framework, an example problem of NASTRAN is solved with the framework. Furthermore, the weight estimate and thickness distribution results are validated by comparison with a simplified analytical model.

4.1. Modal Analysis

With modal analysis, natural frequencies and mode shapes of the finite element model are calculated. Modal analysis can be performed without the application of loads and is thus suited for verifying the model without the influence of results. The modal analysis will fail if there are any unconnected nodes or extreme differences in stiffness. Reasons why the modal analysis might fail:

- Incorrect Structure Generation, resulting in stringers outside the main shape.
- Incorrect Shape Generation, resulting in a structure with holes or discontinuities.
- Incorrect Mesh Generation, resulting too extreme mesh element shapes, giving a failure of the mesh elements check performed by NASTRAN.
- Incorrect Finite Element types assigned to structure, resulting in, for example, errors in the input file reading because beam properties are tried to be assigned to surfaces.
- Incorrect Boundary Conditions.
- Incorrect BDF file writing, resulting in physically impossible meshes or structures due to wrong connectivity.

A successful modal analysis thus can be used to partly verify the model and the framework. A successful analysis will give the requested number of natural frequencies and mode shapes. The mode shapes are mainly determined by the relative stiffness of the structure and the constraints applied to the model. The resulting mode shapes can be used to visually inspect if indeed the mode shapes match with the expected results based on stiffness and constraints.

The results of the modal analysis show that the model acts as one structure, which indicates correct connectivity of the entire structure. An overview of the first ten mode shapes is given in Appendix section B.1. Here, the first mode shapes show deformation of the entire structure, followed by deformations of the winglet. This is in line with expectations based on the relative stiffness and the boundary conditions.

4.2. Mesh Convergence Study

A mesh convergence study is performed to verify the mesh size. Several grid spacings are applied to the baseline model and the maximum deflection is calculated. The results are show in Figure 4.1. A grid spacing of 0.1 is chosen for the remainder of this study. This spacing shows a converged result and ensures the same grid spacing can be used for all design sensitivity studies, as this grid spacing allows for smaller stringer spacing as well. A Mesh Convergence class is used for this convergence study, the mesh convergence can be automatically checked with this class.

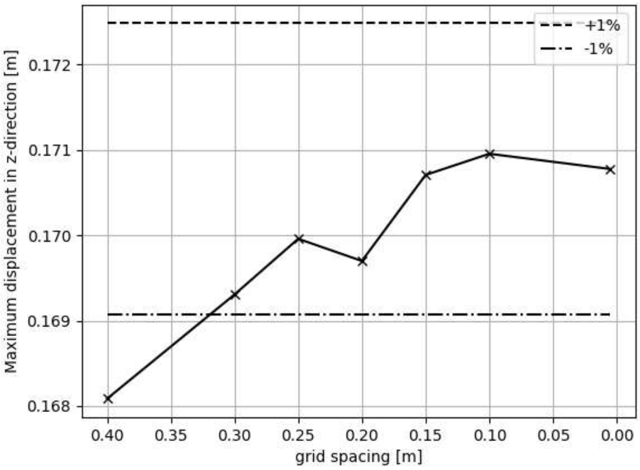

Figure 4.1: Mesh Convergence Plot

4.3. NASTRAN example - Cantilevered Plate

The cantilevered plate example of NASTRAN is chosen as a means to verify the framework [5]. The cantilevered plate example is comparable to the outer-wing, as multiple load cases are applied, yet there is only one design objective. The design variables are mainly sized by shear stress and bending stress. Moreover, the boundary conditions and the general loading and set up is similar, and an optimum thickness distribution is a desired. Both a tip load and a uniform distributed pressure loading are applied in z-direction. With the clamped boundary conditions, it is expected that the highest stresses are induced by bending due to the tip load applied. This would result in the highest stresses at the clamped side of the plate. So, the expected highest thickness is at the clamped side of the plate, reducing in thickness along the length.

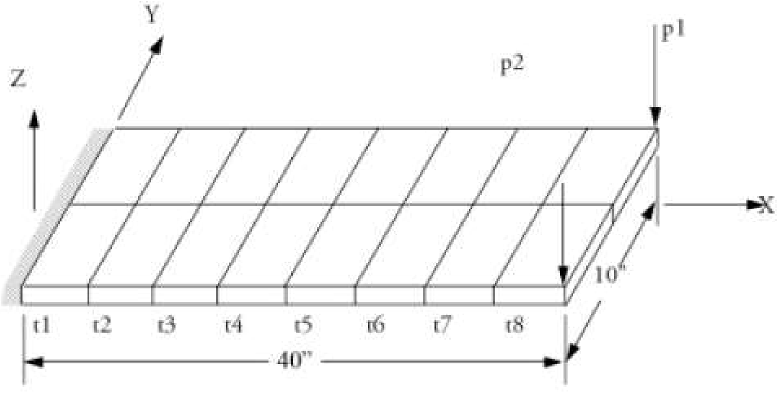

Figure 4.2: Cantilevered plate model of NASTRAN [5].

The input model and the thickness distribution results from the analysis performed with the developed framework, can be seen in Figure 4.2 and Figure 4.3. The numerical results of the analysis can be seen in section B.2 and show to be identical to the results generated by NASTRAN. Here, clearly, the greatest thickness is required at the root and the thickness gradually reduces going towards the tip of the plate. This is in line with expectations from the combination of static tip loading in combination with equally distributed pressure load along the entire section. The results prove that the framework does indeed write the input file correctly and the design problem is defined in line with the user input. The consistency of the results provided by NASTRAN and the results generated by the framework, verify the working of the framework.

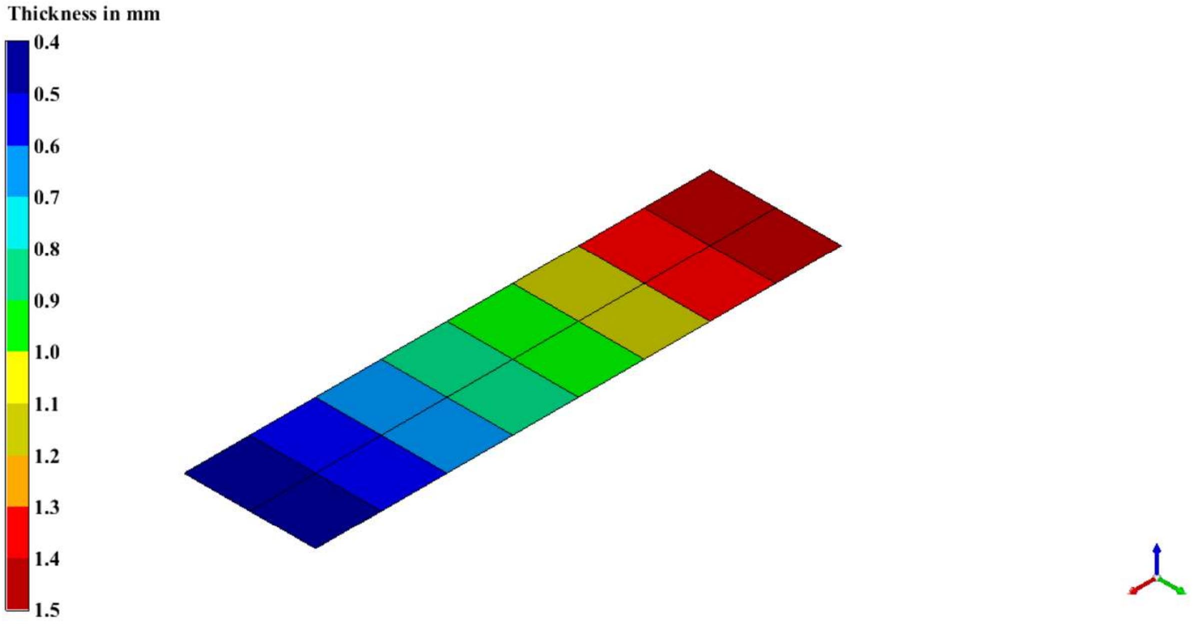

Figure 4.3: Cantilevered plate thickness distribution results visualized in ParaPy.

4.4. Analytical Verification

The results of this research will show a thickness distribution for the Flying-V. Although the cantilevered plate example verified the framework, the model and analysis of the outer wing is not fully verified by the cantilevered plate example and the modal analysis. It would be ideal to verify the model results with an expected a thickness distribution or weight estimate. However, there is not yet a lower-fidelity thickness distribution or a general idea on what the thickness distribution of the outer wing of the Flying-V is expected to look like. And although there are quite some similarities between the outer wing of the Flying-V and a conventional aircraft wing, there are also a lot of difference that make direct comparison complicated. To verify the thickness distribution that results from the Flying-V model, a simplified model is generated. This simplified model is made to bridge the gap between the cantilevered plate model and the outer wing models analysed in this research.

First, the thickness distribution is determined analytically. This solution is compared with the thickness distribution resulting from analysis with the developed framework. These framework results are referred to as the FEA results, in this section. For the current comparison, only bending stresses are considered. The analytical approximation of the bending stress, used in this study, yields more accurate results than a similar approach for shear. Moreover, in the analysis only the skin thickness is sized, no sizing of the stringers or spar webs is done. The simplified outer wing is shown in Figure 4.4

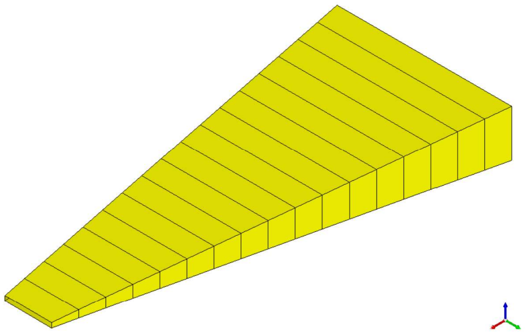

Figure 4.4: Cantilevered plate model of NASTRAN.

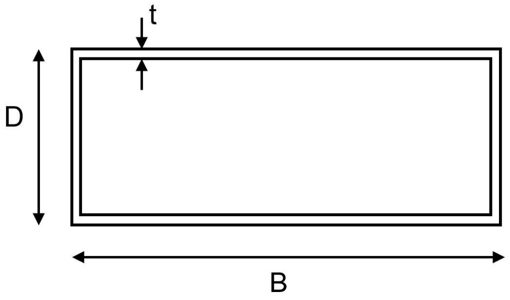

Figure 4.5: Cross-section of the simplified outer wing model.

The Structural model is simplified to a rectangular, double-tapered wing box structure, resembling the outer wing of the Flying-V. The winglet structure is neglected in this approximation; however, a tip moment is added to introduce the aerodynamic forces from the winglet. The box structure is modelled as a beam, for the analytical analysis. Moments are only applied around the beam's x-axis, representing the aerodynamic forces acting perpendicular to the lower wing surface, acting in z-direction. The torsion induced by the distance between the aerodynamic centre and the geometric centre of the cross-section, is neglected in this simplified model. It is assumed that the material is homogenous and behaves in a linear-elastic matter. The Euler-Bernoulli beam theory is applied. For the analytical approximation, a continuous change in skin thickness is allowed.

The continuous change in skin thickness allows for a fully stressed beam, however the non-prismatic beam shape does make exact analysis rather tiresome. The flexure formula is proven to give approximately correct results for predicting the bending stresses in non-prismatic sections if the taper of the beam is not too severe [16]. The flexure formula cannot be used for shear stresses in tapered beams, as the results are not in line with the exact solution. However, full derivation of the tapered beam shear stress is beyond the scope of this research. It is assumed that the shape of the thickness distribution is driven by the bending stresses, and the shear stress are neglected for this verification step. With the fully stressed beam approach, the thickness is determined as a function of x along the length of the beam model. The stress inside the beam will be set equal to the yield stress of the material by varying the thickness. A safety factor of 1.5 is applied to the yield stress, similarly to the outer wing analysis. The material properties of AL 2024-T352 are used, again, similar to the outer wing analysis, see Table 2.3.

It is assumed that the material is homogenous and behaves in a linear-elastic matter. The Euler-Bernoulli Beam theory (Equation 4.2) can be applied, as well as the Flexure Formula (Equation 4.1). With the Flexure Formula the stress inside the beam can be determined, and with the Euler-Bernoulli theory, the internal moment in the beam can be determined.

$$\sigma = -\frac{My}{I} \tag{4.1}$$

$$\frac{\mathrm{d}^2}{\mathrm{d}x^2}\left(EI\frac{\mathrm{d}^2 w}{\mathrm{d}x^2}\right) = q \tag{4.2}$$

Assuming, in the derivation, that the Flexural Rigidity, EI, is constant the Euler-Bernoulli equation can be simplified. Defining the distributed load as a linear equation, see Equation 4.3, the internal moment can be determined with Equation 4.4. The assumption that the Flexural Rigidity is constant, can only be applied as the taper is assumed not to be too severe. Keep in mind that due to the double-tapered geometry the Flexural Rigidity is not constant, and the second moment of area constantly changes. Any discrepancies between the FEA results and the analytical results could be caused by this assumption.

$$q = w_1 + w_2 \cdot x \tag{4.3}$$

$$EI\frac{d^4 v}{dx^4} = w_1 + w_2 \cdot x \tag{4.4}$$

The distributed load is defined as $w_1 = \frac{L_{total}}{9}$ and $w_2 = -\frac{L_{total}}{9} \cdot L$. To result in a moment distribution similar to the moment distribution in the outer wing, with the loading as described in subsection 2.2.5. With the distributed load, $w(x)$, known, the internal moment can be derived. At every integration step, boundary conditions or initial conditions need to be applied in order to solve for the integration constant. The integration with the assumed boundary conditions is shown next.

Integrating the equation for the loading once gives the equation for the shear force inside the beam Equation 4.5. Due to the assumption of the constant structural rigidity factor, this equation for internal shear, is not accurate. Applying the condition that at x = L the shear force V = 0 gives Equation 4.6. Here, L indicates the location of the tip of the wing. As the distributed force is modelled as a linearly distributed force with the maximum magnitude at the root and zero at the tip, this boundary condition holds.

$$V(x) = \int w(x)dx = \int (-w_1 - w_2 x)dx = -w_1 x - \frac{w_2}{2}x^2 + C \tag{4.5}$$

$$V(x) = -w_1 x - \frac{w_2}{2}x^2 + w_1 L + \frac{w_2}{2}L^2 \tag{4.6}$$

Next, Equation 4.6 is integrated again to end up with the equation for the internal moment along the beam Equation 4.7. Applying the boundary condition that at x = L the moment $M = M_{tip}$, Here, $M = M_{tip}$, represents the aerodynamic forces acting on the winglet. Equation 4.8 is derived.

$$M(x) = \int V(x)dx = \int (-w_1 x - \frac{w_2}{2}x^2 + w_1 L + \frac{w_2}{2}L^2)dx = -\frac{w_1}{2}x^2 - \frac{w_2}{6}x^3 + w_1 Lx + \frac{w_2}{2}L^2 x + C \tag{4.7}$$

$$M(x) = -\frac{w_1}{2}x^2 - \frac{w_2}{6}x^3 + w_1 Lx + \frac{w_2}{2}L^2 x - \frac{w_1}{2}L^2 - \frac{w_2}{3}L^3 + M_{tip} \tag{4.8}$$

Now the internal moment is derived, the flexure formula can be solved for the thickness. The moment of inertia of the wing is given by Equation 4.12. With the dimensions B, D and t as shown in Figure 4.5. All cross-sectional dimensions are a function of x, and B and D are defined with Equation 4.9 and Equation 4.10. With L the length of the wing, as set to 17 [m]. All geometrical dimensions are determined such that the structure best represents the behaviour of the baseline outer wing structure.

$$B = 7.5 - \frac{5.5}{L}x \tag{4.9}$$

$$D = 2.0 - \frac{1.8}{L}x \tag{4.10}$$

$$y(x) = 1 - 0.9/(L+1) * x \tag{4.11}$$

$$I = \frac{BD^3 - (B-2t)(D-2t)^3}{12} \tag{4.12}$$

Combining Equation 4.12, with Equation 4.8 and Equation 4.1, one can derive the equation to determine the thickness required Equation 4.13.

$$16t^4 + (-24D - 8B)t^3 + (12D^2 + 12BD)t^2 + (-6BD^2 - 2D^3)t - 12\frac{M(x)y(x)}{\sigma_{allow}} = 0 \tag{4.13}$$

Simplifying and neglecting the terms related to t^4 and t^3, t can be solved with Equation 4.14.

$$t = \frac{6BD^2 + 2D^3 - \sqrt{(-6BD^2 - 2D^3)^2 - 4\frac{12M(x)y(x)}{\sigma_{allow}}(12BD + 12D^2)}}{2 * (12BD + 12D^2} \tag{4.14}$$

This analytical model results in the thickness distribution as shown in Figure 4.6. This shows that the greatest skin thickness is required at the tip of the beam. Here, at the tip of the beam, the height and width of the beam are the smallest and a moment is already introduced by the moment caused by the winglet. The increase in thickness compensates for the other dimensions to still result in a second moment of area that is able to withstand the stresses introduced by the internal moment. Interestingly, the lowest skin thickness is achieved close to the middle of the beam. This can be explained with the cross-section dimensions and the internal moment building up towards the clamped root.

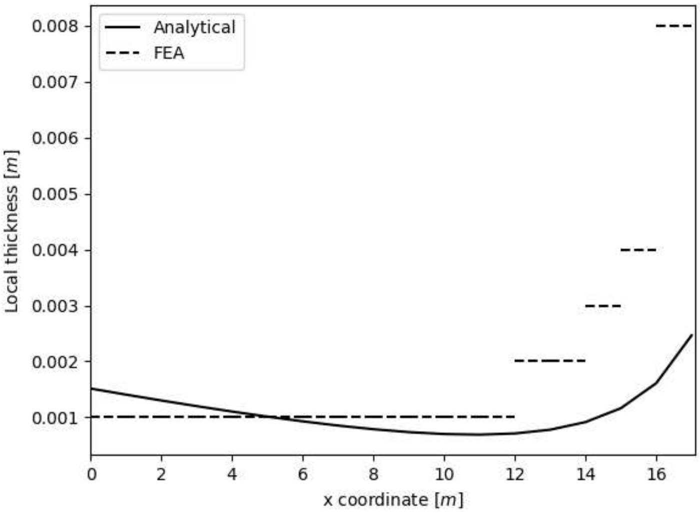

Figure 4.6: Plot comparing the thickness distribution as approximated analytically versus the thickness distribution as a result from a SOL200 analyses generated by the framework developed in this research.

The corresponding internal moment and second moment of area, along the beam's x-axis is showing in Figure 4.7 and Figure 4.8, respectively. This shows that indeed by the shown thickness distribution, the distribution of the internal moment and the second moment of area are equal, which is to be expected.

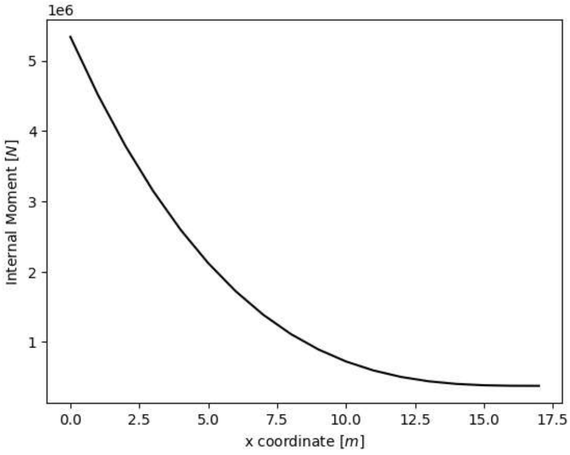

Figure 4.7: The internal moment, in the simplified Flying-V outer-wing model, as calculated with the analytical method.

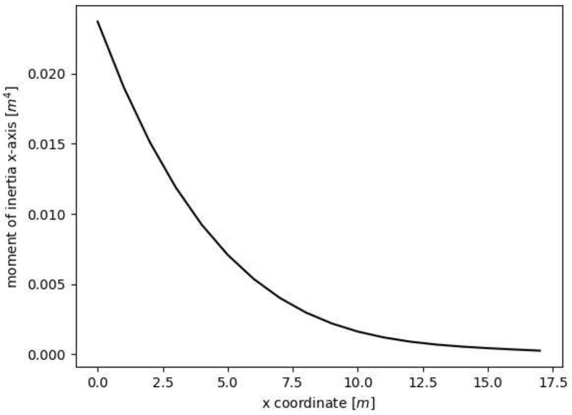

Figure 4.8: The second moment of area around the x-axis of the simplified Flying-V outer wing model after sizing for thickness.

The results clearly shows that although the internal moment increases exponentially going from the tip to the root of the wing and the moment of inertia also increases exponentially going from the tip to the root, the thickness does not increase exponentially due to the change in cross-sectional area and the non-linear relation between thickness and moment of inertia. A plot showing the resulting skin panel thickness as calculated analytically is shown in Figure 4.9.

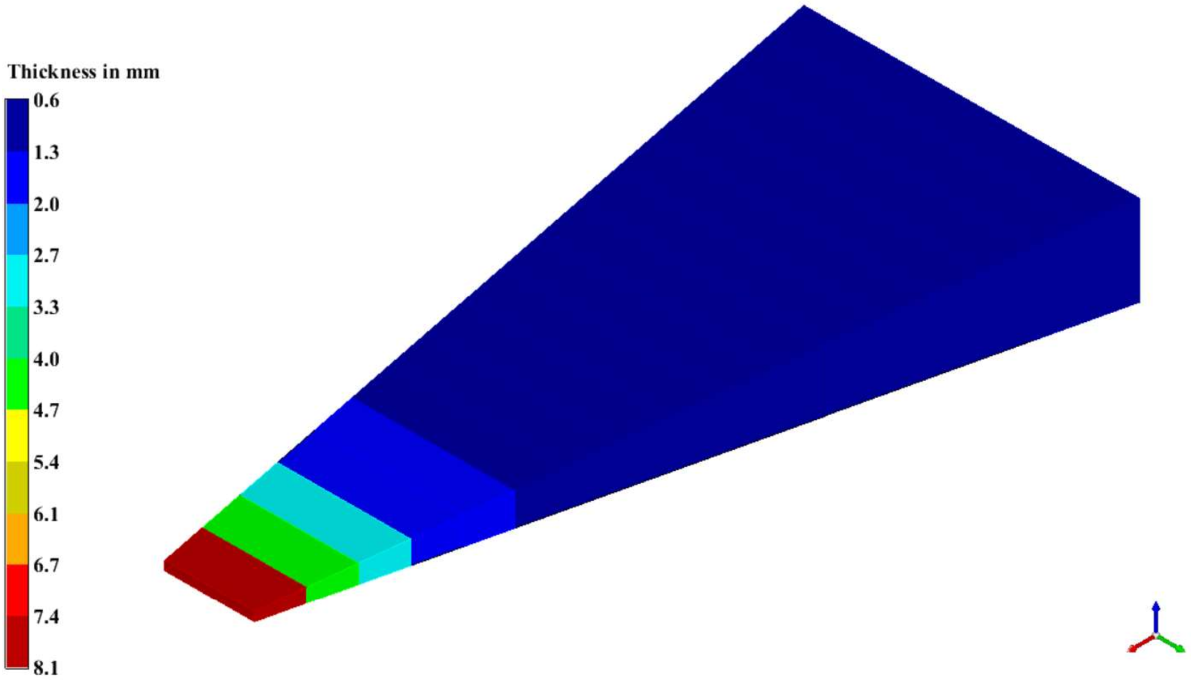

Figure 4.9: Cantilevered plate thickness distribution results visualized in ParaPy.

Interestingly, the thickest skin thickness is achieved at the tip of the wing, this seems odd at first due to the greatest internal bending moment at the root of the wing. However, the cross-sectional area at the tip is a lot reduced, and as this means an even greater decrease in the local moment of inertia, the thickness is increased, to withstand the stresses. A similar thickness distribution is also expected in the baseline outer wing structure.

In Table 4.1, the last gap between the analytical model and the baseline model as will be analysed in this study, is made. The weight estimate as given by the analytical model is almost identical to the weight estimate that results from a FEA of the simplified model if the lift forces are introduced as moments, and shear forces are neglected. When all forces are considered, and the structure is also sized for shear loads, the estimate of the total structural weight of the wing increases. Comparing this simplified model with the actual baseline structural model of the wing, does indicate that the simplified model is close to the actual model. Behaviour is similar even though now, not only skin sizing is available but also the stringers, spars and the winglet have become part of the structural model. Moreover, the actual weight has been applied to the model. The model is used to verify the set-up of the framework and the thickness distribution that results from the framework.

Name	FEA Weight $[kg]$
Analytical Moment	660
Simplified Moment	657
Simplified Moment + Shear	1108
Simplified Moment + Shear + Torsion	1108
Full Moment + Shear + Torsion	1372

Table 4.1: Verification FEA results. Here, the simplified model refers to the rectangular model, skin only, and the full model refers to the baseline design, including skin, stringers, spars, winglet, and the true loads etc.

5

Results

In this chapter, the results of the experiments, conducted with the framework developed in this study, are shown. The results of the experiments with the outer wing, both aim to provide a weight estimate for the outer wing and showcase the possibilities of the framework. The first sections will discuss some of the initial problems that were discovered when starting the experiments. This is followed by a section that presents the baseline results of several cases. This is followed by a section that shows the results of a sensitivity study that aims to provide some confidence in the framework and the results. A design of experiments is performed and the results from the design of experiments are shown and elaborated upon in the next section. Lastly, a final weight estimate of the baseline outer wing model is given and compared to previous estimates.

5.1. Initial Results

Convergence of the optimization proved to be difficult, initially. High stress peaks did occur in the connection of the wing to the winglet. This was solved with the Spar Correction class; with the spars connecting the wing and the winglet, the stress peaks could converge. Additionally, stress peaks did occur at the root, where the boundary conditions are applied. By including the vertical edges of the spars, to the rigid body element that is used to apply the boundary conditions to, the stress peaks are reduced. After fine-tuning the optimization settings, convergence could be achieved for static stress analysis.

For buckling analysis, the convergence problems proved more difficult to solve. First, buckling of the spar webs did occur already at the initial baseline design. After adding the orthogrid structure, no buckling of the spar webs did occur for the initial analysis, and analysis started from an initial feasible design. However, the optimization algorithm still failed to give a converged result and did not end up with a feasible design. With a refined grid spacing of 0.02 [m] and with an analysis taking the first 20 buckling modes into account, convergence can be achieved. This, however, leads to an analysis with extremely high computational costs, about 10 times the computational costs of the static stress analysis. Moreover, no thorough sensitivity study could be performed to prove the stability of the analysis. Taking the buckling analysis into account in this framework proved to be infeasible for the current set-up and resources. Buckling is not considered in the results shown in the upcoming sections, and the designs are sized on static yield strength and fatigue.

5.2. Baseline Results

The baseline outer wing structure is sized for static yield strength and fatigue. The design rib pitch is 1.0 [m], stringer pitch is 0.2 [m] and the design has 2 spars, one front spar at 15% of the chord and one rear spar at 80% of the chord. The initial orthogrid spacing is 0.4 [m]. The initial thickness of all elements is 8 [mm]. This leads to an initial design that is feasible, with the highest stresses occurring in the winglet blend and the root leading edge. The stress distribution of this initial analysis is shown in Figure 5.1.

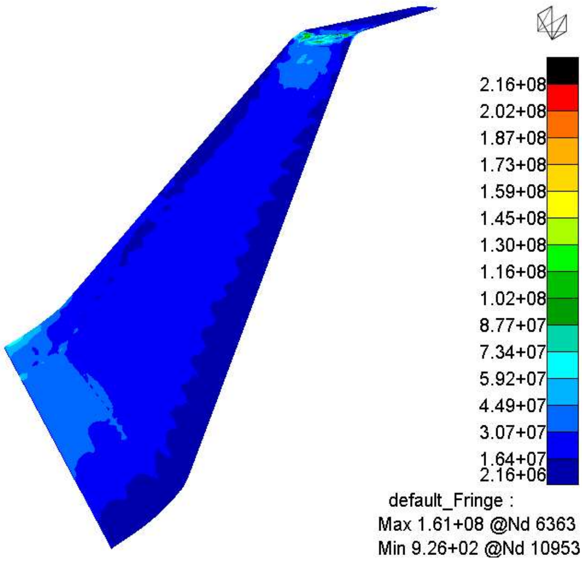

Figure 5.1: Von Mises stress plot in [Pa], showing the stresses in the skin. This shows the results from cycle 1, the stress in the initial design.

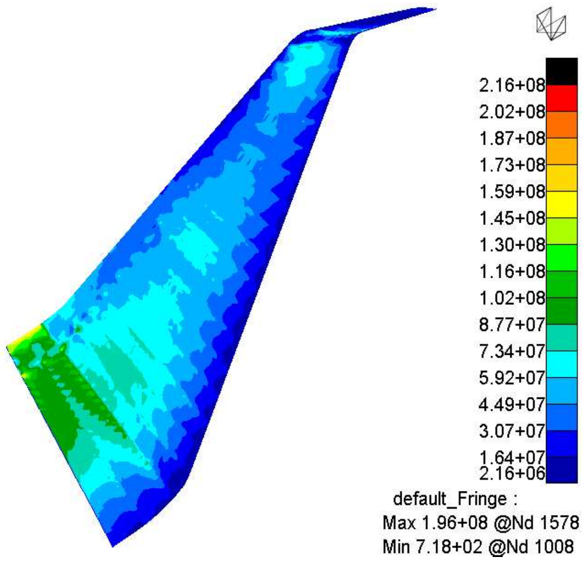

Figure 5.2: Von Mises stress plot in [Pa], showing the stresses in the skin. This shows the results from cycle 4, after some improvements to the design have been made by the optimizer.

The baseline analysis contains about 170,000 Degrees of Freedom and the total analysis until an optimum is found and convergence is achieved takes 73623 CPU seconds. The behaviour of the optimizer can be visualized in Figure 5.1, Figure 5.2 and Figure 5.3. The figures clearly show that the optimizer changes the design variables such that the structure is nearing a fully stressed design. However, as just one design variable per skin section and one design variable per stringer, is available, a fully stressed design cannot be reached. Moreover, it is difficult to directly predict the stresses that occur in neighbouring sections when the skin thickness of one section is decreased, such that it is not necessarily the case that all panels can be fully stressed even if there would be more design variables available in chordwise direction. Keep in mind that only the Von Mises stresses on the outside of the skin are shown. The design is driven by the Von Mises stresses occurring on the inside of the skin as well. Some stresses that did drive the design might not be visible in these plots.

The trailing edge is lightly loaded compared to the leading edge of the wing. This can be explained by the combination of the sweep, the kink, and the torsional moment around the aerodynamic chord. All resulting in higher stresses closer to the leading edge. Moreover, the trailing edge spar takes most of the shear loads, reducing stresses in the skin of the trailing edge. The highest stresses occur in the spars going from wing to winglet. This can probably be explained by the low cross-sectional height of this structure and the redirection of the loading. This is also in line with the thickness distribution shown by the simplified model in verification. Additional stress peaks are present in the skin near the kink, at the leading edge. Likely caused by the compressive forces caused by bending and torsion of the wing and the sudden shape change at the kink.

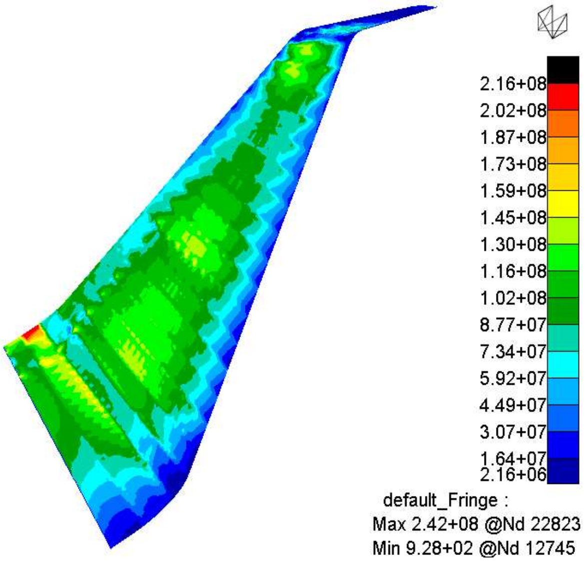

Figure 5.3: Von Mises stress plot in [Pa], showing the stresses in the skin. This shows the results from cycle 14, the final design cycle, showing the optimized baseline design.

In Figure 5.4, the stress inside the stringers is shown. This image also shows that most stringers have equal internal stress levels throughout the entire length of the stringer. At the location of the kink, a new section begins. This means that the stringers before the kink and aft of the kink could have a different thickness value, as they both have an individual design variable. The stringers, that have low internal stresses throughout the entire length, are sized by the minimum thickness value. Again, it can be seen that the trailing edge section is only lightly loaded.

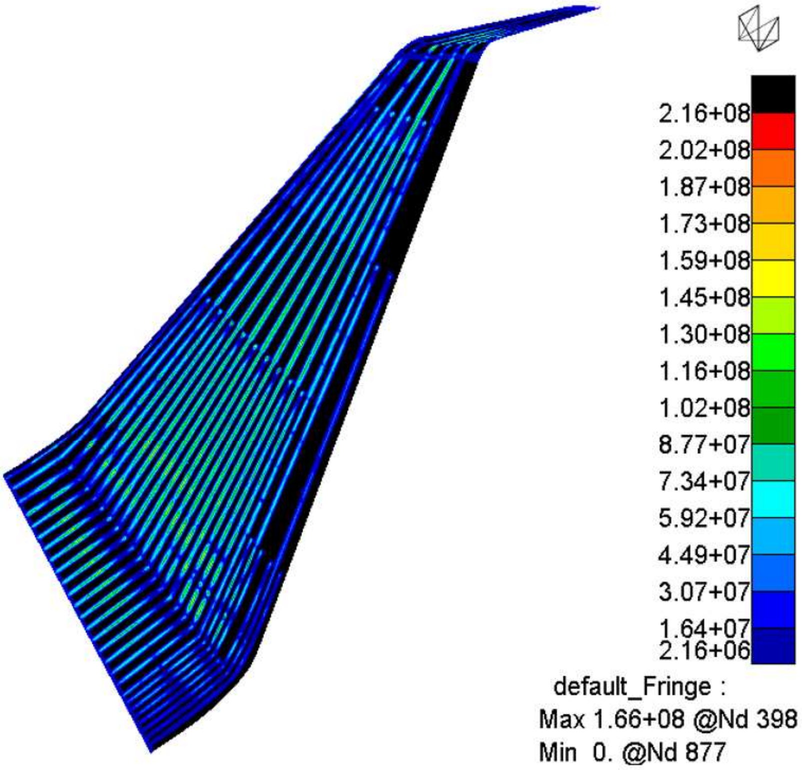

Figure 5.4: The combined stresses inside the stringers, or beam elements, in [Pa]. For the final optimized design.

In Figure 5.5 and Figure 5.6, the deformation of the outer wing is shown. These results show a great increase in deformation going from the initial to the final design. This is in line with expectations, as the thicknesses of the outer wing are reduced to end up with a light design. This lighter design is less stiff, which leads to more deformation. It can be clearly seen that the maximum deformation occurs at the tip of the winglet. As the total deformation is still relatively small compared to the size of the wing, the deformations are not expected to cause any issues. However, aerodynamic performance might be reduced due to deformation.

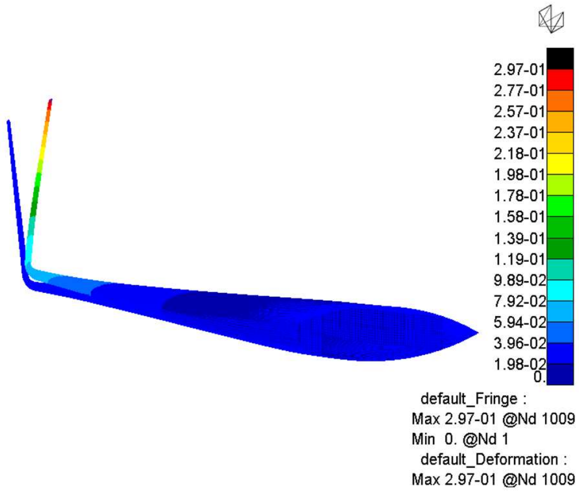

Figure 5.5: Deformation plot in [m], showing the deformation of the outer wing. This shows the results from cycle 1, the deformation of the initial design.

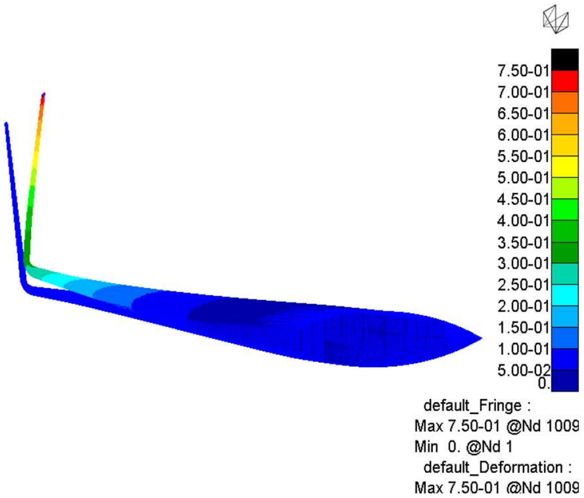

Figure 5.6: Deformation plot in [m], showing the deformation of the outer wing. This shows the results from cycle 14, the final design cycle, showing the optimized baseline design.

In Figure 5.7, the thickness distribution can be seen. The increase in thickness towards the wing tip might look surprising at first, as higher bending loads are experienced at the root of the wing. However, due to the great reduction in local second moment of area at the tip, higher local internal stresses do occur here. Just as seen in section 4.4, the highest skin thicknesses are required at the tip of the wing. As the shear load is applied proportionally to the planform area, the shear load is highest at the root, and it could be assumed that also the internal shear stresses are highest at the root. The lowest skin thickness does occur slightly in front of mid-span, ahead of the estimated location based upon the verification results. This can be explained due to the addition of shear loads and the non-linear reduction in height and width as assumed in the simplified verification model.

The thicker skin of the panel right after the kink can be explained as follows: The size of the stringers can only be determined once per section. The section is split right before and after the kink. The stringers inboard of the kink are generally of a greater size than the stringers outboard of the kink. This reduction in stringer size, will lead to a reduction in local moment of inertia, the increase in skin thickness compensates for this loss of stiffness due to the change in stringer size. The skin thickness is highest at the location of the blend connecting the wing and the winglet. All stringers have a thickness greater than 2.0 [mm] as can be seen by the red lines throughout the entire wing.

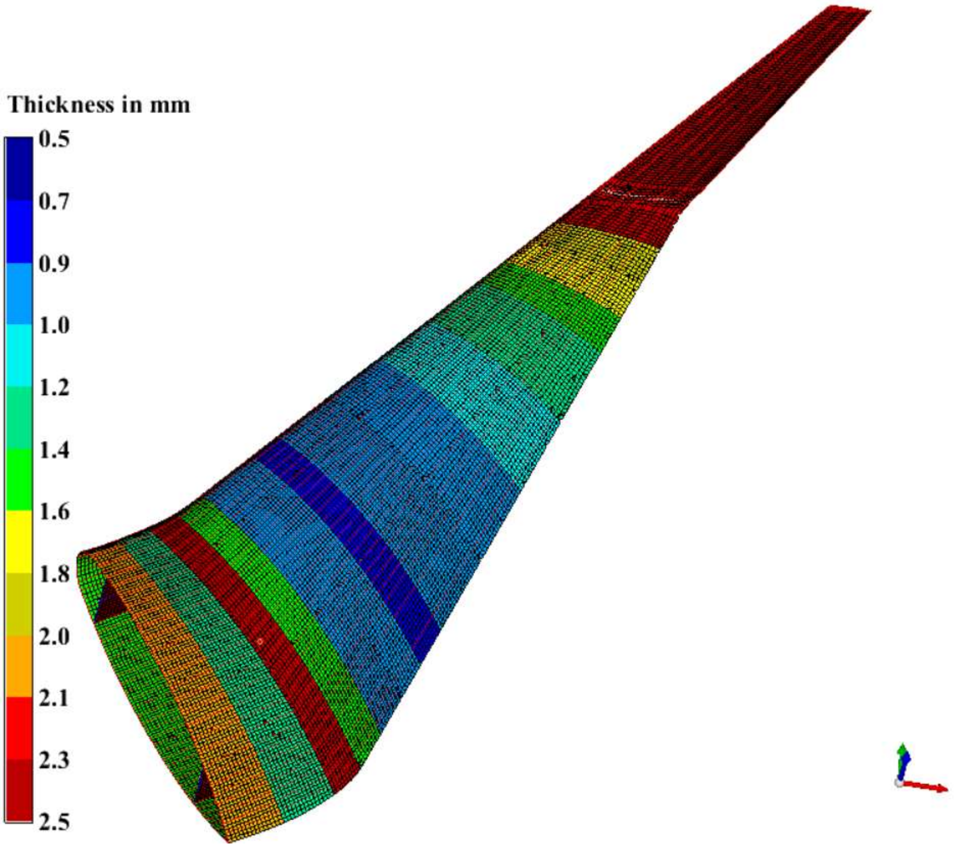

Figure 5.7: Plot showing the thickness in [mm] of the optimized baseline design. Both the skin and the stringers are plotted.

In Figure 5.8, only the stringers are shown. Notice that the legend has changed, as the stringers are generally thicker than the skin. Looking more closely at the stringer thicknesses, it can be clearly seen that the stringers closer to the leading-edge spar generally have a higher thickness than the stringers closer to the trailing edge spar. Moreover, the shorter stringers, and the stringers closest to the root, generally get a higher thickness. The stringer in the blend section connecting the winglet is assigned the highest thickness. Meanwhile, the stiffening elements that form the orthogrid structure are assigned the minimum gauge thickness. This is in line with expectations as the stiffening elements are added to prevent buckling of the spar webs, however, buckling is not sized for.

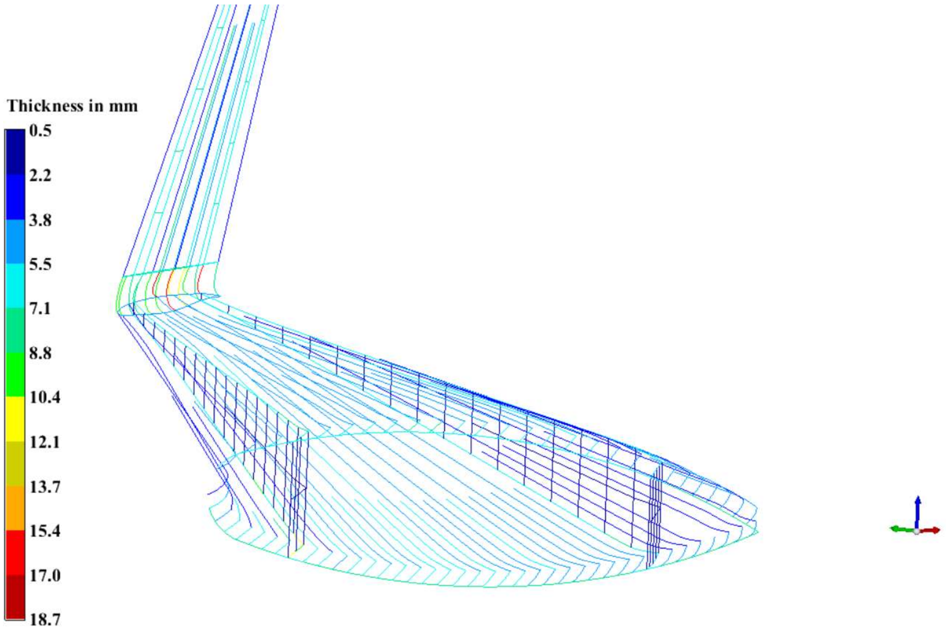

Figure 5.8: Plot showing the thickness in [mm] of the stringers of the optimized baseline design.

In Figure 5.9, the thickness distribution of the spar web thickness can be seen. At the leading-edge spar, a similar phenomenon to the skin thickness can be seen. Right after the redefinition of the stringer size, outboard of the kink, the spar thickness is momentarily increased. Interestingly, the stress in the skin and the spar near the trailing edge close to the kink is lightly loaded. The spar thickness is greatest at the blend connection of the wing and winglet, again in line with the phenomenon that can be seen in the skin thickness and explained by the fast reduction in cross-sectional area running towards the tip, and the forces and moments introduced by the relatively large winglet structure.

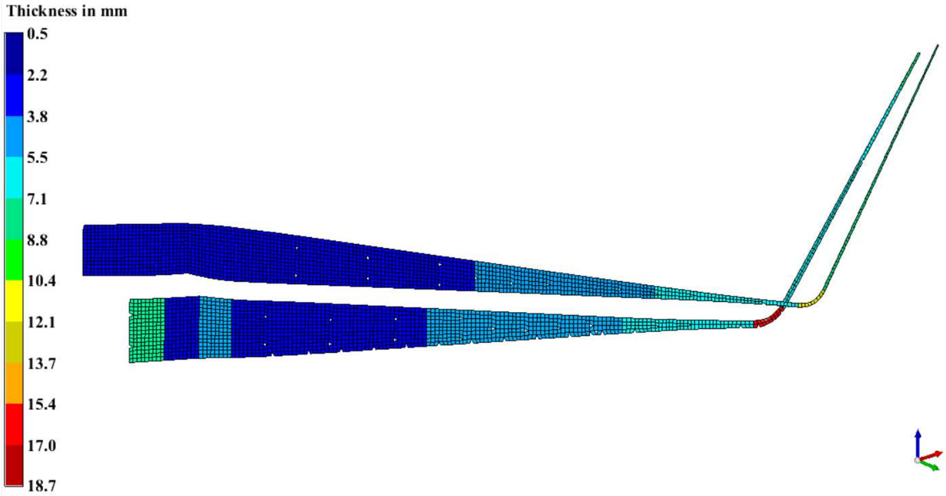

Figure 5.9: Plot showing the thickness in [mm] of the spars of the optimized baseline design.

The baseline results are compared to the results from an analysis on a NLES design, and a design that includes, or rather, excludes a flap surface from the analysis. An analysis combining both the NLES, and a flap is also performed. The results on the weight estimates are shown in Table 5.1. This clearly shows that a design that does include a leading-edge spar is more efficient than the same design that lacks a leading-edge spar. This can be explained by the shape of the cross-section that remains and the maximum transverse shear stress that occurs in common tube cross-sections. A round cross-section, or rather a curve section of a cross-section generally has a higher maximum shear stress value than a comparable rectangular cross-section, with all straight edges. The average shear stress is equal for both cross-sections however, the peak values are higher for the round or circular cross-section. With the removal of the leading-edge spar, the leading-edge skin has to take up more shear stresses. The leading-edge spar is thus more efficient than the NLES design. And introducing the NLES design comes at the cost of a 15% increase in weight.

The results of the Flap analysis show that introducing a flap does make the structure more efficient. As seen in the results of the baseline design, the trailing edge of the structure is lightly loaded, and the results of the flap analysis confirm that removal of the trailing edge do not impose greater stresses in the remaining structure. The influence of forces introduced by the flap on the outer wing are not analysed. It should be noted that the weight of the flap is not included in the total wing weight for this analysis. Most of the reduction in wing weight is thus simply caused because part of the structure, and its weight, is removed. However, the removal of the flap structure makes the wing structure less stiff, leading in this case to a more efficient design. The outer wing structure does reduce in total weight by roughly 20% when a flap structure is removed.

Name	FEA Weight $[kg]$	Fraction
Baseline	2407	1
NLES	2767	1.15
Flap	1904	0.79
NLES + Flap	2232	0.93

Table 5.1: Baseline Results, comparing the NLES design with the baseline design. The Flap model does not include the weight of the Flap.

The stress plots showing the final stress distribution in the optimized cases can be seen in Figure 5.11, Figure 5.12 and Figure 5.13. In Figure 5.11, it can be clearly seen that the stresses in the skin to the root and leading edge, are increased compared to the stresses in the baseline, LES, design. The lack of the leading-edge spar imposes additional stresses in the skin close to the leading edge, especially at the root. This is in line with the expectations.

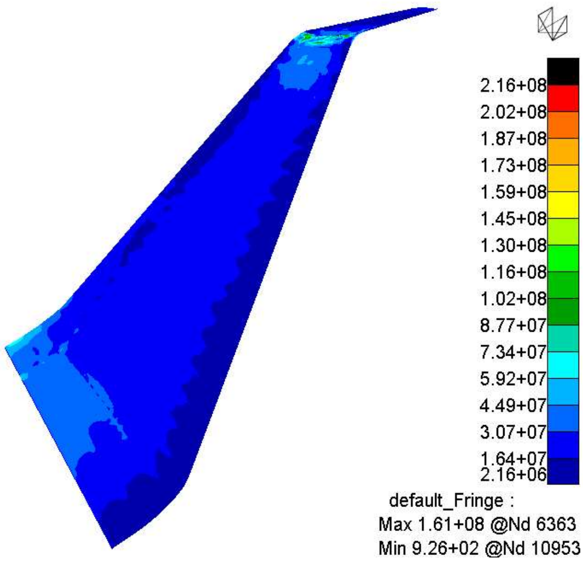

Figure 5.10: Von Mises stress plot in [Pa], showing the stresses in the skin. This shows the results from cycle 14, the final design cycle, showing the optimized baseline design.

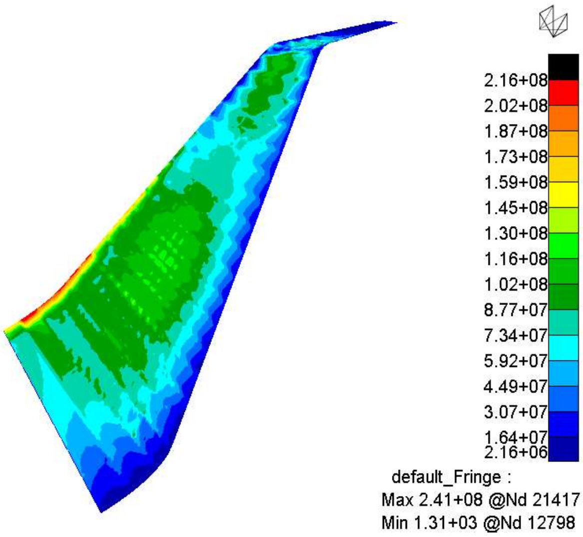

Figure 5.11: Von Mises stress plot in [Pa], showing the stresses in the skin. This shows the results of the optimized NLES design.

In Figure 5.12, the baseline design with flap, can be seen. The removal of the flap does not have a great influence on the stresses within the wing. The trailing edge was already lightly loaded for the baseline model, so a flap can be fitted without much compromise. The reduction in the cross-section area closer to the wing tip, does lead to slightly increased stresses towards the tip. In Figure 5.13, the stress distribution in the optimized structure for the NLES design with flap is shown. This clearly shows to be a combination of both the NLES and the baseline flap model. The skin at the leading edge shows the highest stresses and the resulting design is close to fully stressed.

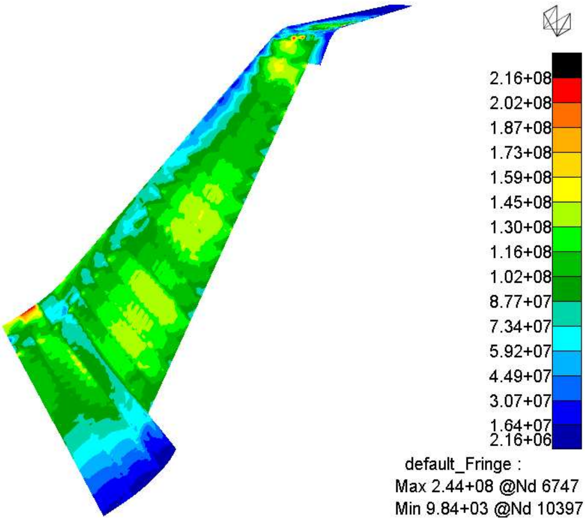

Figure 5.12: Von Mises stress plot in [Pa], showing the stresses in the skin. This shows the results of the optimized Baseline with Flap design.

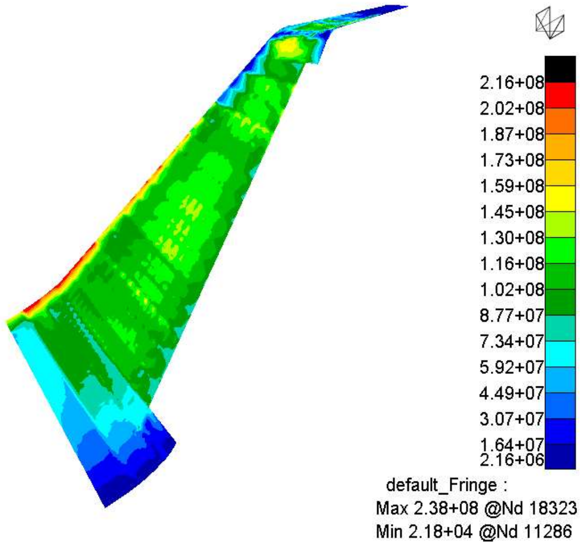

Figure 5.13: Von Mises stress plot in [Pa], showing the stresses in the skin. This shows the results of the optimized NLES with Flap design.

5.3. Sensitivity Study

A sensitivity study is performed to see the influence of the design choices that are made in this study. To perform this sensitivity study, the baseline model is analysed again, but this time without a minimum gage value for the design variables. Several design choices are included in the sensitivity study. An overview of the results of the sensitivity can be seen in Table 5.2.

Name	FEA Weight [kg]	Fraction
Baseline - No Min. Thickness	2019	1
More Stringer DESVARS	2450	1.21
More Stringer + More Skin DESVARS	2054	1.02
No Stringers	2211	1.10
Stringer Pitch 0.5 [m]	2321	1.15
No Spars	2084	1.03
RBE DOFs 123456	2375	1.18
Rib pitch 1.5 [m]	2363	1.17
Rib pitch 2.0 [m]	3365	1.66

Table 5.2: Sensitivity Study Results. The fraction indicates the FEA weight fraction of the specific design compared to the baseline without minimum gage values for the design variables.

One of the design decisions evaluated in the sensitivity study is the total number of design variables, as this is one of the most important parameters defining the design problem. A trade-off between computational effort and weight saving potential was continuously made when defining the design problem. The first analysis of the sensitivity study compares the baseline with a design problem where the stringers can be defined at every rib bay, instead of per section. This leads to a great increase in computational effort, not only as a direct result of the increased number of design variables the optimizer must evaluate at every run. Rather, the run time is increased due to the increased number of optimization cycles required before convergence. The final weight is way higher than the weight estimated with less design variable for the stringers, this is likely because the optimizer got stuck in a local optimum, and the increased number of design variables made it more difficult for the optimizer to converge. Moreover, the run-out stringers, are likely to already provide the variation in stiffness required going from the root to tip, without the need for a change in stringer size.

To test this hypothesis, another analysis was performed with the increased number of design variables for the stringers and an increased number of design variables for the skin as well. At every pocket between ribs and stringers, the skin now gets an individual design variable. This greatly increase the total number of design variables. This design problem no converges to a close to similar weight estimate as the baseline design problem. However, it takes more computational power to get there. The increase in design variables for the skin thickness thus is expected to be beneficial for the overall weight. However, from a manufacturing point of view, it is unlikely that the skin thickness can be changed so often. And the increase in computational costs limit the analysis possibilities. It is expected that the increased number of design variables for skin thickness has the potential to decrease the structural weight of the wing as the stress plots from the baseline analysis show the difference in stress in the skin close to the leading edge and trailing edge, compared to the stresses around mid-chord. The weight saving potential, however, is not considered great enough to adjust the design problems to include the additional design variables.

To check the effect of the stringers and verify that the stringers do allow for an increased structural efficiency, the baseline analysis is compared to a design that does not have any stringers. This clearly shows that the stringers, and the added design variables that come with the stringers, allow for a more optimized result. An analysis, with an increased stringer pitch of 0.5 [m] does show that the stringer pitch value does influence the overall weight estimate. And care should be taken in deciding upon the stringer pitch value, to allow for an optimal design.

To see the influence of the spars on the design, an analysis is performed without the spars. This does not seem to have an influence and the weight estimate. By changing the values for the design variables of the stringers and the skin, enough design freedom is given to compute a close to optimum design.

To test the influence of the ribs on the design, the rib pitch is changed. However, first, an analysis is performed where the ribs are not only adding stiffness in the x,y, and z-direction however, also in all 3 rotational directions. This leads to a design problem set up, similar to the case where all rib bays would be clamped constraint. This leads to an increase in weight. Which can be explained by an increase in stresses due to an increase in stiffness. Increasing the rib pitch results in an increase of estimate weight as well. This can be caused by multiple reasons. First, the increase in rib pitch, directly results in less design variables for the skin thickness and the spar web thickness. Secondly, the increase in rib pitch, results in a decrease in number of ribs, which means that the loads will be more like point loads and less like a distributed load. A rib pitch of 1 [m] is assumed to be the best trade-off between computational efficiency and reliable weight estimate.

Another design choice to consider is the stress concentration factor, chosen to determine fatigue failure. The value of 4.5 accounts for a broad range of attachment and bonding techniques. If more details on the manufacturing are known, it is likely that this stress concentration factor can be decreased. To see if fatigue is driving the design, multiple stress concentration factors are compared. The results in Table 5.3, show that fatigue is indeed driving the design, and the stress concentration factor does directly influence the weight estimate. The conservation choice for 4.5 is still considered valid.

Name	FEA Weight $[kg]$	Fraction
Baseline - No Min. Thickness - $K_t = 4.5$	2019	1
$K_t = 0.0$	1372	0.68
$K_t = 2.0$	1811	0.90
$K_t = 3.0$	1856	0.92
$K_t = 4.0$	1956	0.97
$K_t = 5.0$	2208	1.09

Table 5.3: Sensitivity Study on the Stress Concentration Factor used for Fatigue analysis.

5.4. Design of Experiment Results

One of the main reasons of the design of experiments was to test the robustness of the framework. A sample size of 50 individuals was chosen, of which 5 individuals failed. This means the framework works for 90% of the cases. The 5 individuals failed due to mesh element tolerances being exceeded. Often this was caused by a layout configuration where the spars are located too closely to one another, within .1, percentage of chord. This results in mesh errors as the fem shape generation, the fuse operator, does not guarantee a perfect shape. When the elements are too close, the fuse operator has difficulties with selecting the correct lines to generate the shape. For this reason, some lines that are very close to each other are both selected for shape generation, where these lines should be considered the same line. This leads to high skew angles for the mesh elements that are generated between the lines. NASTRAN rejects the individuals with too high skew angles for the mesh. If the design of experiment sample space would be defined such that the spars would require a space between neighbouring spars of at least 0.1 percentage of chord, the number of failed individuals could likely be decreased. Locating the spars this close to one another is not realistic from a manufacturing perspective either, verifying this adjustment. With this change, a success rate of more than 90% is expected.

The other reason for performing a design of experiments was to look for trends in layout design that lead to efficient structures. A full overview of the results can be found in Appendix Appendix E. Notice that some individuals that are similar to other individuals are removed in this graph for clarity. To truly find the trends in the structural layout, the lightest five individuals and the heaviest five individuals are compared in Figure 5.14. To better compare the trend of the lighter versus the heavier structures, in Figure 5.15, the average of the five lightest and five heaviest is plotted. The results of the design of experiments clearly show some trends that indicate an efficient design. Moreover, some variables show to have no significant influence on the overall weight.

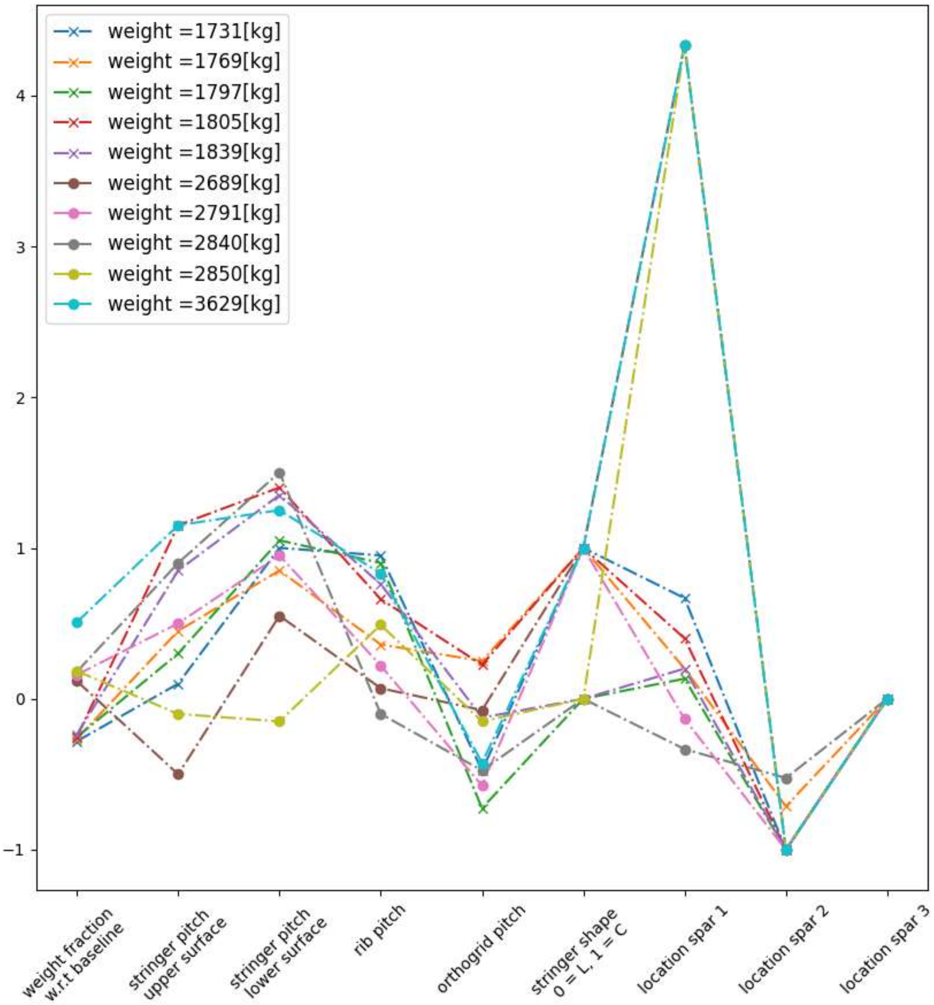

Figure 5.14: Plot showing the structural weight and layout parameters of the 5 layouts that resulted in the lowest structural weight and the 5 layouts that resulted in the highest structural weight, as a result of the design of experiments. The weight is indicated as a percentage of the baseline design weight. The stringer pitches, rib pitch, and orthogrid pitch are given in percentage w.r.t the baseline value. The stringer shape is indicated in binary. A value of zero indicates an L-shaped stringer, a value of one indicates a C-shaped stringer is used. The location of the spar is given as a percentage w.r.t the baseline value, zero indicates no spar is present.

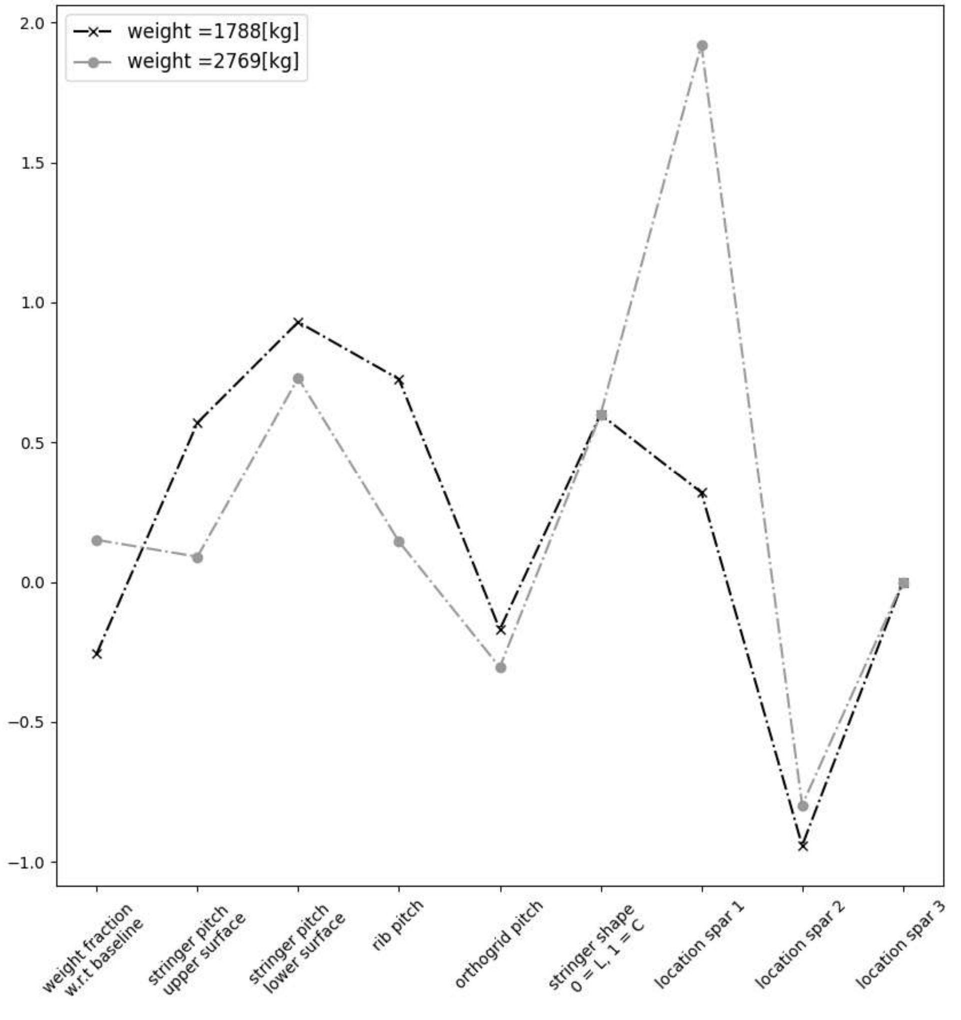

Figure 5.15: Plot showing the structural weight and layout parameters of the average of the 5 layouts that resulted in the lowest structural weight and the average of the 5 layouts that resulted in the highest structural weight, as a result of the design of experiments. The weight is indicated as a percentage of the baseline design weight. The stringer pitches, rib pitch, and orthogrid pitch are given in percentage w.r.t the baseline value. The stringer shape is indicated in binary. A value of zero indicates an L-shaped stringer, a value of one indicates a C-shaped stringer is used. The location of the spar is given as a percentage w.r.t the baseline value, zero indicates no spar is present.

The efficient layouts have a higher value for stringer pitch compared to the base line. This reduces the number of stringers. The stringers can thus be sized more efficiently if the total number of stringers is lower, and the stringer pitch is larger. This result is in line with the expectations, as from the baseline design it can be seen that some of the stringers are sized to the minimum gage size. It should be pointed out that these results are again based upon a stress and fatigue analysis only, buckling is not taken into account. A higher number of stringers might be required for buckling. Both the light and heavier structures have a slightly higher value for stringer pitch for the lower surface as compared to the upper surface. As both are higher, no conclusion can be made.

Interestingly, a higher rib pitch leads to a lighter structure. A lower number of ribs, and thus a lower number of design variables, leads to a lower structural weight. As the number of design variables and the number of ribs is directly related, one cannot draw a conclusion on whether this is caused by the reduction of design variables or by the reduced number of ribs. A lower number of ribs might reduce some stresses introduced into the structure due to constraints on the DOFs at the rib location. Furthermore, the optimization might be more efficient if there are less design variables, however, this seems unlikely for the algorithm that is used by SOL200 optimization.

The rib pitch does not seem to have a direct correlation to the final weight of the structure. This is interesting as the rib pitch does determine the total number of design variables. This indicates a robust design problem. Moreover, the shape of the stringer does also not seem to have a direct correlation with the weight estimate. The pitch of the orthogrid does not have a direct correlation either. This orthogrid pitch is most likely a variable that will be sized by buckling. With a change in stringer size, an efficient design can be reached in dependently of the stringer pitch.

The orthogrid pitch does not seem to have a direct correlation to the final weight of the structure, as the value for the lightest and heaviest designs are close to equal. This is in line with expectations, as the orthogrid is added to prevent buckling and this parameter should be sized by buckling. The optimizer shows to be just as efficient for all orthogrid pitches. The stringer shape does not seem to have an influence on the structural efficiency either. Meaning that the structure can be designed just as efficient with either of the stringer shapes.

The location of the spars shows to be one of the main drivers for structural efficiency. The design of experiments shows that it is more efficient to have a spar located at about quarter chord. This can be explained as the centre of lift acts is assumed to act at quarter chord of the wing. The loads are thus applied at this location, making it an efficient location for a spar. The further away the spar is located from the quarter chord, the less efficient the spar looks to be. Moreover, it seems like a one spar configuration is the most efficient. All light designs resulting from the design of experiments, that have 2 or more spars, have the spars all located close to the quarter chord of the wing.

From a pure structural design perspective, it can thus be concluded that the most efficient design for the outer wing of the Flying-V makes use of one spar only, located at quarter chord and has a stringer pitch of around 0.35 [m]. The outer wing structure can potentially be up to 25% lighter than the proposed baseline structure, mainly through changing the location of the spars.

5.5. Weight Estimate

The framework estimates the structural weight of one outer wing of the Flying-V to be $2400[kg]$. Now, to convert this FEA weight into the actual engineered weight of the wing, a factor must be included to account for the weight of the bonding mechanism. With the use of composite materials, the weight of bonding mechanism, is expected to be little, especially considering the weight savings that are likely possible to achieve with the use of composites. Moreover, the weight can be lowered if a more precise manufacturing method is chosen, decreasing the stress concentration factor, and reducing the weight. The weight increase due to buckling requirements is estimated to be 25%. Moreover, the weight of the ribs needs to be added, it is estimated to be accounted for in the 25% weight increase. This leads to a structural weight estimate of one of the Flying-V outer wings of $3.0 * 10^3 [kg]$. The NLES design is estimated at $3.5 * 10^3 [kg]$. For both outer wings this is $6.0 * 10^3$ for baseline LES design and $7.0 * 10^3$ for NLES design. This resulting weight estimate is close to the estimate of EMWET Oosterom at $6.6 * 10^3 [kg]$ [25] and the estimate from Claeys at $7304[kg]$ [7]. The weight estimated in this thesis is thus 20% lower than the outer wing weight of Claeys. Claeys outer wing weight is based on the weight of the wing skin and stringers only and the weight of the ribs and the spars is not taken into account. However, a lower weight estimate compared to Claeys estimate is not unexpected. Taking a closer look at the structural design of the outer wing used in Claeys model, see Figure 1.7, it is not unlikely to assume that the proposed structure is more efficient, as a major jump in thickness from the wing kink is prevented, the cross-sectional area is higher, and the distribution of the structural elements is more gradual. The differences in the structural model can be seen in Figure 5.16 and Figure 5.17.

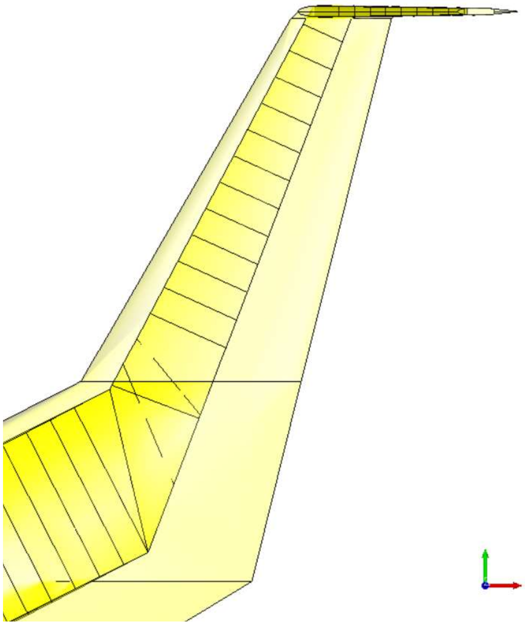

Figure 5.16: Top view of structure of the outer wing of Flying-V, as generated with the previous framework developed by Van der Schaft [32] and Claeys [7].

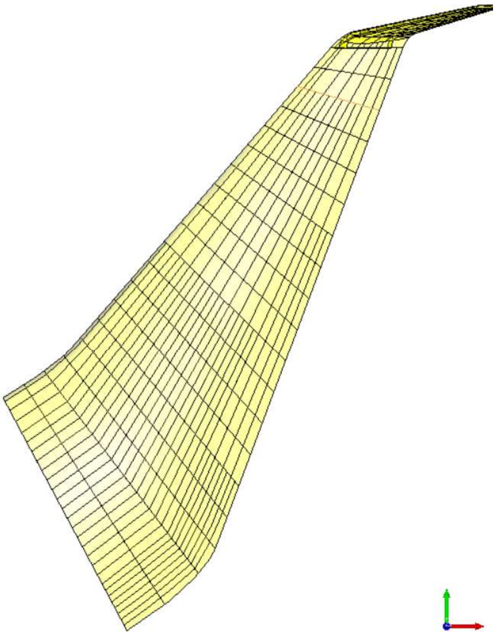

Figure 5.17: Top view of the structure of the outer wing of the Flying-V, as generated with the framework developed in this thesis.

6

Conclusions & Recommendations

6.1. Conclusions

The goal of this study was to estimate the structural weight distribution of the outer wing of a Flying-V aircraft by developing a fully parametric framework, which is compatible with the latest concept developments and allows for expansion into a full Flying-V aircraft. As a result, a fully automatic parametric structure generation, analysis, and sizing framework was developed. The developed framework proved to be an effective means for feasibility studies and sensitive weight estimations early in the concept development phase. The framework makes extensive use of the advantages of KBE and OOP and combines the functionalities of ParaPy and NASTRAN, all contributing to a flexible yet robust weight estimation tool. A newly developed structure generation tool is used to create a structure based on rules defined in a knowledge based. This structure is automatically transformed to a Finite Element Model and a NASTRAN input file is created. The NASTRAN SOL200 optimization algorithm is used to size the structure and give an optimized weight estimate.

By careful selection of dynamic and static parameters of the structural design, a wide range of structures can be evaluated with minimal risks of invalid designs. A design of experiments shows a success rate of 90% for automatic generation and analysis of outer wing structure concepts based solely on the outer shape and the knowledge-base. Different non-conventional concepts can easily be compared, and with the novel structure generation tool, the No Leading Edge Spar concept are included as well. Making the framework compatible with the latest concept developments.

A limitation to the current framework is that the sizing of the structure is performed based on static yield strength and fatigue criterion only, as the buckling analysis of NASTRAN showed to be too computationally heavy for direct implementation into the framework. However, the framework does allow for expansion to the evaluation of the full Flying-V concept. Moreover, the framework only uses ParaPy and NASTRAN, both commercially available software, making the method more generally applicable. Furthermore, the framework shows potential to be useful for other concept evaluations as well, due to the parametric nature of the framework and the rule-based structure generation requiring only the outer shape as input. And as the post-processing is also done in ParaPy, seamless integration with the already developed multidisciplinary design tools, for the Flying-V, is possible by feeding back the weight estimates and design variables. This opens possibilities for future research into stability, aeroelasticity and servo-aeroelasticity, all essential steps towards full proof of the concept of the Flying-V.

The outer wing structure of the Flying is used to showcase the capabilities and flexibility of the analysis tool. The outer wing showed to be feasible, even if use is made of the NLES and no leading-edge spar is present in the outer wing. The greatest skin thickness is achieved in the connection structure from wing to winglet. The NLES is 15% heavier compared to the conventional baseline design. In the outer wing of the aircraft, a clear load path can be identified running along the leading edge. And implementation of a flap is expected to make the structure more efficient and to reduce the weight of the structure up to 20% compared to the baseline design. Fatigue proved to be the critical failure mode, and if the stress concentration factor can be reduced, a weight saving up to 30% can potentially be achieved.

A design of experiments shows the structural most efficient designs have a spar located at the aerodynamic centre and lack a trailing edge spar. The most efficient design, which places the spar at the aerodynamic centre, is estimated to be up to 25% lighter compared to the baseline design. The FEM weight of the baseline design is $2400[kg]$, such that the final, engineering weight of one outer wing is estimated at $3.0 \cdot 10^3[kg]$, when including weight penalties for buckling and manufacturing as well. This is 20% lower than the weight as estimated by previous work of Claeys which already indicated a potential reduction in the total structural weight up to 15% compared to conventional reference aircraft. With the new weight estimate and the new insights into ways to reduce the structural weight of the outer wing, an even more efficient structure for the Flying-V could be possible. These results are promising and hopefully bring the novel Flying-V concept closer to becoming the solution to the need for more efficient and environmentally friendly aircraft.

6.2. Recommendations

No satisfactory results on the sizing of the entire Flying-V concept are generated yet, so it is suggested that future research investigates the expansion of the framework and application to the entire Flying-V structure. A trade-off between the NLES and the LES design can be made when the structural weight estimates on the fuselage design are known as well. The high computational costs required for buckling analysis are another limitation to the current framework. Future work could include application of the analytical approach to sizing for buckling. Moreover, a thorough load analysis should be performed to validate the load cases used for sizing of the structure.

Additionally, there are many possibilities for expanding this framework, due to the parametric nature, of the framework. This could include the use of different materials including composite materials, local topology optimization, integration of high-fidelity aerodynamics for loads and aeroelastic analysis, or a full optimization loop with an optimization algorithm used for structure generation. A cost estimation tool could be implemented as well to make for a more complete optimization. Including all recommendations, the framework has the potential to become a versatile sizing and optimization tool for the Flying-V and other (un)conventional aircraft.

A

Code Documentation

In this appendix, a concise UML Diagram is presented in the first section, followed by the activity diagrams from the structure generation.

A.1. UML Diagram

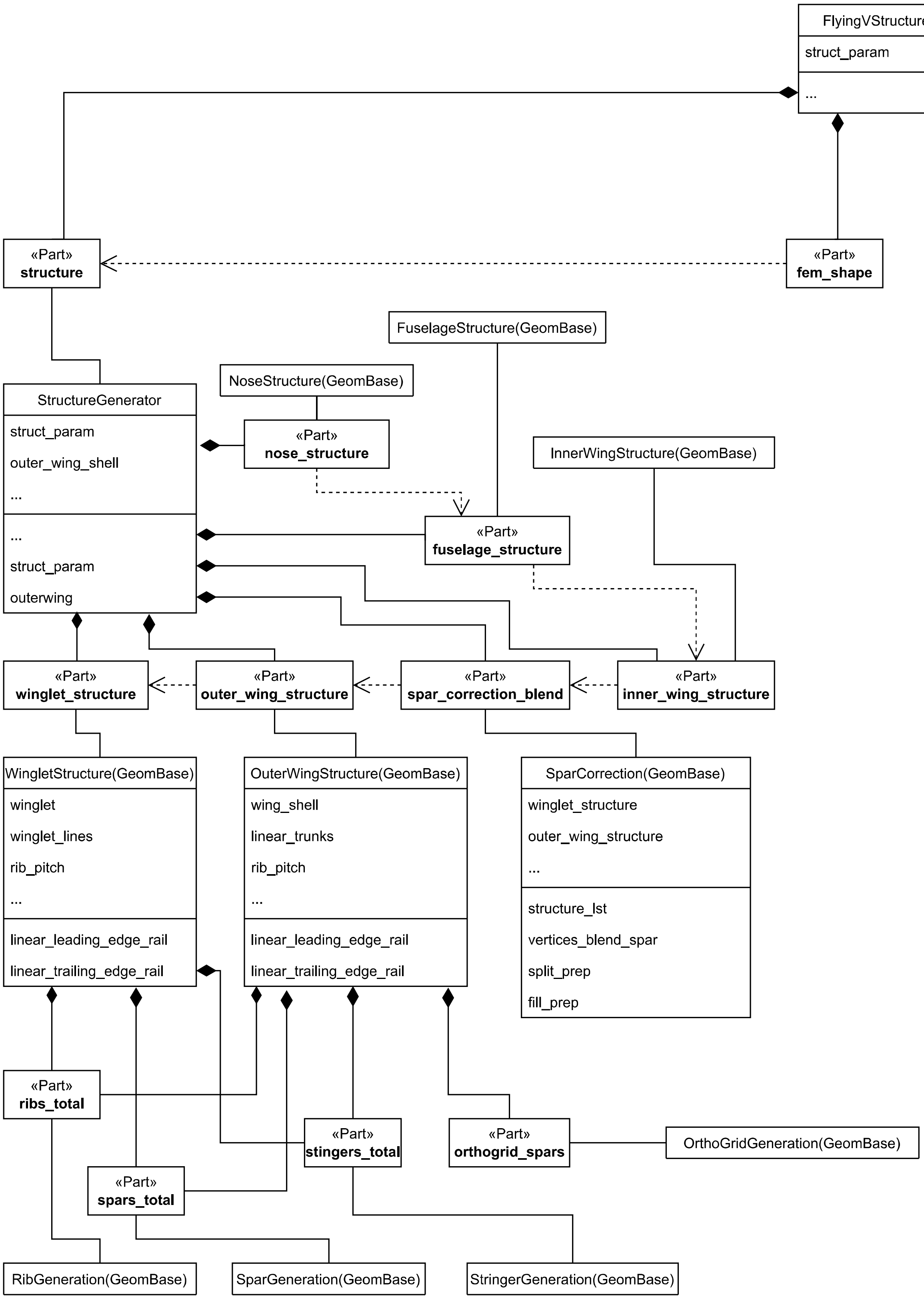

Figure A.1: Part one of the UML Class Diagram of the Framework developed in this study.

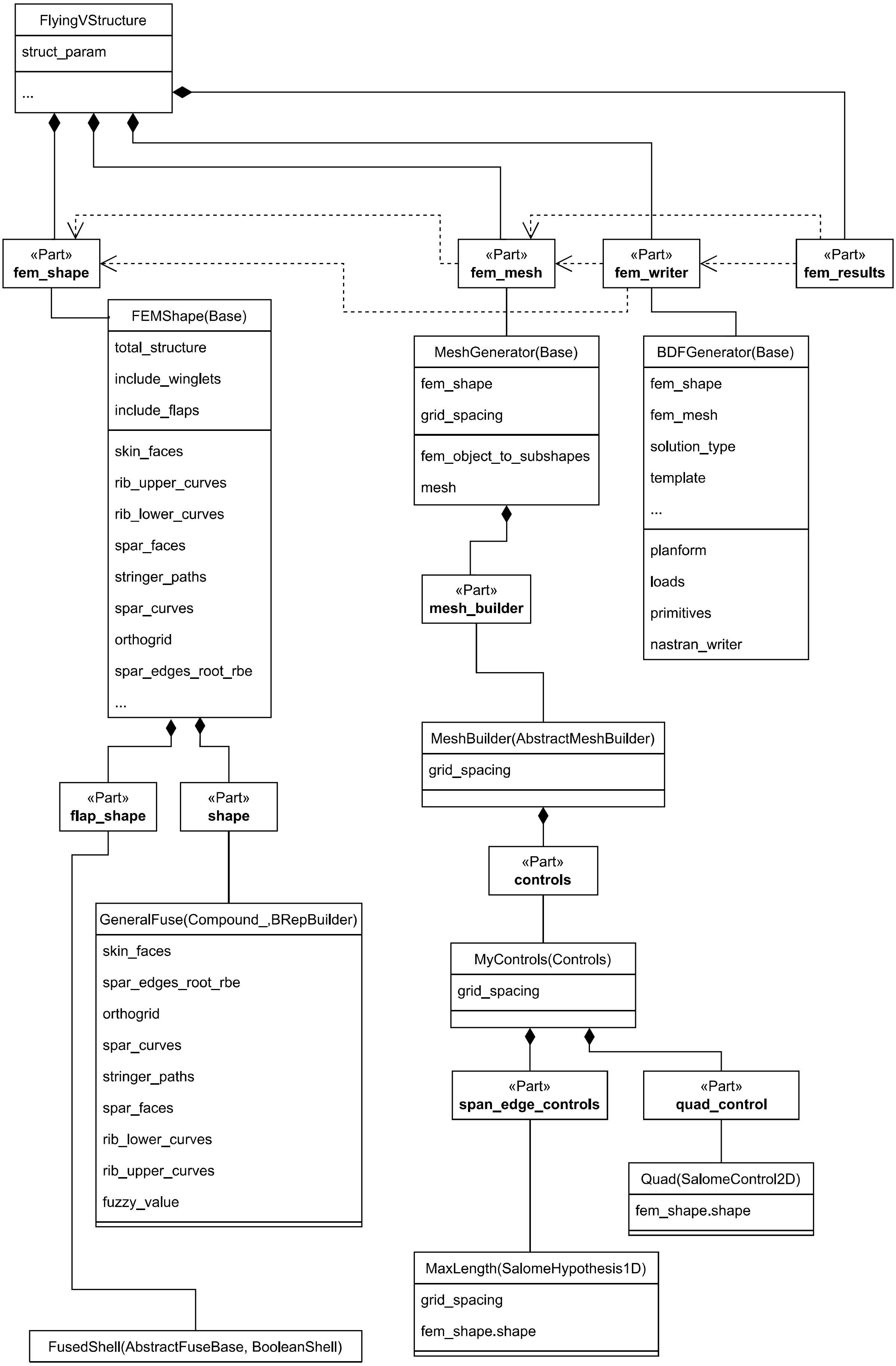

Figure A.2: Part two of the UML Class Diagram of the Framework developed in this study.

A.2. Activity Diagrams

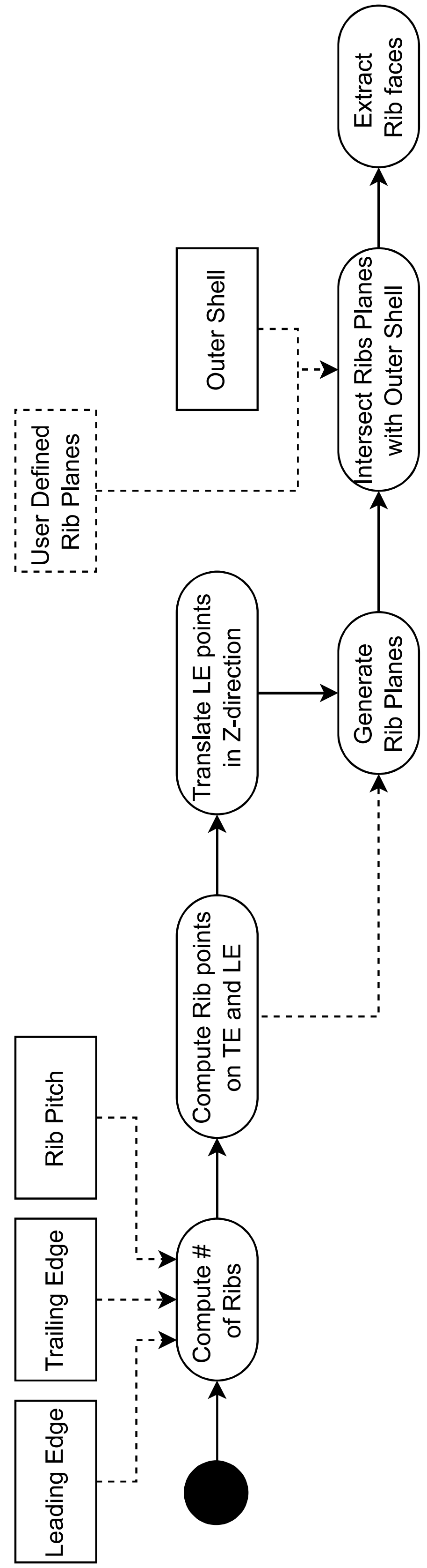

Figure A.3: Activity Diagram showing the rib generation.

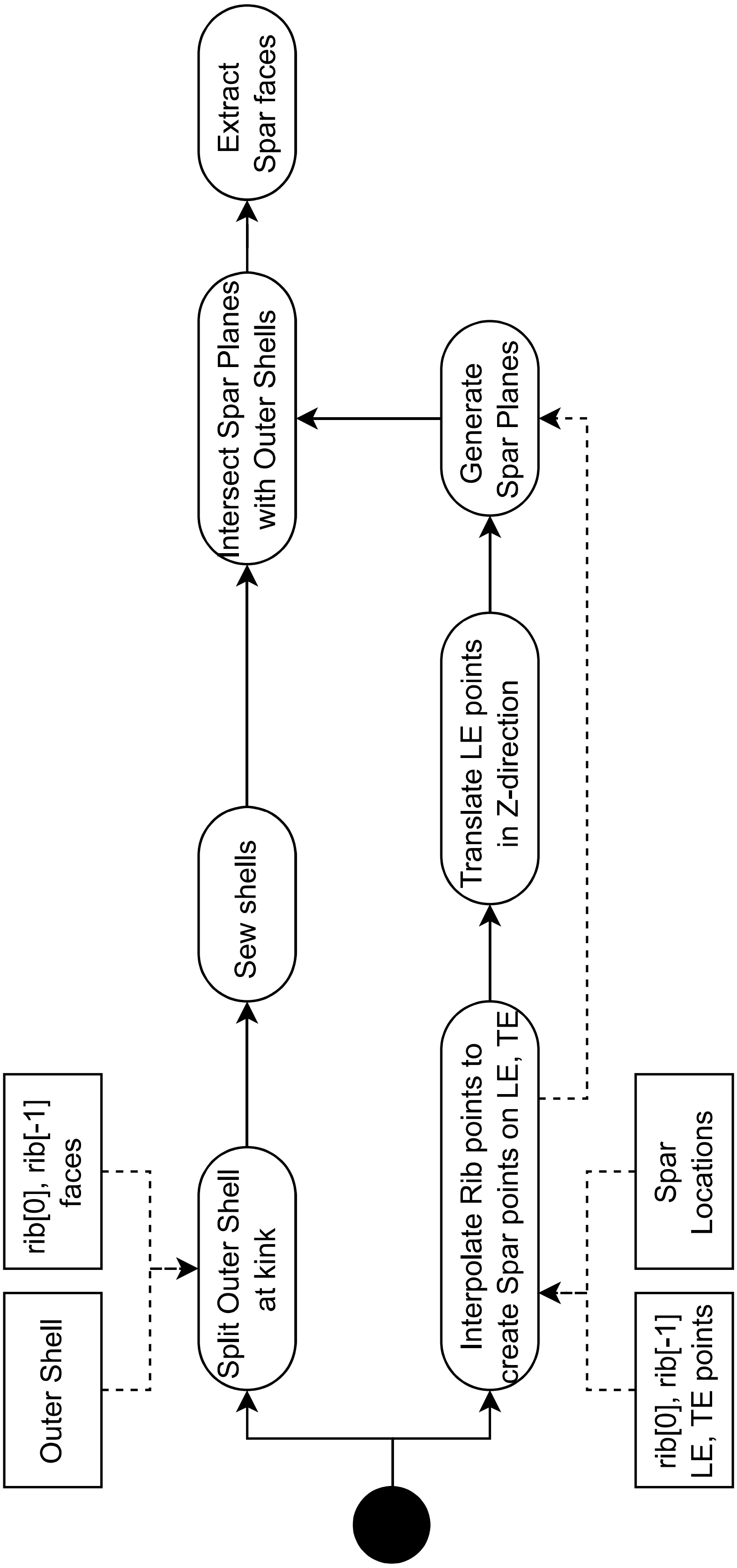

Figure A.4: Activity Diagram showing the spar generation.

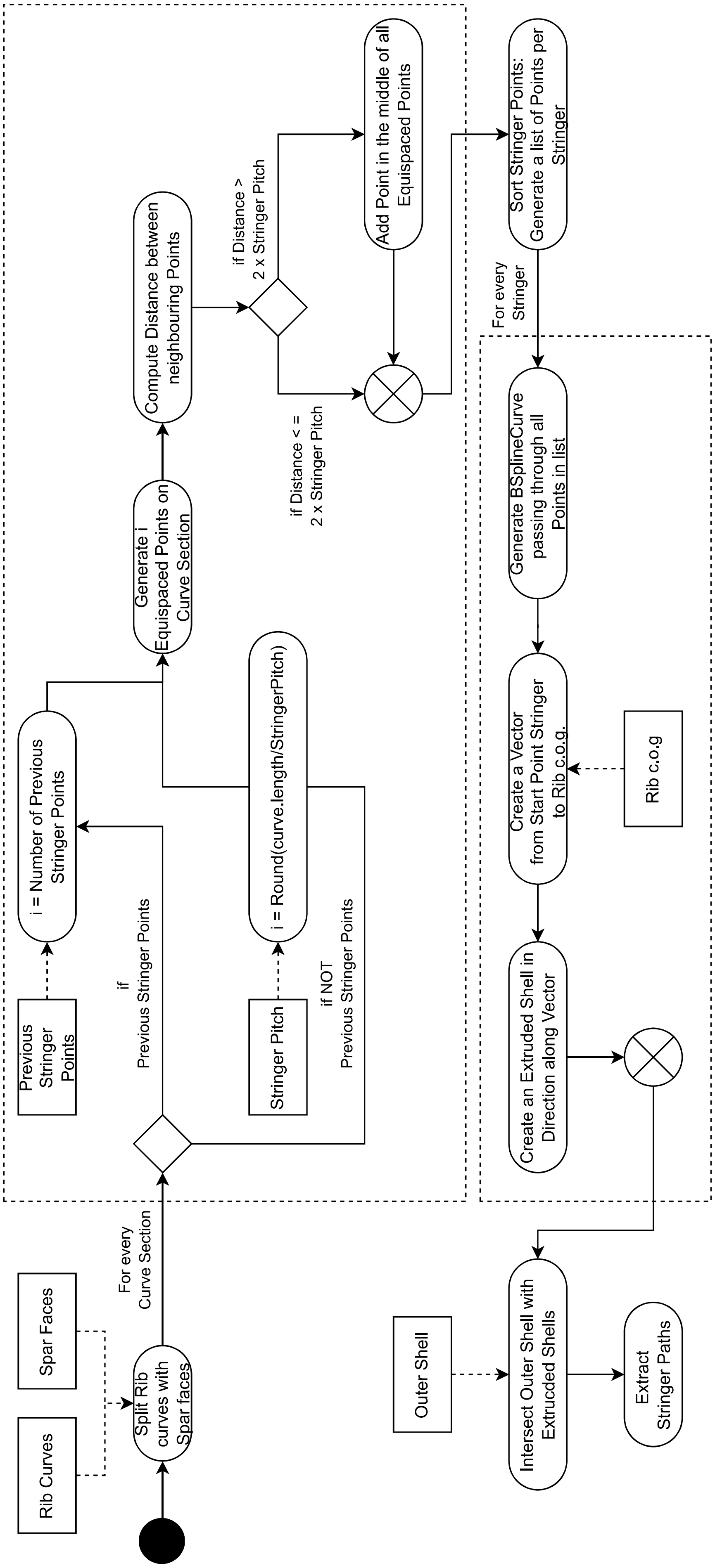

Figure A.5: Activity Diagram showing the stringer generation.

B

Additional Verification Results

B.1. Modal Analysis Results

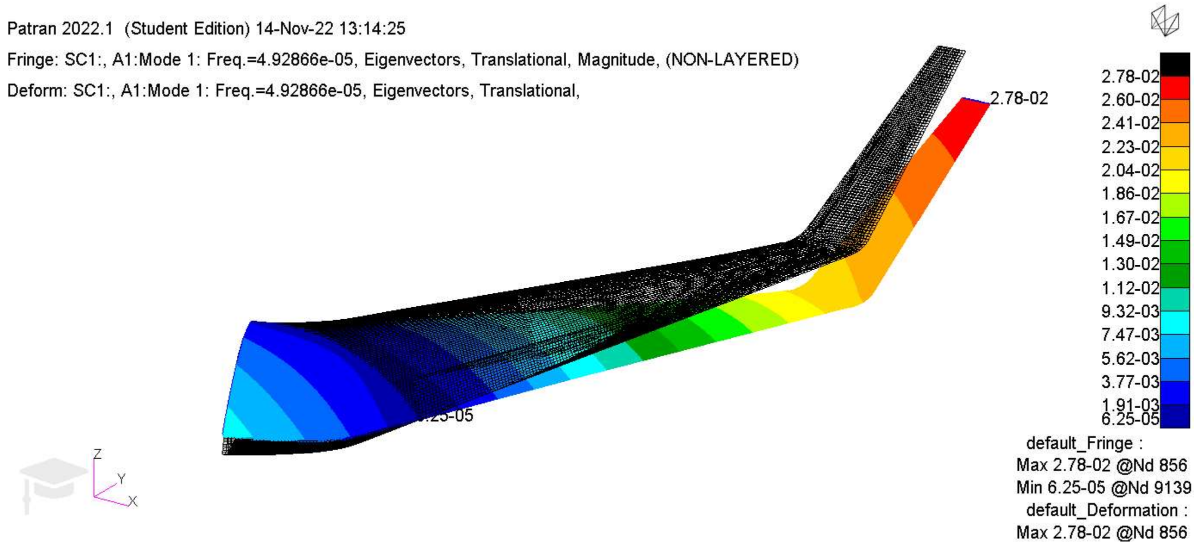

Figure B.1: First eigenmode of the baseline structure of the Flying V outer-wing. Deformation at frequency = 4.928E-05.

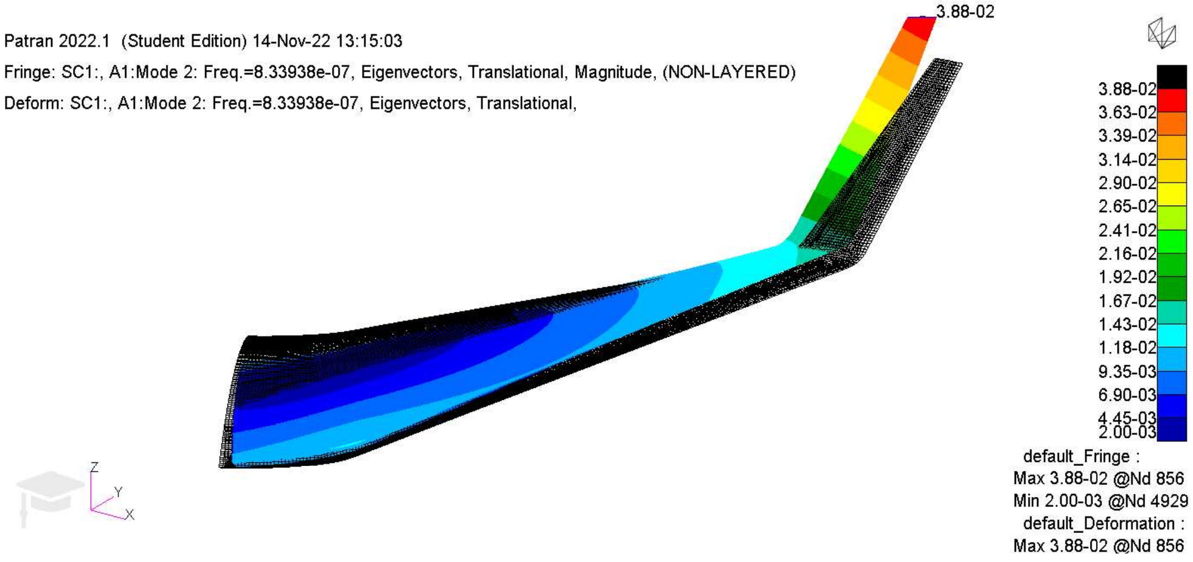

Figure B.2: Section eigenmode of the baseline structure of the Flying V outer-wing. Deformation at frequency = 8.339E-07.

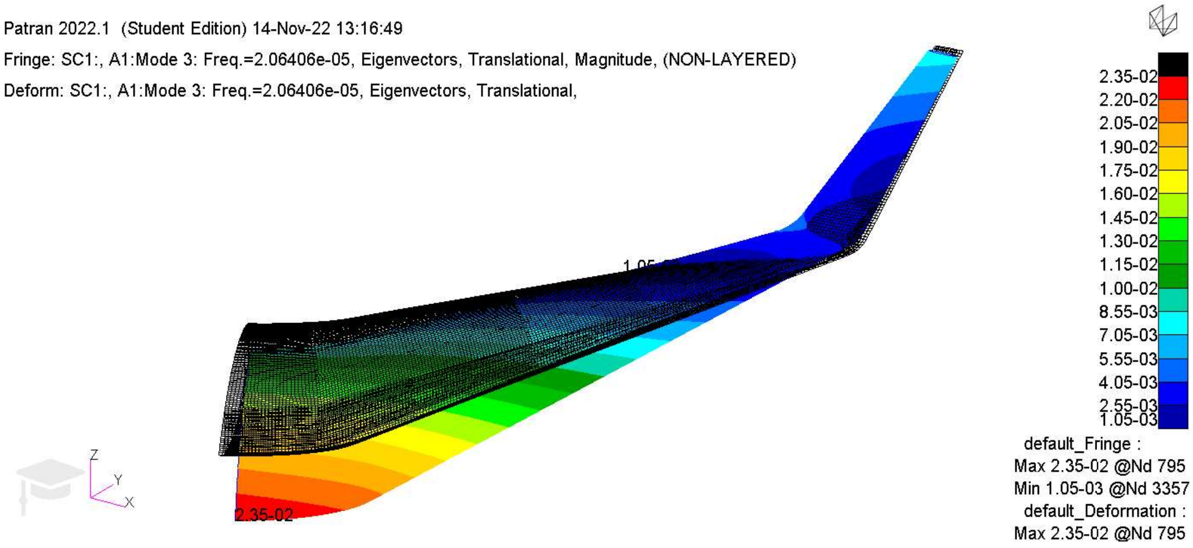

Figure B.3: Third eigenmdoe of the baseline structure of the Flying V.Deformation at frequency = 2.064-05.

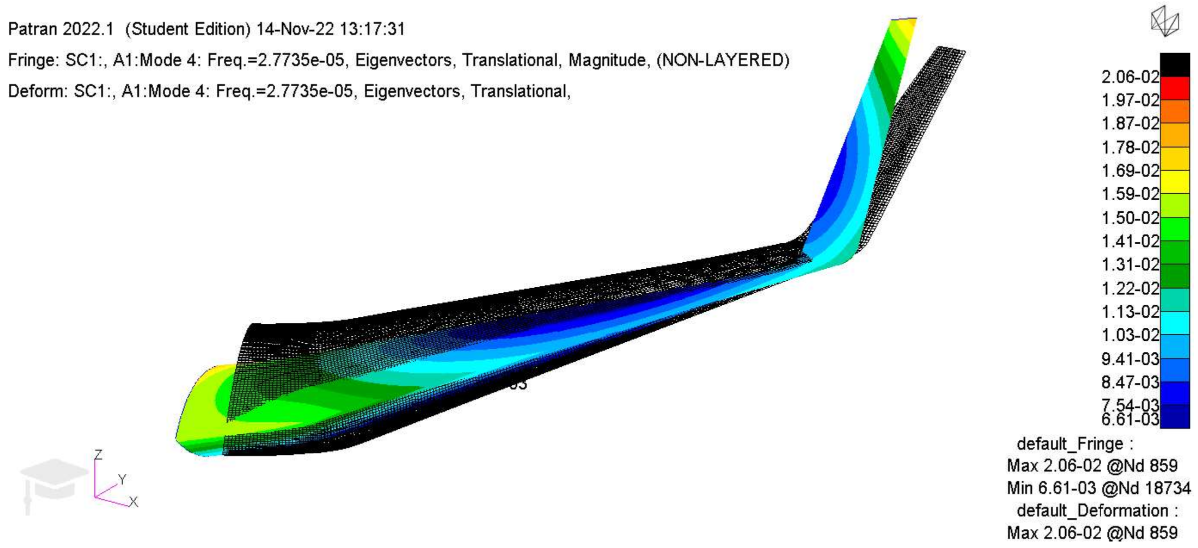

Figure B.4: Fourth eigenmode of the baseline structure of the Flying V outer-wing. Deformation at frequency = 2.773-05.

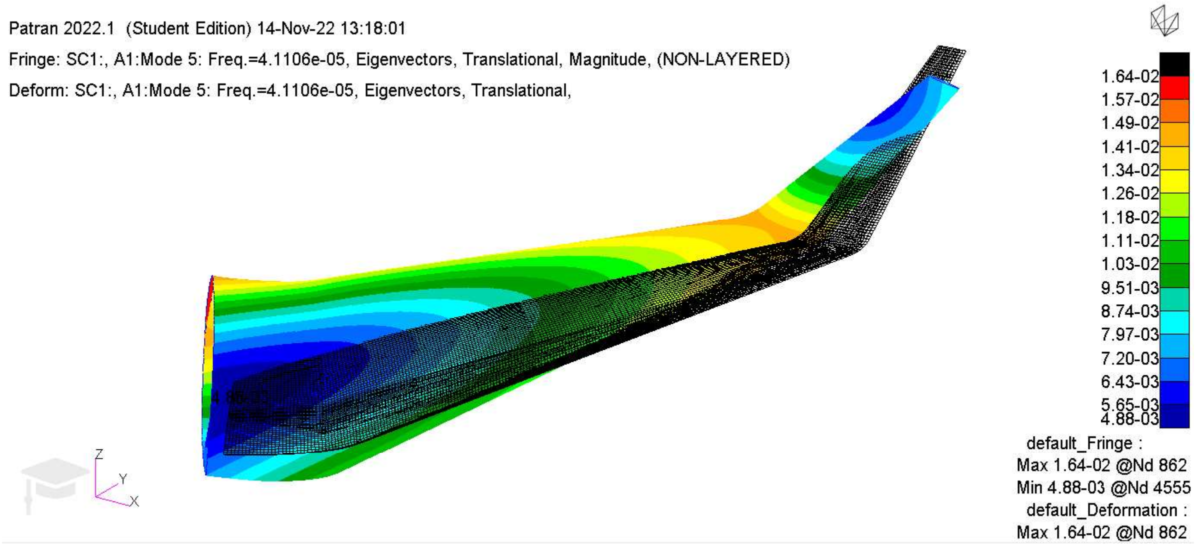

Figure B.5: Fifth eigenmdoe of the baseline structure of the Flying V. Deformation at frequency = 4.110E-05.

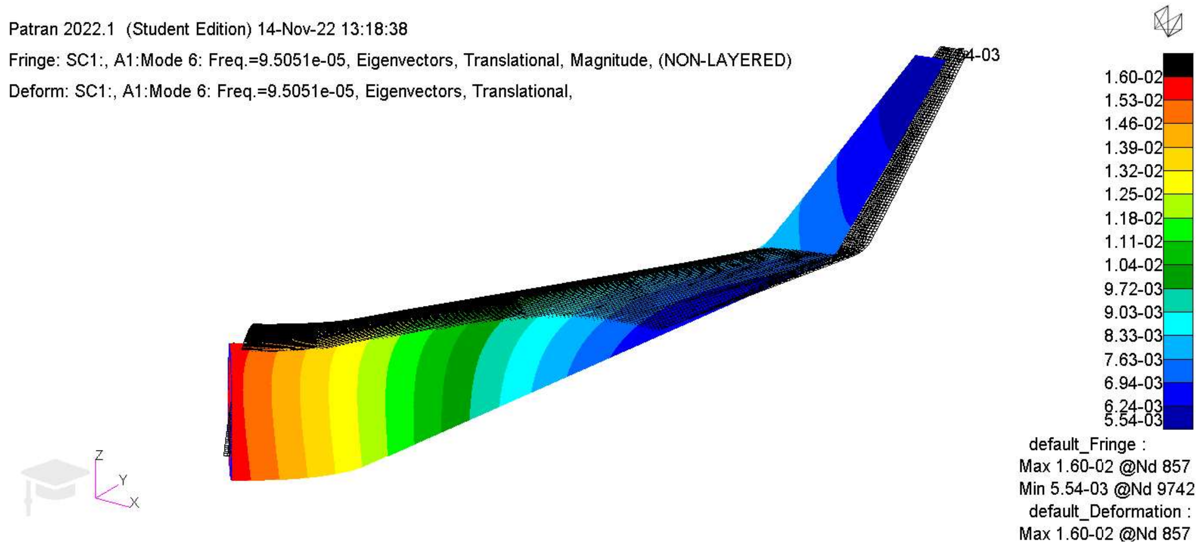

Figure B.6: Sixth eigenmode of the baseline structure of the Flying V outer-wing. Deformation at frequency = 9.505E-05.

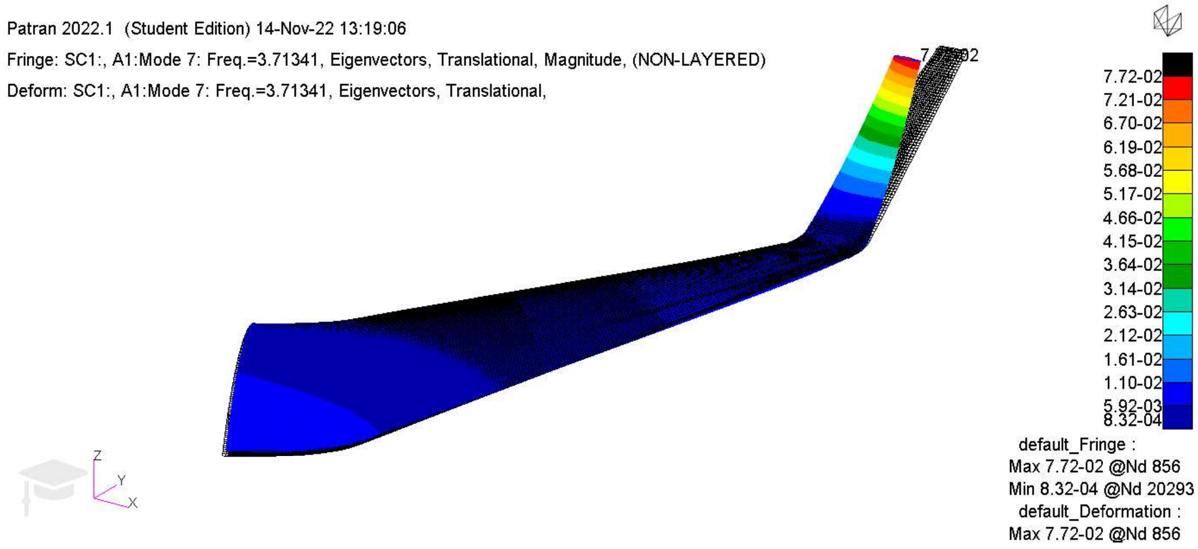

Figure B.7: Seventh eigenmode of the baseline structure of the Flying V. Deformation at frequency = 3.713

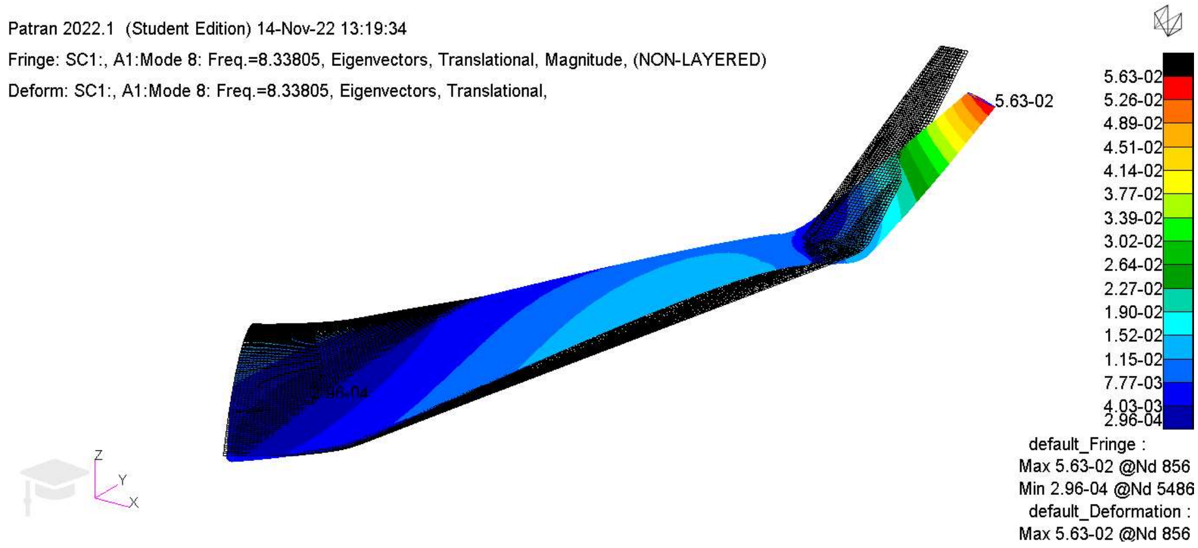

Figure B.8: Eighth eigenmode of the baseline structure of the Flying V outer-wing. Deformation at frequency = 8.338.

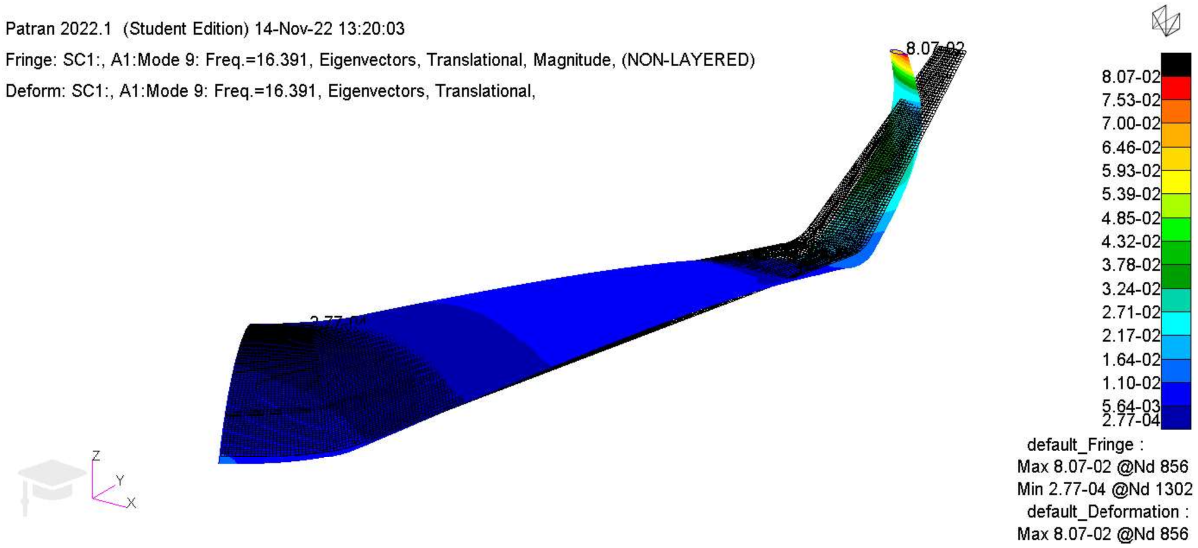

Figure B.9: Ninth eigenmdoe of the baseline structure of the Flying V. Deformation at frequency = 16.391.

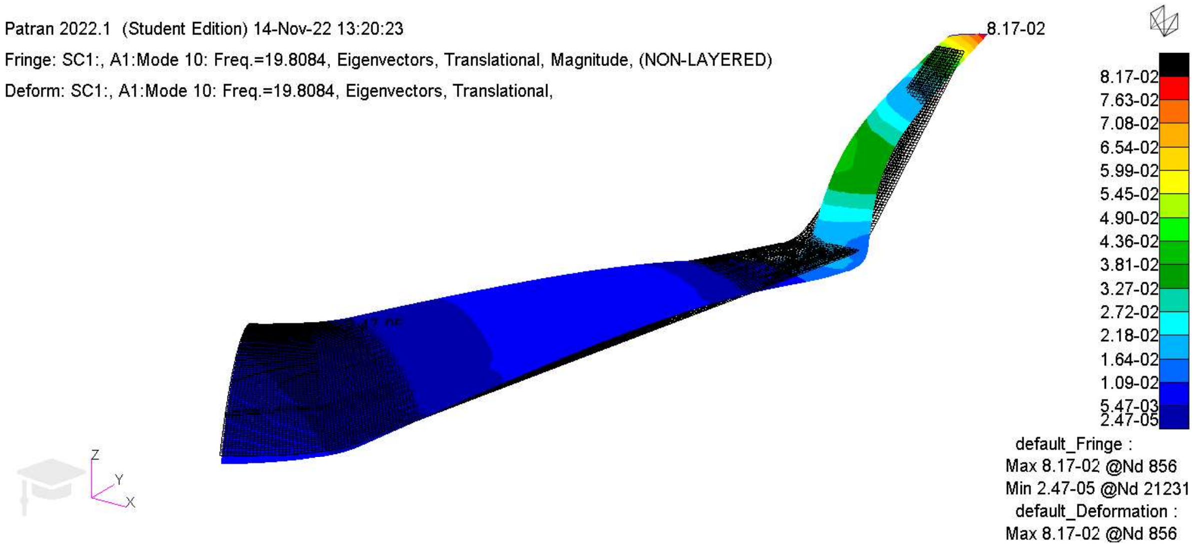

Figure B.10: Tenth eigenmode of the baseline structure of the Flying V outer-wing. Deformation at frequency = 19.6064.

B.2. NASTRAN Example - Numerical Results

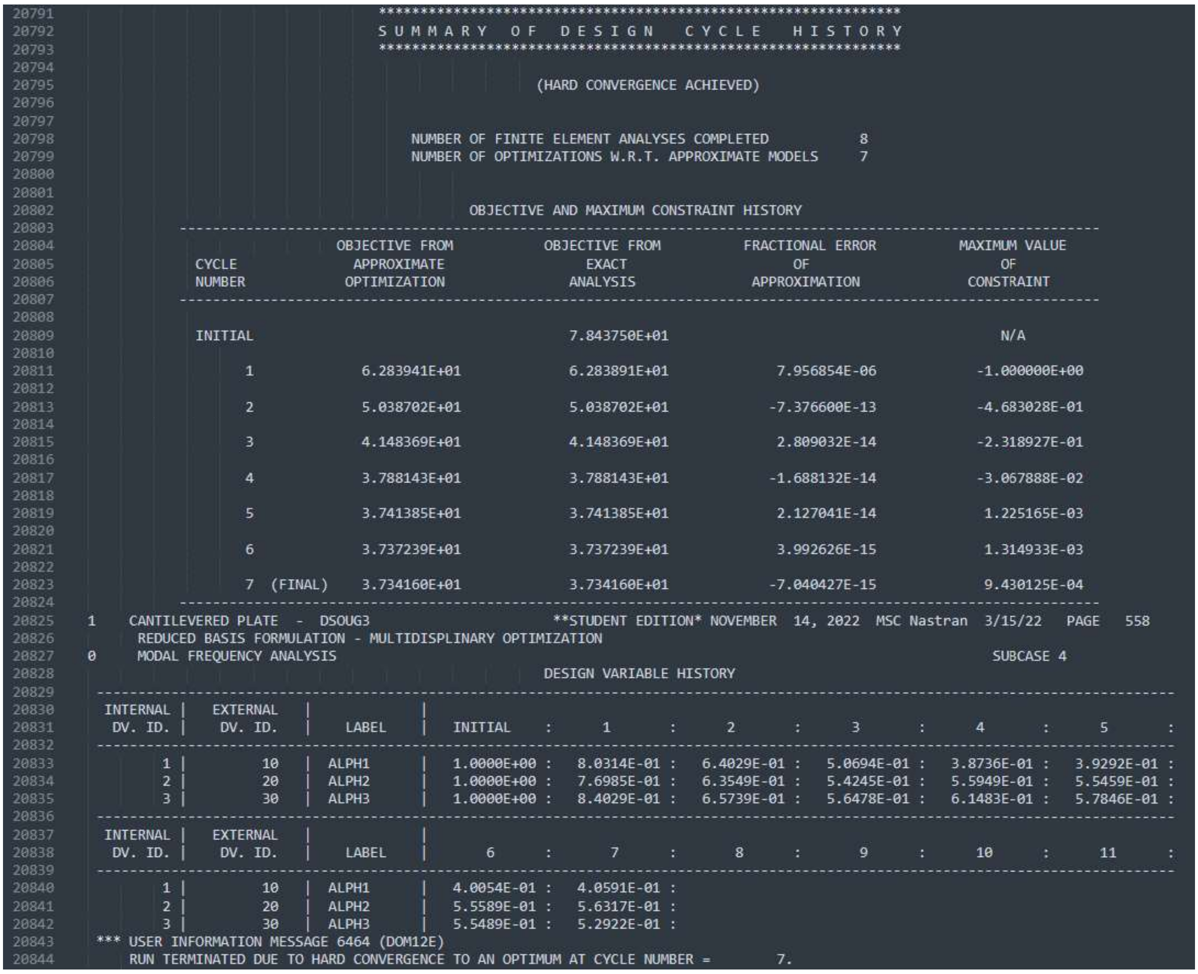
```
                                   **************************************************************
                                   S U M M A R Y    O F    D E S I G N    C Y C L E    H I S T O R Y
                                   **************************************************************

                                                      (HARD CONVERGENCE ACHIEVED)


                                       NUMBER OF FINITE ELEMENT ANALYSES COMPLETED          8
                                       NUMBER OF OPTIMIZATIONS W.R.T. APPROXIMATE MODELS    7


                                              OBJECTIVE AND MAXIMUM CONSTRAINT HISTORY
           ---------------------------------------------------------------------------------------------------------------
                            OBJECTIVE FROM          OBJECTIVE FROM          FRACTIONAL ERROR          MAXIMUM VALUE
             CYCLE           APPROXIMATE                EXACT                      OF                      OF
             NUMBER          OPTIMIZATION              ANALYSIS              APPROXIMATION             CONSTRAINT
           ---------------------------------------------------------------------------------------------------------------

             INITIAL                                7.843750E+01                                           N/A

                   1             6.283941E+01            6.283891E+01             7.956854E-06            -1.000000E+00

                   2             5.038702E+01            5.038702E+01            -7.376600E-13            -4.683028E-01

                   3             4.148369E+01            4.148369E+01             2.809032E-14            -2.318927E-01

                   4             3.788143E+01            3.788143E+01            -1.688132E-14            -3.067888E-02

                   5             3.741385E+01            3.741385E+01             2.127041E-14             1.225165E-03

                   6             3.737239E+01            3.737239E+01             3.992626E-15             1.314933E-03

                   7  (FINAL)    3.734160E+01            3.734160E+01            -7.040427E-15             9.430125E-04
           ---------------------------------------------------------------------------------------------------------------
1    CANTILEVERED PLATE   -  DSOUG3                     **STUDENT EDITION* NOVEMBER  14, 2022  MSC Nastran  3/15/22   PAGE   558
      REDUCED BASIS FORMULATION - MULTIDISPLINARY OPTIMIZATION
0     MODAL FREQUENCY ANALYSIS                                                                                SUBCASE 4
                                                       DESIGN VARIABLE HISTORY
 ---------------------------------------------------------------------------------------------------------------------------------
  INTERNAL |   EXTERNAL   |              |
   DV. ID. |    DV. ID.   |     LABEL    |   INITIAL    :      1       :      2       :      3       :      4       :      5       :
 ---------------------------------------------------------------------------------------------------------------------------------
         1 |         10   |  ALPH1       |   1.0000E+00 :   8.0314E-01 :   6.4029E-01 :   5.0694E-01 :   3.8736E-01 :   3.9292E-01 :
         2 |         20   |  ALPH2       |   1.0000E+00 :   7.6985E-01 :   6.3549E-01 :   5.4245E-01 :   5.5949E-01 :   5.5459E-01 :
         3 |         30   |  ALPH3       |   1.0000E+00 :   8.4029E-01 :   6.5739E-01 :   5.6478E-01 :   6.1483E-01 :   5.7846E-01 :
 ---------------------------------------------------------------------------------------------------------------------------------
  INTERNAL |   EXTERNAL   |              |
   DV. ID. |    DV. ID.   |     LABEL    |      6       :      7       :      8       :      9       :     10       :     11       :
 ---------------------------------------------------------------------------------------------------------------------------------
         1 |         10   |  ALPH1       |   4.0054E-01 :   4.0591E-01 :
         2 |         20   |  ALPH2       |   5.5589E-01 :   5.6317E-01 :
         3 |         30   |  ALPH3       |   5.5489E-01 :   5.2922E-01 :
 *** USER INFORMATION MESSAGE 6464 (DOM12E)
     RUN TERMINATED DUE TO HARD CONVERGENCE TO AN OPTIMUM AT CYCLE NUMBER =        7.
```

Figure B.11: Numerical Results of the NASTRAN Cantilivered Plate problem as analysed with the ParaPy based Framework developed in this research.

B.3. Analytical Validation - Numerical Results

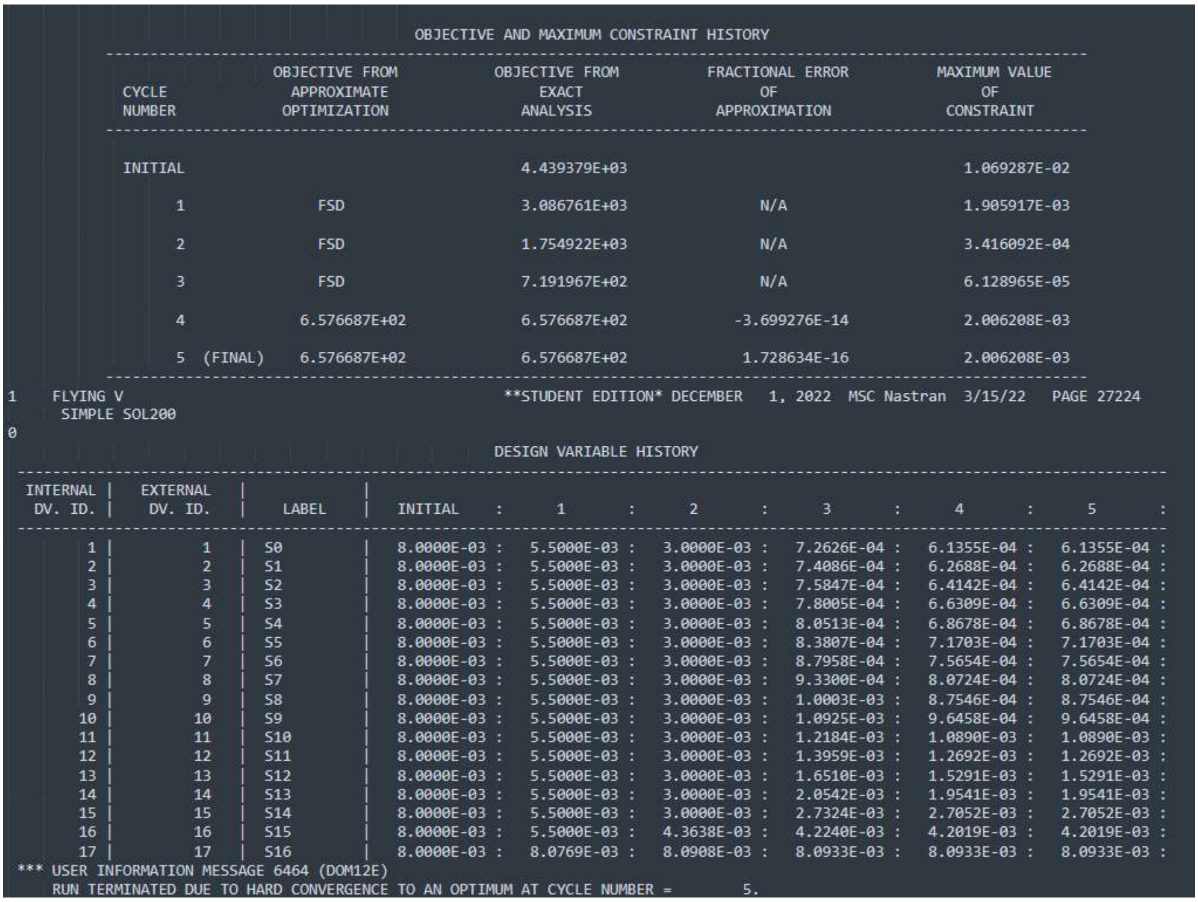

```
                                       OBJECTIVE AND MAXIMUM CONSTRAINT HISTORY
          ---------------------------------------------------------------------------------------------------------
                             OBJECTIVE FROM          OBJECTIVE FROM          FRACTIONAL ERROR         MAXIMUM VALUE
            CYCLE              APPROXIMATE               EXACT                      OF                      OF
            NUMBER            OPTIMIZATION              ANALYSIS              APPROXIMATION             CONSTRAINT
          ---------------------------------------------------------------------------------------------------------

            INITIAL                                   4.439379E+03                                    1.069287E-02

                  1               FSD                 3.086761E+03                 N/A                1.905917E-03

                  2               FSD                 1.754922E+03                 N/A                3.416092E-04

                  3               FSD                 7.191967E+02                 N/A                6.128965E-05

                  4           6.576687E+02            6.576687E+02            -3.699276E-14           2.006208E-03

                  5  (FINAL)  6.576687E+02            6.576687E+02             1.728634E-16           2.006208E-03
          ---------------------------------------------------------------------------------------------------------
1    FLYING V                                   **STUDENT EDITION* DECEMBER   1, 2022  MSC Nastran  3/15/22   PAGE 27224
      SIMPLE SOL200
0
                                                      DESIGN VARIABLE HISTORY
 ------------------------------------------------------------------------------------------------------------------------------
  INTERNAL |   EXTERNAL  |              |
   DV. ID. |    DV. ID.  |    LABEL     |   INITIAL    :      1       :      2       :      3       :      4       :      5       :
 ------------------------------------------------------------------------------------------------------------------------------
         1 |           1 |  S0          |   8.0000E-03 :   5.5000E-03 :   3.0000E-03 :   7.2626E-04 :   6.1355E-04 :   6.1355E-04 :
         2 |           2 |  S1          |   8.0000E-03 :   5.5000E-03 :   3.0000E-03 :   7.4086E-04 :   6.2688E-04 :   6.2688E-04 :
         3 |           3 |  S2          |   8.0000E-03 :   5.5000E-03 :   3.0000E-03 :   7.5847E-04 :   6.4142E-04 :   6.4142E-04 :
         4 |           4 |  S3          |   8.0000E-03 :   5.5000E-03 :   3.0000E-03 :   7.8005E-04 :   6.6309E-04 :   6.6309E-04 :
         5 |           5 |  S4          |   8.0000E-03 :   5.5000E-03 :   3.0000E-03 :   8.0513E-04 :   6.8678E-04 :   6.8678E-04 :
         6 |           6 |  S5          |   8.0000E-03 :   5.5000E-03 :   3.0000E-03 :   8.3807E-04 :   7.1703E-04 :   7.1703E-04 :
         7 |           7 |  S6          |   8.0000E-03 :   5.5000E-03 :   3.0000E-03 :   8.7958E-04 :   7.5654E-04 :   7.5654E-04 :
         8 |           8 |  S7          |   8.0000E-03 :   5.5000E-03 :   3.0000E-03 :   9.3300E-04 :   8.0724E-04 :   8.0724E-04 :
         9 |           9 |  S8          |   8.0000E-03 :   5.5000E-03 :   3.0000E-03 :   1.0003E-03 :   8.7546E-04 :   8.7546E-04 :
        10 |          10 |  S9          |   8.0000E-03 :   5.5000E-03 :   3.0000E-03 :   1.0925E-03 :   9.6458E-04 :   9.6458E-04 :
        11 |          11 |  S10         |   8.0000E-03 :   5.5000E-03 :   3.0000E-03 :   1.2184E-03 :   1.0890E-03 :   1.0890E-03 :
        12 |          12 |  S11         |   8.0000E-03 :   5.5000E-03 :   3.0000E-03 :   1.3959E-03 :   1.2692E-03 :   1.2692E-03 :
        13 |          13 |  S12         |   8.0000E-03 :   5.5000E-03 :   3.0000E-03 :   1.6510E-03 :   1.5291E-03 :   1.5291E-03 :
        14 |          14 |  S13         |   8.0000E-03 :   5.5000E-03 :   3.0000E-03 :   2.0542E-03 :   1.9541E-03 :   1.9541E-03 :
        15 |          15 |  S14         |   8.0000E-03 :   5.5000E-03 :   3.0000E-03 :   2.7324E-03 :   2.7052E-03 :   2.7052E-03 :
        16 |          16 |  S15         |   8.0000E-03 :   5.5000E-03 :   4.3638E-03 :   4.2240E-03 :   4.2019E-03 :   4.2019E-03 :
        17 |          17 |  S16         |   8.0000E-03 :   8.0769E-03 :   8.0908E-03 :   8.0933E-03 :   8.0933E-03 :   8.0933E-03 :
 *** USER INFORMATION MESSAGE 6464 (DOM12E)
     RUN TERMINATED DUE TO HARD CONVERGENCE TO AN OPTIMUM AT CYCLE NUMBER =        5.
```

Figure B.12: Numerical Results of the simplified Flying V outer-wing as analysed with the ParaPy based Framework developed in this research. Bending loads only.

C

BDF Files

In this appendix, first the BDF file setup that is a required input for the framework is shown, followed by the BDF file generated by the framework that NASTRAN uses as input for an analysis.

C.1. BDF Template Input Files

In Figure C.1

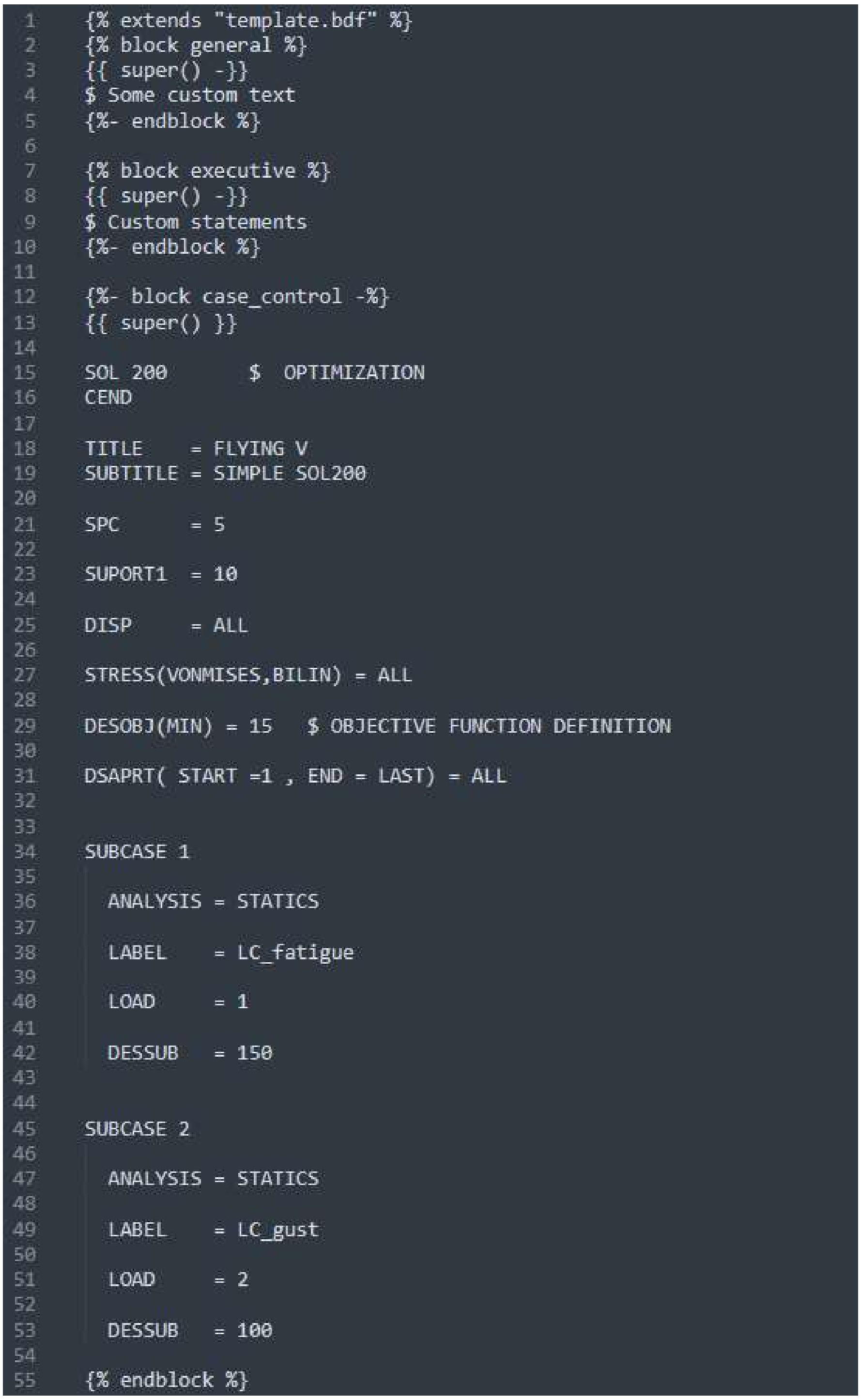

```
{% extends "template.bdf" %}
{% block general %}
{{ super() -}}
$ Some custom text
{%- endblock %}

{% block executive %}
{{ super() -}}
$ Custom statements
{%- endblock %}

{%- block case_control -%}
{{ super() }}

SOL 200       $  OPTIMIZATION
CEND

TITLE    = FLYING V
SUBTITLE = SIMPLE SOL200

SPC      = 5

SUPORT1  = 10

DISP     = ALL

STRESS(VONMISES,BILIN) = ALL

DESOBJ(MIN) = 15   $ OBJECTIVE FUNCTION DEFINITION

DSAPRT( START =1 , END = LAST) = ALL


SUBCASE 1

  ANALYSIS = STATICS

  LABEL    = LC_fatigue

  LOAD     = 1

  DESSUB   = 150


SUBCASE 2

  ANALYSIS = STATICS

  LABEL    = LC_gust

  LOAD     = 2

  DESSUB   = 100

{% endblock %}
```

Figure C.1: BDF Template input file required for the framework to automatically write the full BDF file for NASTRAN. Here, an example of a template for the baseline sol200 analysis is shown.

C.2. Example BDF File

In this section, an example of an automatically generated BDF file is given. This example is based on the BDF file of the baseline analysis, and all duplicate NASTRAN cards are removed. So, for example, only one GRID statement is shown, however the triple dots indicate that more GRID statements are present in the original file. The aim is to show the outline of the BDF files and show how the design problem is defined in the NASTRAN input file. The original BDF file is the input file for NASTRAN, directly leading to an analysis.

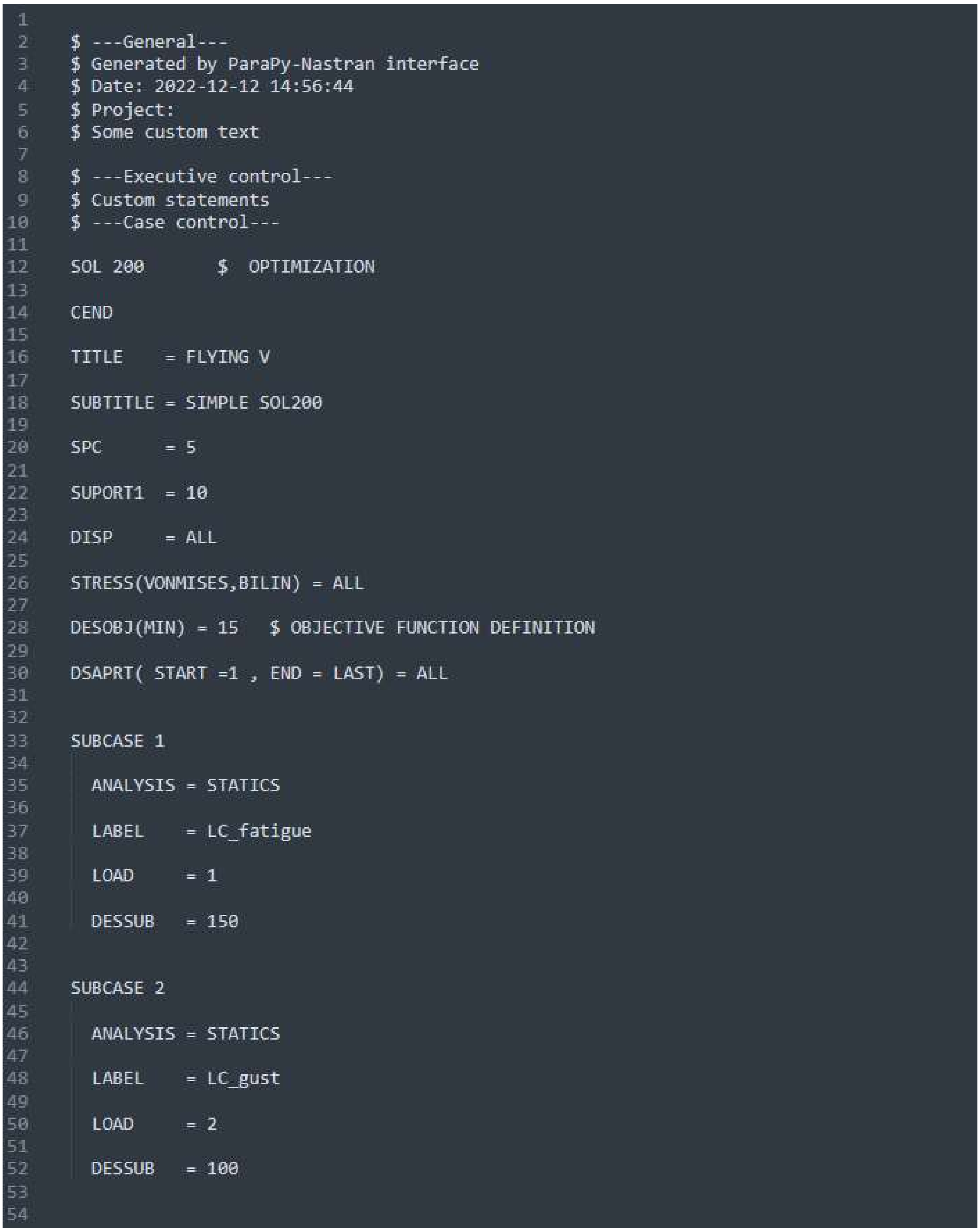

```
$ ---General---
$ Generated by ParaPy-Nastran interface
$ Date: 2022-12-12 14:56:44
$ Project:
$ Some custom text

$ ---Executive control---
$ Custom statements
$ ---Case control---

SOL 200       $  OPTIMIZATION

CEND

TITLE    = FLYING V

SUBTITLE = SIMPLE SOL200

SPC      = 5

SUPORT1  = 10

DISP     = ALL

STRESS(VONMISES,BILIN) = ALL

DESOBJ(MIN) = 15   $ OBJECTIVE FUNCTION DEFINITION

DSAPRT( START =1 , END = LAST) = ALL


SUBCASE 1

  ANALYSIS = STATICS

  LABEL    = LC_fatigue

  LOAD     = 1

  DESSUB   = 150


SUBCASE 2

  ANALYSIS = STATICS

  LABEL    = LC_gust

  LOAD     = 2

  DESSUB   = 100
```

Figure C.2: First part of the BDF file generated by the framework developed in this study. This first part makes extensive use of the Template for the structure and includes the Executive control section and the Case Control section.

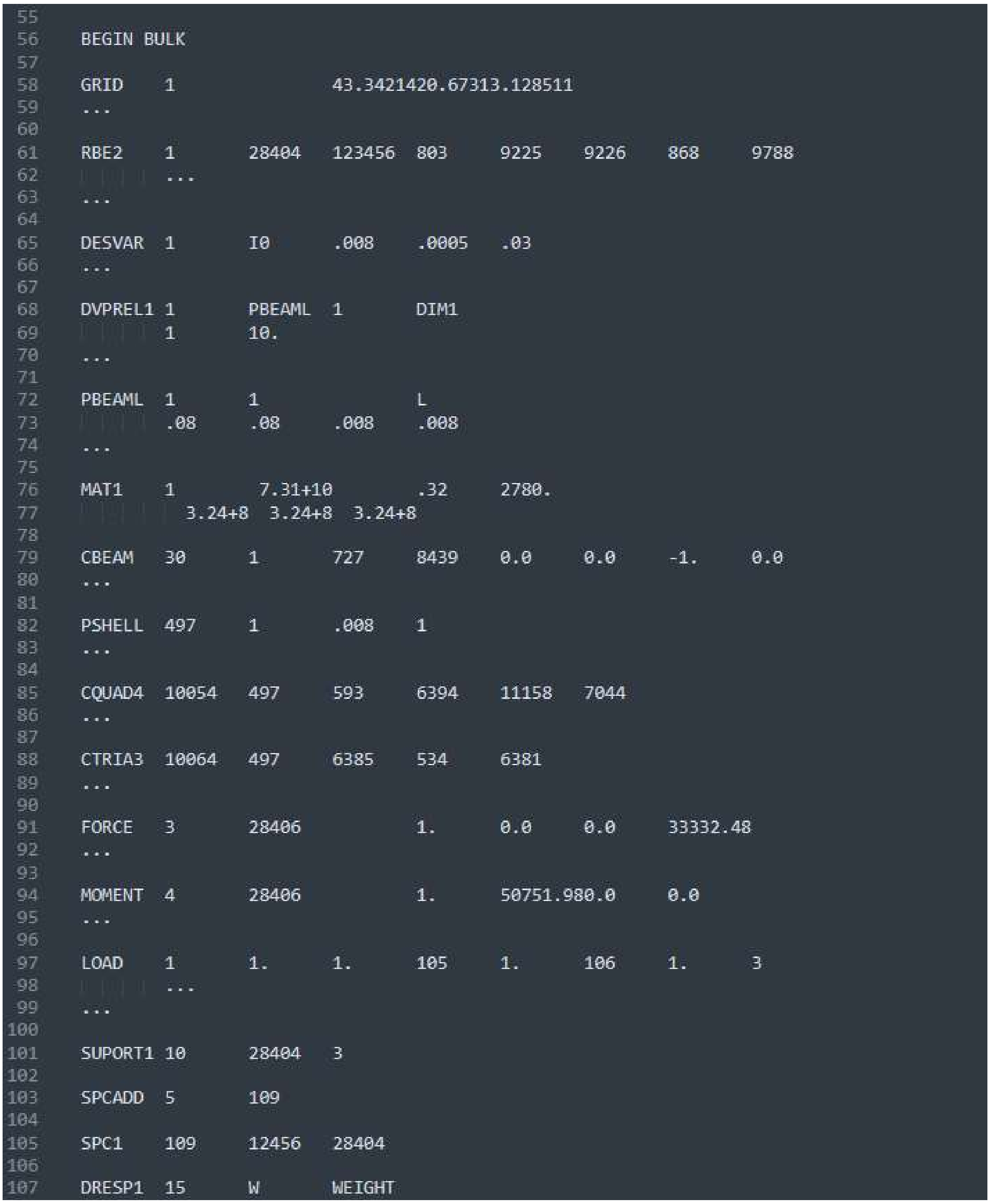

```

BEGIN BULK

GRID    1               43.3421420.67313.128511
...

RBE2    1       28404   123456  803     9225    9226    868     9788
        ...
...

DESVAR  1       I0      .008    .0005   .03
...

DVPREL1 1       PBEAML  1       DIM1
        1       10.
...

PBEAML  1       1               L
        .08     .08     .008    .008
...

MAT1    1        7.31+10        .32     2780.
          3.24+8  3.24+8  3.24+8

CBEAM   30      1       727     8439    0.0     0.0     -1.     0.0
...

PSHELL  497     1       .008    1
...

CQUAD4  10054   497     593     6394    11158   7044
...

CTRIA3  10064   497     6385    534     6381
...

FORCE   3       28406           1.      0.0     0.0     33332.48
...

MOMENT  4       28406           1.      50751.980.0     0.0
...

LOAD    1       1.      1.      105     1.      106     1.      3
        ...
...

SUPORT1 10      28404   3

SPCADD  5       109

SPC1    109     12456   28404

DRESP1  15      W       WEIGHT
```

Figure C.3: Second part of a BDF file generated by the framework developed in this study. The triple dots indicate that the NASTRAN statement on the previous line was repeated multiple times. This part shows the majority of the Bulk Section.

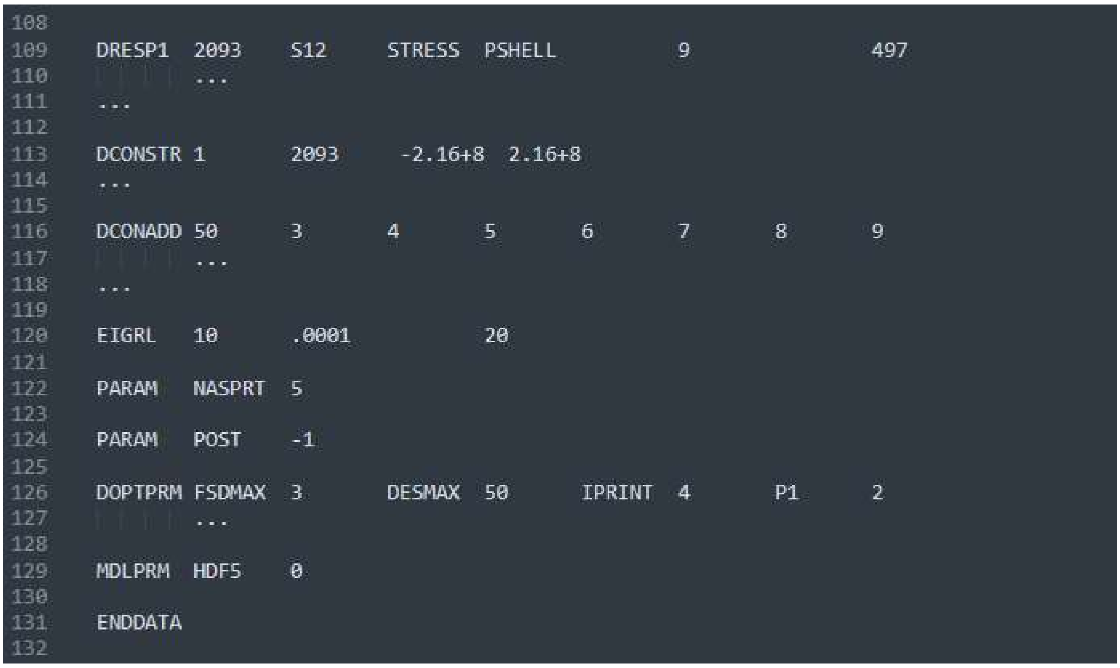

```

DRESP1  2093    S12     STRESS  PSHELL          9               497
        ...
...

DCONSTR 1       2093     -2.16+8  2.16+8
...

DCONADD 50      3       4       5       6       7       8       9
        ...
...

EIGRL   10      .0001           20

PARAM   NASPRT  5

PARAM   POST    -1

DOPTPRM FSDMAX  3       DESMAX  50      IPRINT  4       P1      2
        ...

MDLPRM  HDF5    0

ENDDATA

```

Figure C.4: Final part of a BDF file generated by the framework developed in this study. The triple dots indicate that the NASTRAN statement on the previous line was repeated multiple times. This part show the final part of the Bulk Section.

D

NASTRAN Cards

In this appendix, an overview of the NASTRAN Cards or Statements used in the framework are presented. The basic definition and the format as written by the framework, and required by NASTRAN, is shown. A more elaborate explanation and the definition of all the input parameters can be found in the NASTRAN Quick Reference Guide. The framework is based on the definitions from NASTRAN 2020.

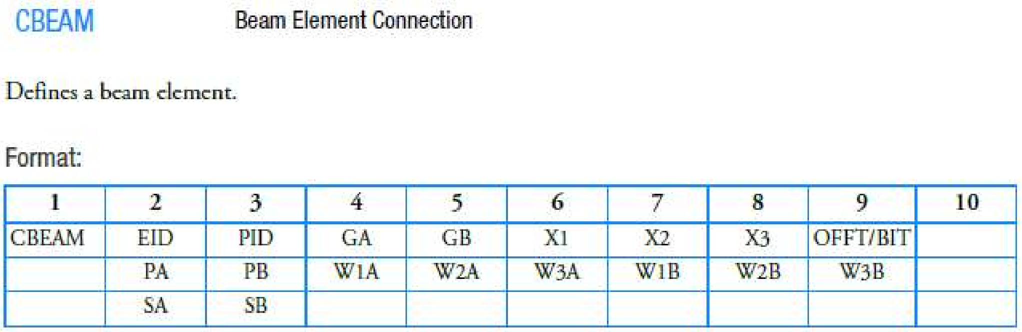

CBEAM Beam Element Connection

Defines a beam element.

Format:

1	2	3	4	5	6	7	8	9	10
CBEAM	EID	PID	GA	GB	X1	X2	X3	OFFT/BIT	
	PA	PB	W1A	W2A	W3A	W1B	W2B	W3B	
	SA	SB							

Figure D.1: The CBEAM Card [23]. Used for the stringers and stiffeners of the outer wing model.

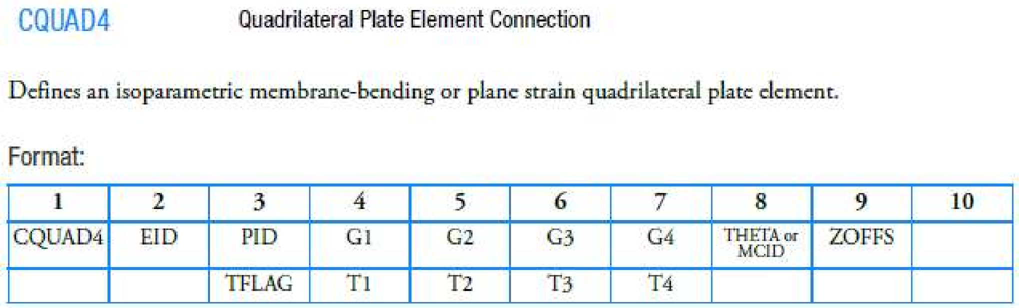

CQUAD4 Quadrilateral Plate Element Connection

Defines an isoparametric membrane-bending or plane strain quadrilateral plate element.

Format:

1	2	3	4	5	6	7	8	9	10
CQUAD4	EID	PID	G1	G2	G3	G4	THETA or MCID	ZOFFS	
		TFLAG	T1	T2	T3	T4			

Figure D.2: The CQUAD4 Card [23]. Used for the majority of the skin elements. Requires rectangular mesh elements.

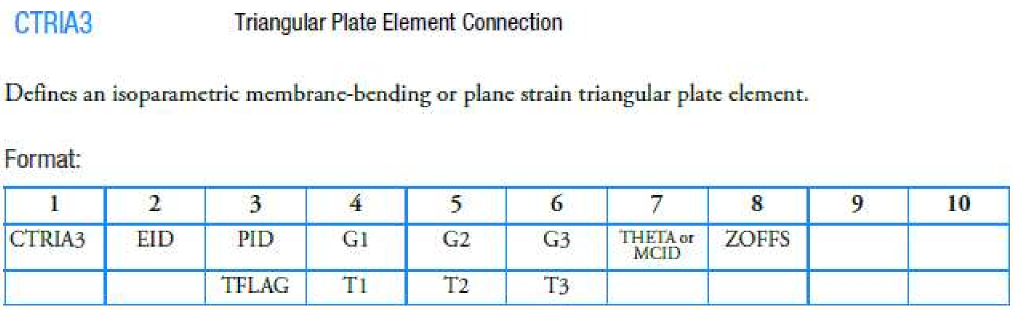

CTRIA3 Triangular Plate Element Connection

Defines an isoparametric membrane-bending or plane strain triangular plate element.

Format:

1	2	3	4	5	6	7	8	9	10
CTRIA3	EID	PID	G1	G2	G3	THETA or MCID	ZOFFS		
		TFLAG	T1	T2	T3				

Figure D.3: The CTRIA3 Card [23]. Used for the triangular skin elements.

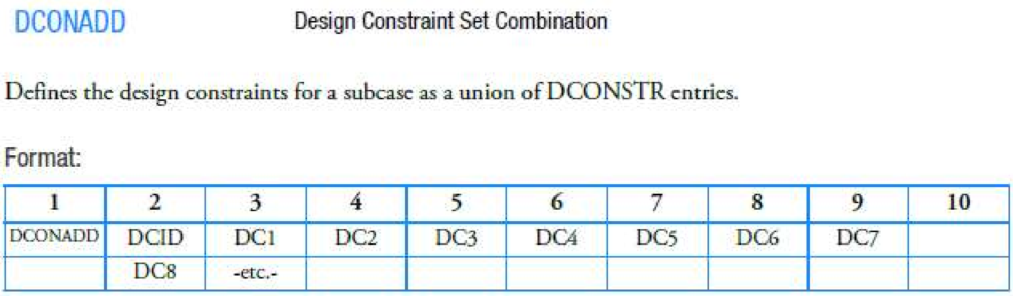

DCONADD Design Constraint Set Combination

Defines the design constraints for a subcase as a union of DCONSTR entries.

Format:

1	2	3	4	5	6	7	8	9	10
DCONADD	DCID	DC1	DC2	DC3	DC4	DC5	DC6	DC7	
	DC8	-etc.-							

Figure D.4: The DCONADD Card [23]. Used to specify the constraints applicable to each subcase. The Design Constraint ID needs to be match with the Template DESSUB.

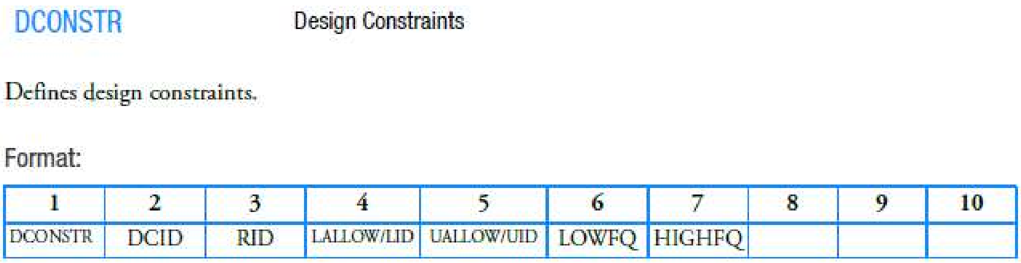

DCONSTR Design Constraints

Defines design constraints.

Format:

1	2	3	4	5	6	7	8	9	10
DCONSTR	DCID	RID	LALLOW/LID	UALLOW/UID	LOWFQ	HIGHFQ			

Figure D.5: The DCONSTR Card [23]. Used to specify the individual design constraints.

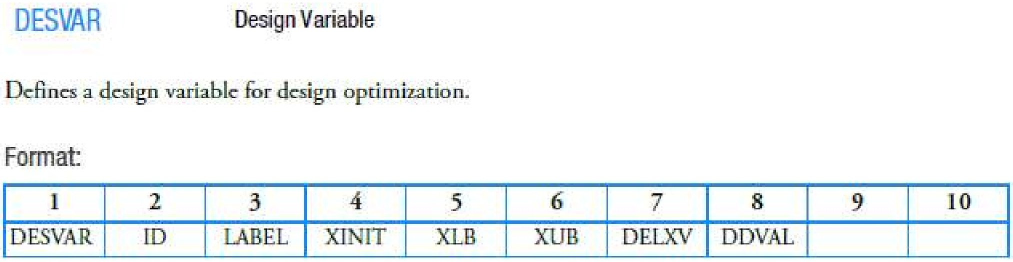

DESVAR Design Variable

Defines a design variable for design optimization.

Format:

1	2	3	4	5	6	7	8	9	10
DESVAR	ID	LABEL	XINIT	XLB	XUB	DELXV	DDVAL		

Figure D.6: The DESVAR Card [23]. Used to define a design variable.

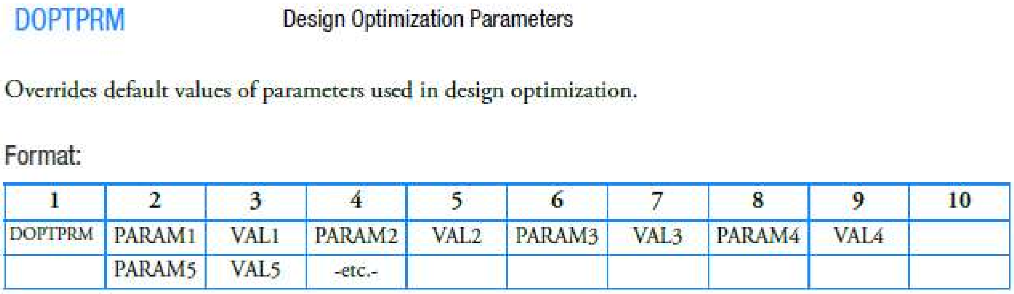

DOPTPRM Design Optimization Parameters

Overrides default values of parameters used in design optimization.

Format:

1	2	3	4	5	6	7	8	9	10
DOPTPRM	PARAM1	VAL1	PARAM2	VAL2	PARAM3	VAL3	PARAM4	VAL4	
	PARAM5	VAL5	-etc.-						

Figure D.7: The DOPTPRM Card [23]. Used to define the optimization settings.

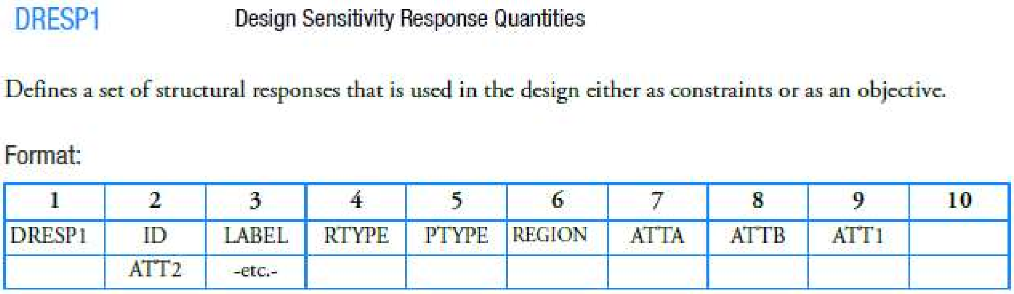

DRESP1 Design Sensitivity Response Quantities

Defines a set of structural responses that is used in the design either as constraints or as an objective.

Format:

1	2	3	4	5	6	7	8	9	10
DRESP1	ID	LABEL	RTYPE	PTYPE	REGION	ATTA	ATTB	ATT1	
	ATT2	-etc.-							

Figure D.8: The DRESP1 [23]. Used to link structural responses to constraints.

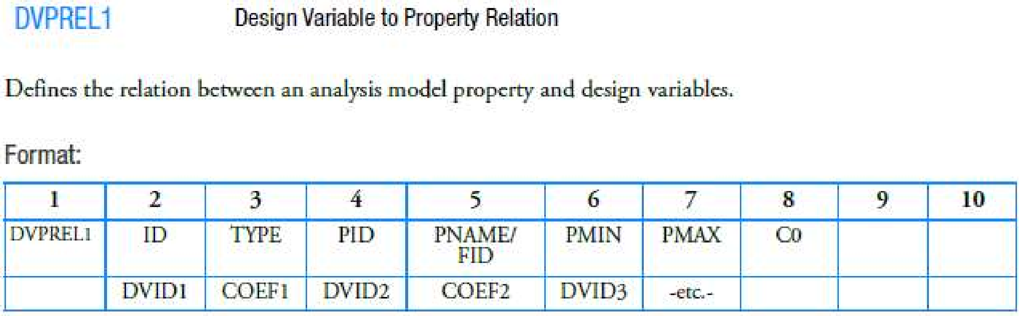

DVPREL1 Design Variable to Property Relation

Defines the relation between an analysis model property and design variables.

Format:

1	2	3	4	5	6	7	8	9	10
DVPREL1	ID	TYPE	PID	PNAME/ FID	PMIN	PMAX	C0		
	DVID1	COEF1	DVID2	COEF2	DVID3	-etc.-			

Figure D.9: The DVPREL1 Card [23]. Used to link the design variable to a model property.

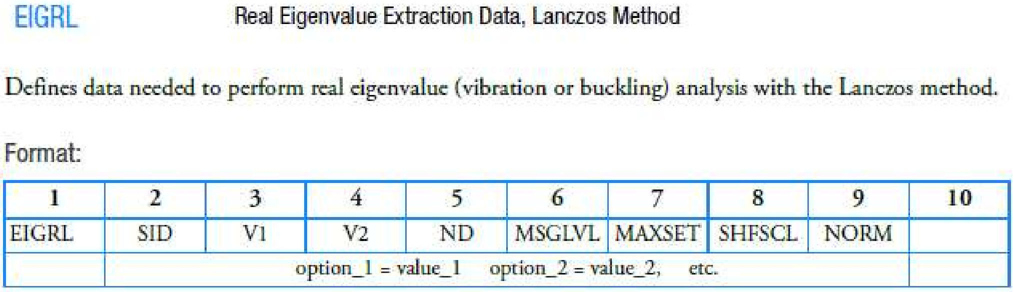

EIGRL Real Eigenvalue Extraction Data, Lanczos Method

Defines data needed to perform real eigenvalue (vibration or buckling) analysis with the Lanczos method.

Format:

1	2	3	4	5	6	7	8	9	10
EIGRL	SID	V1	V2	ND	MSGLVL	MAXSET	SHFSCL	NORM	
	option_1 = value_1 option_2 = value_2, etc.								

Figure D.10: The EIGRL Card [23]. Used to activate buckling analysis using the Lanczos method.

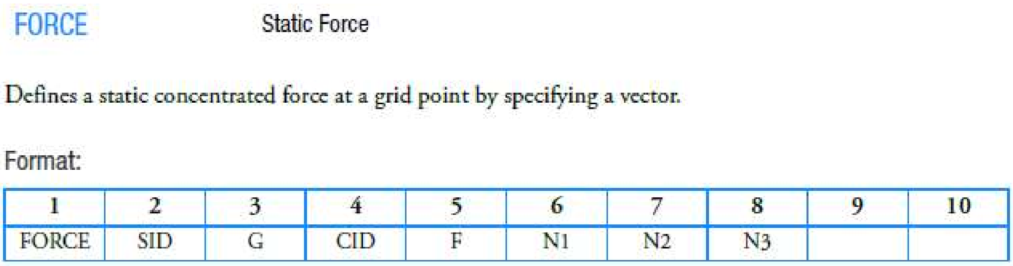

FORCE Static Force

Defines a static concentrated force at a grid point by specifying a vector.

Format:

1	2	3	4	5	6	7	8	9	10
FORCE	SID	G	CID	F	N1	N2	N3		

Figure D.11: The FORCE Card [23]. Used to define a point load.

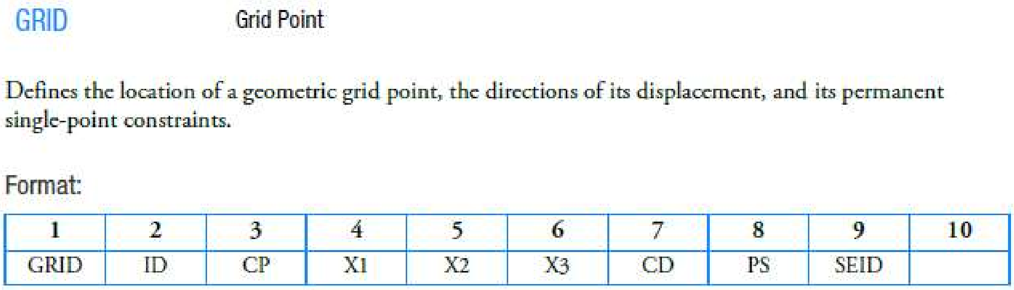

GRID Grid Point

Defines the location of a geometric grid point, the directions of its displacement, and its permanent single-point constraints.

Format:

1	2	3	4	5	6	7	8	9	10
GRID	ID	CP	X1	X2	X3	CD	PS	SEID	

Figure D.12: The GRID Card [23]. Used to define the grid points of the finite element model.

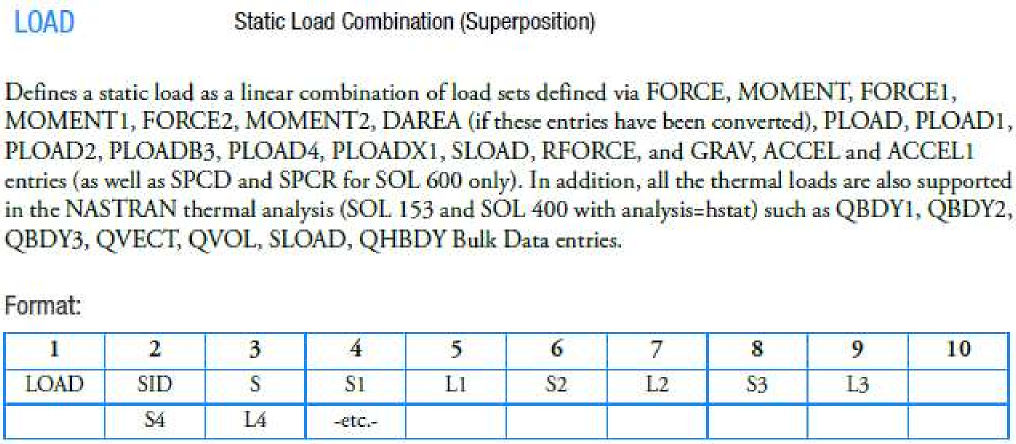

LOAD Static Load Combination (Superposition)

Defines a static load as a linear combination of load sets defined via FORCE, MOMENT, FORCE1, MOMENT1, FORCE2, MOMENT2, DAREA (if these entries have been converted), PLOAD, PLOAD1, PLOAD2, PLOADB3, PLOAD4, PLOADX1, SLOAD, RFORCE, and GRAV, ACCEL and ACCEL1 entries (as well as SPCD and SPCR for SOL 600 only). In addition, all the thermal loads are also supported in the NASTRAN thermal analysis (SOL 153 and SOL 400 with analysis=hstat) such as QBDY1, QBDY2, QBDY3, QVECT, QVOL, SLOAD, QHBDY Bulk Data entries.

Format:

1	2	3	4	5	6	7	8	9	10
LOAD	SID	S	S1	L1	S2	L2	S3	L3	
	S4	L4	-etc.-						

Figure D.13: The LOAD Card [23]. Used to specify the loads applicable to each subcase. The ID needs to be match with the Template LOAD ID.

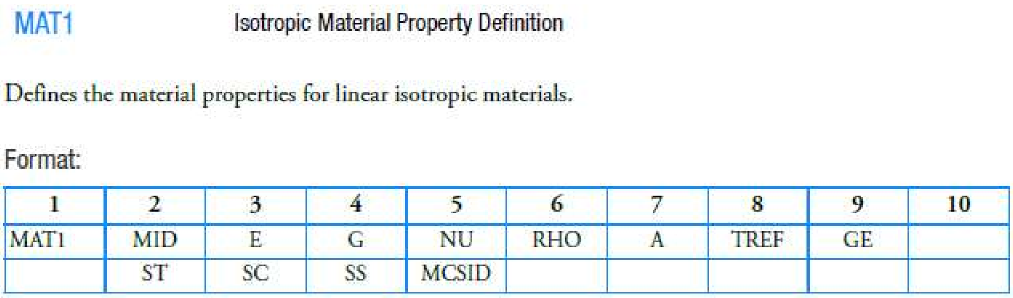

MAT1 Isotropic Material Property Definition

Defines the material properties for linear isotropic materials.

Format:

1	2	3	4	5	6	7	8	9	10
MAT1	MID	E	G	NU	RHO	A	TREF	GE	
	ST	SC	SS	MCSID					

Figure D.14: The MAT1 Card [23]. Used to define the material properties.

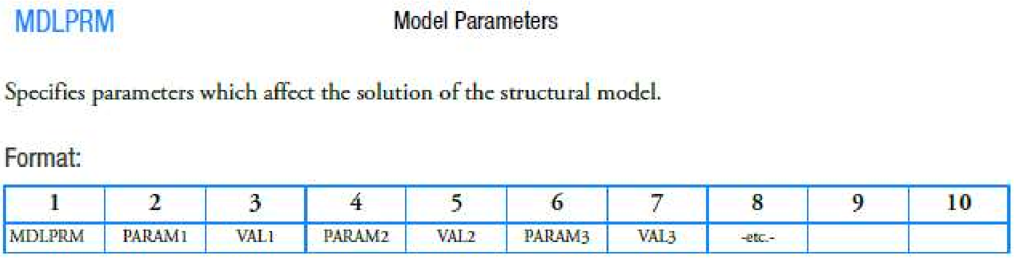

MDLPRM Model Parameters

Specifies parameters which affect the solution of the structural model.

Format:

1	2	3	4	5	6	7	8	9	10
MDLPRM	PARAM1	VAL1	PARAM2	VAL2	PARAM3	VAL3	-etc.-		

Figure D.15: The MDLPRM Card [23]. Used to request a H5 output file.

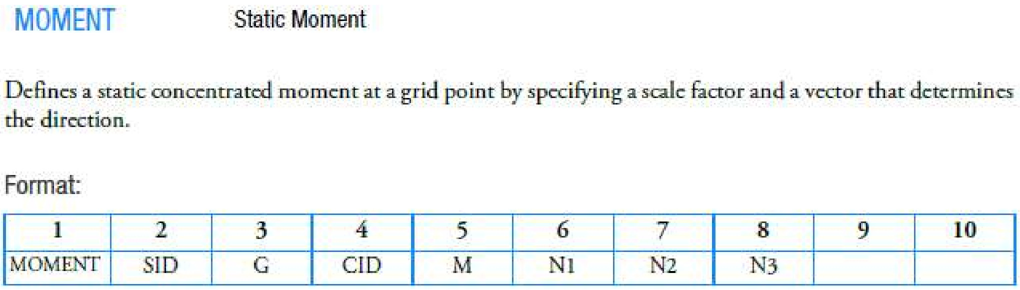

MOMENT Static Moment

Defines a static concentrated moment at a grid point by specifying a scale factor and a vector that determines the direction.

Format:

1	2	3	4	5	6	7	8	9	10
MOMENT	SID	G	CID	M	N1	N2	N3		

Figure D.16: The MOMENT Card [23]. Used to define a moment.

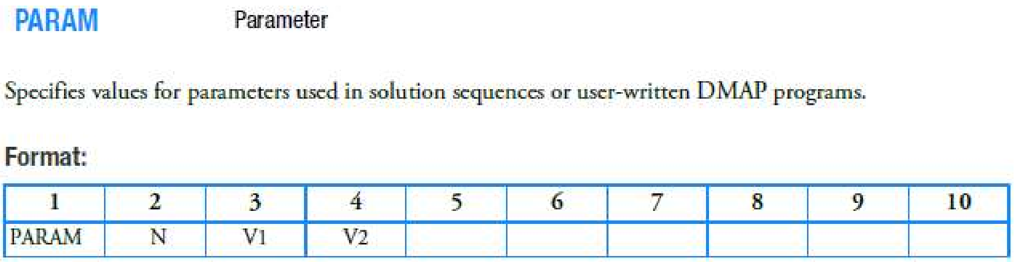

PARAM Parameter

Specifies values for parameters used in solution sequences or user-written DMAP programs.

Format:

1	2	3	4	5	6	7	8	9	10
PARAM	N	V1	V2						

Figure D.17: The PARAM Card [23]. Used to specify the format of the output data.

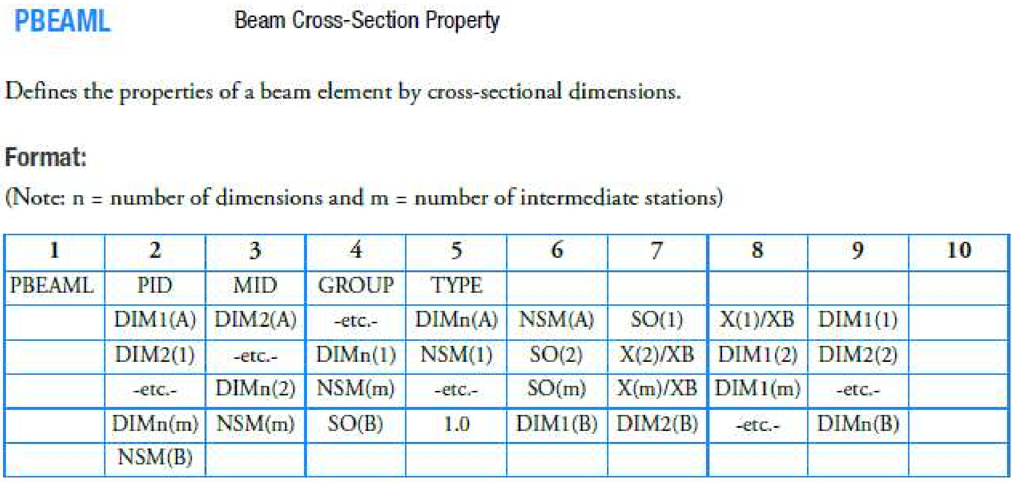

PBEAML Beam Cross-Section Property

Defines the properties of a beam element by cross-sectional dimensions.

Format:

(Note: n = number of dimensions and m = number of intermediate stations)

1	2	3	4	5	6	7	8	9	10
PBEAML	PID	MID	GROUP	TYPE					
	DIM1(A)	DIM2(A)	-etc.-	DIMn(A)	NSM(A)	SO(1)	X(1)/XB	DIM1(1)	
	DIM2(1)	-etc.-	DIMn(1)	NSM(1)	SO(2)	X(2)/XB	DIM1(2)	DIM2(2)	
	-etc.-	DIMn(2)	NSM(m)	-etc.-	SO(m)	X(m)/XB	DIM1(m)	-etc.-	
	DIMn(m)	NSM(m)	SO(B)	1.0	DIM1(B)	DIM2(B)	-etc.-	DIMn(B)	
	NSM(B)								

Figure D.18: The PBEAML Card [23]. Used to describe the shape of the stringers and stiffening elements. Linked to the CBEAM Card.

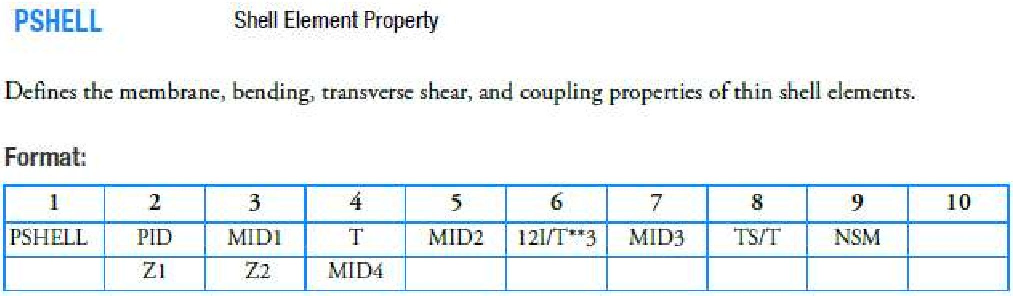

PSHELL Shell Element Property

Defines the membrane, bending, transverse shear, and coupling properties of thin shell elements.

Format:

1	2	3	4	5	6	7	8	9	10
PSHELL	PID	MID1	T	MID2	12I/T**3	MID3	TS/T	NSM	
	Z1	Z2	MID4						

Figure D.19: The PSHELL Card [23]. Used to model the skin and define the skin properties.

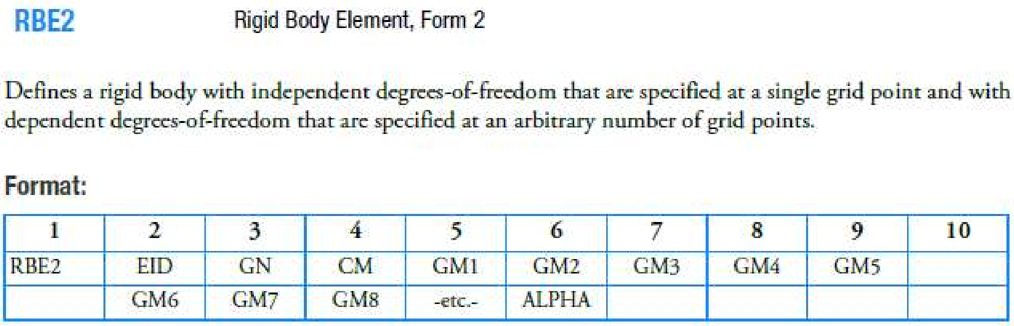

RBE2 Rigid Body Element, Form 2

Defines a rigid body with independent degrees-of-freedom that are specified at a single grid point and with dependent degrees-of-freedom that are specified at an arbitrary number of grid points.

Format:

1	2	3	4	5	6	7	8	9	10
RBE2	EID	GN	CM	GM1	GM2	GM3	GM4	GM5	
	GM6	GM7	GM8	-etc.-	ALPHA				

Figure D.20: The RBE2 Card [23]. Used to define the Rigid Body Elements, used to resemble the ribs and to introduce loads and boundary conditions.

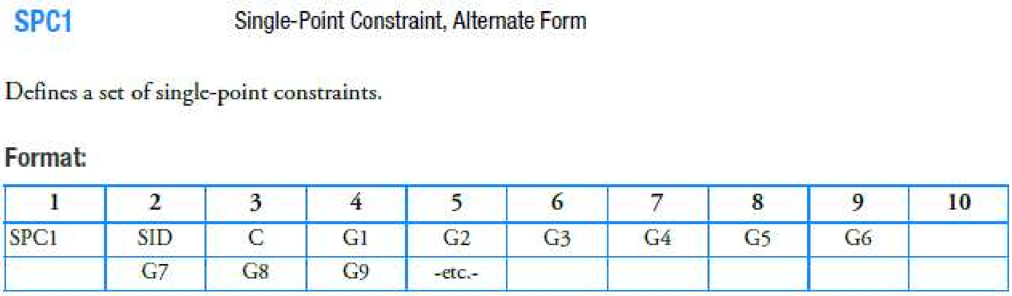

SPC1 Single-Point Constraint, Alternate Form

Defines a set of single-point constraints.

Format:

1	2	3	4	5	6	7	8	9	10
SPC1	SID	C	G1	G2	G3	G4	G5	G6	
	G7	G8	G9	-etc.-					

Figure D.21: The SPC1 Card [23]. Used to define a single point constraint, as part of the boundary conditions.

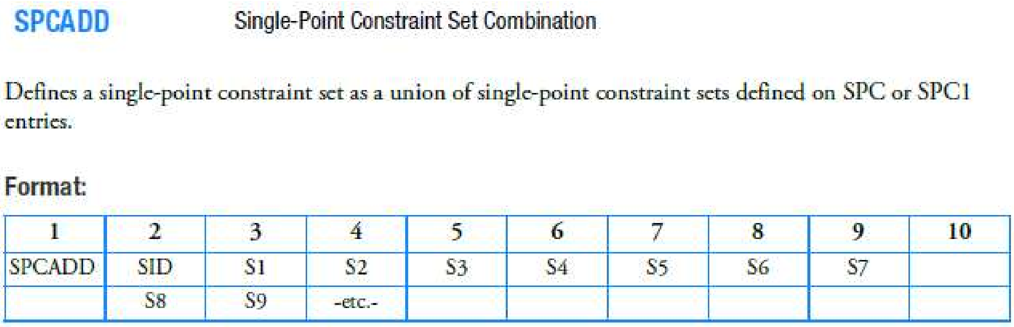

SPCADD Single-Point Constraint Set Combination

Defines a single-point constraint set as a union of single-point constraint sets defined on SPC or SPC1 entries.

Format:

1	2	3	4	5	6	7	8	9	10
SPCADD	SID	S1	S2	S3	S4	S5	S6	S7	
	S8	S9	-etc.-						

Figure D.22: The SPCADD Card [23]. Used to define a constraint set, to specify for each subcase the boundary conditions. Needs to match with the Template.

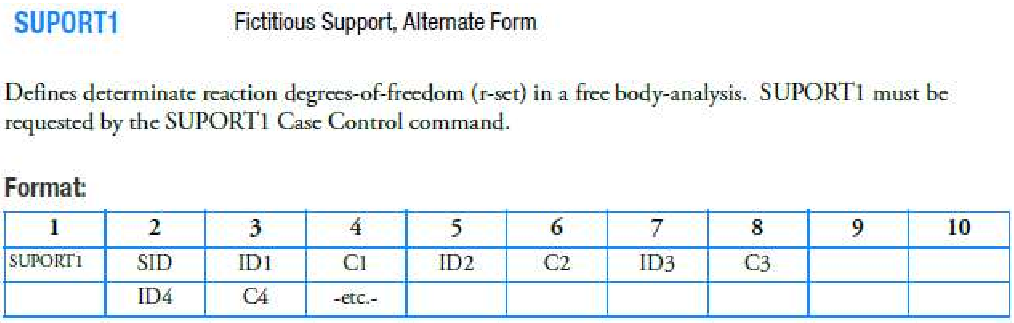

SUPORT1 Fictitious Support, Alternate Form

Defines determinate reaction degrees-of-freedom (r-set) in a free body-analysis. SUPORT1 must be requested by the SUPORT1 Case Control command.

Format:

1	2	3	4	5	6	7	8	9	10
SUPORT1	SID	ID1	C1	ID2	C2	ID3	C3		
	ID4	C4	-etc.-						

Figure D.23: The SUPORT1 Card [23]. Used to define a additional constraint. Needs to be referenced in the Template.

E

Additional Results Design of Experiments

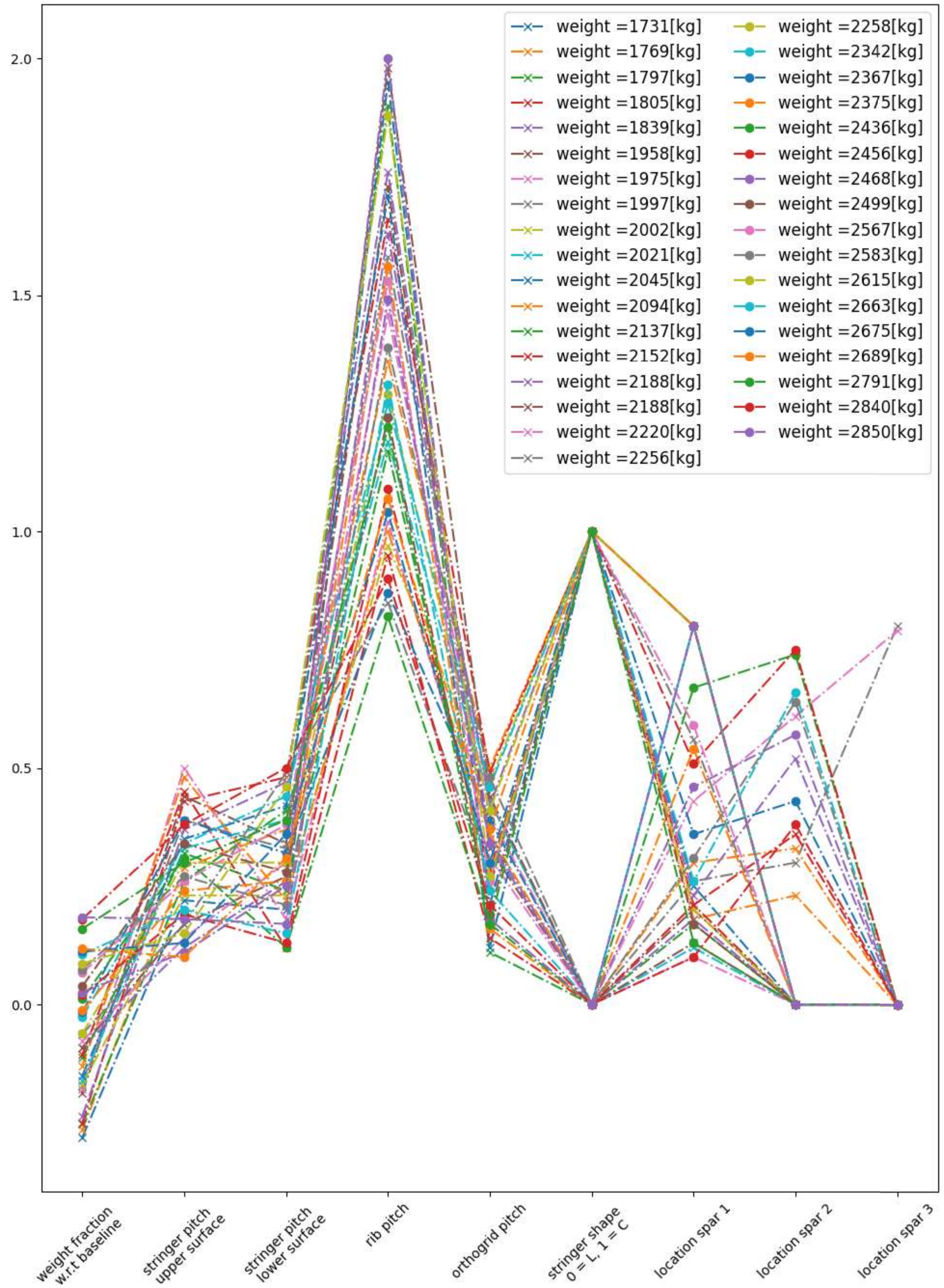

Figure E.1: Plot showing the structural weight of several different layouts as a result of a design of experiments. The weight is indicated as a percentage w.r.t. the baseline design weight. The stringer pitches, rib pitch, and orthogrid pitch are given in [m]. The stringer shape is indicated in binary. A value of zero indicates an L-shaped stringer, a value of one indicates an C-shaped stringer is used. The location of the spar is given in percentage of chord. If a value of zero is given, this means that the spar is not present.

Bibliography

[1] K. S. Al-Rubaie. "A general model for stress-life fatigue prediction", *Materialwissenschaft und Werkstofftechnik* Vol. 39, no. 6 (2008), 400–406. DOI: `10.1002/mawe.200800282`.

[2] J. Benad. "The Flying V - A new Aircraft Configuration for Commercial Passenger Transport", *Deutscher Luft- und Raumfahrtkongress 2015* (2015), pp. 1–8. DOI: `10.25967/370094`.

[3] A.L Bolsunovsky et al. "Flying wing—problems and decisions", *Aircraft Design* Vol. 4, no. 4 (2001), 193–219. DOI: `10.1016/s1369-8869(01)00005-2`.

[4] *BREPTOOLS HISTORY class reference.* URL: `https://dev.opencascade.org/doc/occt-7.4.0/refman/html/class_b_rep_tools___history.html`.

[5] *Cantilevered Plate.* URL: `https://help.hexagonmi.com/bundle/MSC_Nastran_2022.1/page/Nastran_Combined_Book/design_opt/dsoexample/TOC.Cantilevered.Plate.xhtml`.

[6] Niu Michael Chun-Yung. *Airframe structural design - practical design information and data on Aircraft Structures (2nd edition).* AD Adaso/Adastra Engineering LLC, 1999.

[7] M. Claeys. "Flying V and Reference Aircraft Structural Analysis and Mass Comparison". Thesis. Delft University of Technology, 2018.

[8] O. Dababneh and A. Kayran. "Design, analysis and optimization of thin walled semi-monocoque wing structures using different structural idealization in the preliminary design phase". English, *International Journal of Structural Integrity* Vol. 5, no. 3 (2014). Cited By :4, pp. 214–226. URL: `www.scopus.com`.

[9] Odeh Dababneh and Timoleon Kipouros. "A review of aircraft wing mass estimation methods", *Aerospace Science and Technology* Vol. 72 (2018), pp. 256–266. ISSN: 1270-9638. DOI: `https://doi.org/10.1016/j.ast.2017.11.006`. URL: `https://www.sciencedirect.com/science/article/pii/S1270963817307113`.

[10] JB De Jong et al. "A standardized load sequence for flight simulation tests on transport aircraft wing structures", *NLR-TR 73029 U, LBF Bericht FB-106* (1973).

[11] JKS Dillinger et al. "Stiffness Optimization of Composite Wings with Aeroelastic Constraints". English, *12th AIAA Aviation Technology, Integration, and Operations (ATIO) Conference and 14th AIAA/ISSMO Multidisciplinary Analysis and Optimization Conference Online Proceedings (2012)*. Ed. by s.n. United States: American Institute of Aeronautics and Astronautics Inc. (AIAA), 2012, pp. 1–15. DOI: `10.2514/6.2012-5401`.

[12] T.P. Dotman. "A Structural Sizing Methodology for the Wing-Fuselage of the Flying-V". MSc Thesis. Delft University of Technology, 2021.

[13] Ali Elham. "Weight indexing for multidisciplinary design optimization of lifting surfaces", (2013).

[14] F. Faggiono. "Aerodynamic Design Optimisation of a Flying V Aircraft". MSc Thesis. Delft University of Technology, 2016.

[15] Megson T H G. *Aircraft Structures for engineering students.* Elsevier, 2022.

[16] Russell Charles Hibbeler. *Mechanics of materials.* Pearson Education, 2005.

[17] M. Hillen. "Parametrisation of the Flying V Outer Mould Line". MSc Thesis. Delft University of Technology, 2020.

[18] Erwin H Johnson. "Fully Stressed Design in MSC. Nastran", *MSC 3rd Worldwide Aerospace Users Conference and Technology Showcase.* 2002.

[19] Bruce I. Larrimer. *Beyond tube-and-wing:* NASA, 2020.

[20] G. R. Liu and S. S. Quek. "Chapter 11 - Modeling Techniques", *The Finite Element Method: A practical course.* Butterworth-Heinemann, 2014.

[21] R Martinez-Val and E Perez. "Aeronautics and astronautics: Recent progress and future trends", *Proceedings of the Institution of Mechanical Engineers, Part C: Journal of Mechanical Engineering Science* Vol. 223, no. 12 (2009), 2767–2820. DOI: `10.1243/09544062jmes1546`.

[22] MSC Nastran. *Design sensitivity and optimization user's guide.* 2013.

[23] MSC Nastran and HEXAGON. "Quick Reference Guide", *MSC. SOFTWARE* Vol. 1 (2020).

[24] T. Nieuwenhuizen. "Conceptual Design Optimisation of a Flying V Aircraft". MSc Thesis. Delft University of Technology, 2021.

[25] W. Oosterom. "Flying-V Family Design". MSc Thesis. Delft University of Technology, 2021.

[26] W.D. Pilkey and Bi Z. *Peterson's Stress Concentraion Factors.* John Wiley & Sons, 2020.

[27] N Eswara Prasad and Russel JH Wanhill. *Aerospace materials and material technologies.* Vol. 3. Springer, 2017.

[28] Osvaldo M Querin et al. *Topology design methods for structural optimization.* Butterworth-Heinemann, 2017.

[29] Martijn Roelofs and Roelof Vos. "Semi-analytical composite oval fuselage weight estimation", *55th AIAA Aerospace Sciences Meeting* (2017). DOI: `10.2514/6.2017-0466`.

[30] *salome mesh user's guide: introduction to mesh.* 2022. URL: `https://docs.salome-platform.org/7/gui/SMESH/index.html`.

[31] European Union. *Transport and The Green Deal.* 2022. URL: `https://ec.europa.eu/info/strategy/priorities-2019-2024/european-green-deal/transport-and-green-deal_en`.

[32] L. van der Schaft. "Development, Model Generation and Analysis of a Flying V Structure Concept". Thesis. Delft University of Technology, 2017.

[33] Arne Voss and Thomas Klimmek. "Design and sizing of a parametric structural model for a UCAV configuration for loads and aeroelastic analysis", *CEAS Aeronautical Journal* Vol. 8, no. 1 (2017), pp. 67–77.

[34] Weizhu Yang et al. "Aircraft wing structural design optimization based on automated finite element modelling and ground structure approach", *Engineering Optimization* Vol. 48, no. 1 (2015), 94–114. DOI: `10.1080/0305215x.2014.995175`.

[35] Chao You et al. "Identification of the key design inputs for the FEM-based preliminary sizing and mass estimation of a civil aircraft wing box structure", *Aerospace Science and Technology* Vol. 121 (2022), p. 107284.